Alma Mater Studiorum - Università di Bologna

School of Science
Department of Physics and Astronomy
Master Degree Programme in Astrophysics and Cosmology

Dynamics of Prolate Galaxies

Graduation Thesis

Presented by:
Giulia Congera

Supervisor:
Chiar.mo Prof. Luca Ciotti

Co-supervisor:
Dr. Leonardo De Deo

Academic year 2024-2025
Graduation date III

The most exciting phrase to hear in science, the one that heralds new discoveries, is not 'Eureka!' but 'That's funny...'

Isaac Asimov

ABSTRACT

Elliptical galaxies are stellar systems whose intrinsic shape can be triaxial or axisymmetric, with the latter including both oblate and prolate shapes. Among axisymmetric galaxies, the internal dynamics of oblate galaxies has been extensively studied and is quite well understood. In contrast, prolate galaxies have received much less attention and their internal dynamics is still not as well understood as that of oblate galaxies. They are, in fact, significantly more complicated from the dynamical point of view: it is sufficient to recall that, while oblate stellar systems have a hydrodynamical analogue, thus they can, at a very basic level, be imagined as rotating fluids, no such fluid analogue exists for prolate systems.

This thesis aims to contribute to filling this gap by providing a theoretical analysis of various dynamical properties of prolate systems through a comparison with their oblate counterparts. We restrict the analysis to ellipsoidally stratified models, as they provide a good description of elliptical galaxies, and we focus on two-integral systems (i.e., systems described by a distribution function which depends on the classical two integrals of motion: the energy E and the component L_z along the symmetry axis of the angular momentum).

Comparing systems with intrinsically different shapes is not as straightforward as it might appear at first sight and some conditions must be specified. Therefore, to carry out a physically meaningful comparison between oblate and prolate galaxies, we construct oblate-prolate *conjugate pairs* with the same mass, the same intrinsic density profile and the same edge-on surface brightness profile. The possibility of constructing such photometrically indistinguishable systems is non-trivial and represents an important result of this work. This degeneracy also makes the study of kinematical signatures that distinguish oblate and prolate galaxies particularly relevant in the observational context. The first step of this work is therefore to identify the conditions to construct such conjugate pairs.

We then explore more general differences between oblate and prolate galaxies. First, we use the Tensor Virial Theorem to study their main energetic differences. Second, we analyse some important properties of their gravitational field and introduce the Jeans equations for two-integral systems. Third, we investigate the consistency of axisymmetric models by studying the sign of the average squared azimuthal velocity $\overline{v_\varphi^2}$. Finally, we return to conjugate pairs and highlight kinematical differences between oblate and prolate systems to derive constraints on their intrinsic shape.

The results of this thesis reveal the main peculiarities of prolate systems and show that they are not simply oblate systems with "inverted" axial ratio. Furthermore, by providing a clearer understanding of their dynamics, this work lays a solid foundation for future studies aimed at further exploring prolate galaxies.

Contents

CHAPTER 1

Introduction

After the first morphological classification of galaxies by Hubble (1926), the structure and dynamics of galaxies have always been of great interest in astrophysical research, due to their numerous fundamental implications, ranging from constraining the distribution of dark matter to testing theories of galaxy formation and evolution. However, determining the intrinsic shape and dynamical structure of galaxies is not a trivial challenge.

Hubble's classification showed that galaxies fall in two broad categories: ellipticals, which in projection have an elliptical shape, and spirals, characterised by a disk-like structure. Among these, elliptical galaxies are by far the most challenging when it comes to determining their intrinsic shape. This is primarily due to the fact that, while for disks it is immediate to identify their orientation with respect to the observer, for ellipsoids it is instead much more complicated, making their deprojection particularly difficult.

Early studies assumed elliptical galaxies to be oblate spheroids with isotropic stellar velocity dispersion and supported by rotation. In the '70s, however, the advent of long-slit spectroscopy revealed that the low rotation of many elliptical galaxies could not account for their observed flattening (Bertola and Capaccioli 1975; Illingworth 1977; Schechter and Gunn 1979). This motivated alternative hypotheses, namely that galaxies could be prolate (Miller 1978) or triaxial (Binney 1978). It is now well established that most elliptical galaxies are triaxial. Nevertheless, all three intrinsic shapes, oblate, prolate and triaxial, are physically possible and, in most cases, anisotropic stellar velocity dispersion, rather than rotation, is responsible for their flattening.

Triaxial systems are difficult to handle analytically, since their dynamics at equilibrium involves non-classical integrals of motion, whose explicit expression is rarely known, requiring numerical treatments (e.g., Schwarzschild 1979). For this reason, in this thesis we analyse only axisymmetric systems, with particular focus on the prolate case.

Compared to the extensively studied oblate galaxies, prolate galaxies have received much less attention, and their internal dynamics is not understood as well as that of oblate systems. In addition to this, there are several other compelling reasons to investigate them further.

First, the existence of prolate systems is not only predicted by theoretical models but is proven by observations. Bertola and Galletta (1978) observed dust lanes aligned with the projected minor axis in a few elliptical galaxies, a configuration stable only in prolate systems. More recently, integral-field spectroscopy (IFS) has revealed several "prolate

rotators", i.e., galaxies rotating around their projected major axis, indicative of triaxial or prolate shapes. Such systems have been found in the ATLAS^{3D} survey (Krajnović et al. 2011), in the CALIFA survey (Tsatsi et al. 2017) and in the MaNGA survey (Li, Mao, Cappellari, et al. 2018). Simulations agree with these findings: Ebrová and Łokas (2017) and Li, Mao, Emsellem, et al. (2018) identified several prolate rotators in the Illustris simulation. These studies further suggest that prolate galaxies are more frequent among most massive systems.

Second, statistical studies show that prolate galaxies should be quite common: Kimm and Yi (2007) found that about 26% of ellipticals should be prolate in order to reproduce the observed distribution of apparent flattenings.

Finally, although this analysis specifically addresses elliptical galaxies, a detailed study of prolate systems could also be particularly relevant in the context of dark matter: halos produced in cosmological simulations are on average prolate (Jing and Suto 2002), and those resulting from binary mergers are typically prolate or triaxial (Novak et al. 2006).

Motivated by these considerations, this thesis provides an original and in-depth theoretical analysis of the dynamics of prolate galaxies, through a comparison with oblate galaxies. Particular attention is devoted to showing that, from various points of view, prolate systems are fundamentally different from oblate ones, and cannot be regarded simply as oblate systems with an "inverted" axial ratio.

Moreover, this thesis addresses a problem of direct observational relevance: first, it demonstrates that it is possible to construct oblate and prolate systems that are photometrically identical in projection, and then it answers the question of whether they can be kinematically distinguished. This question is central to the interpretation of current and future large IFS surveys.

We limit our analysis to ellipsoidally stratified systems, as they provide a good description of elliptical galaxies, and we focus particularly on classical two-integral systems (i.e., systems described by a distribution function, hereafter DF, which depends on the two classical integrals of motion: the energy E and the component L_z along the symmetry axis of the angular momentum). While a fully accurate description of real galaxies generally also requires a third, non-classical integral of motion (e.g., Binney, Davies, et al. 1990; van der Marel 1991), whose form is in general not known analytically, and which may not even exist for all orbits, adopting a two-integral DF allows for a relatively simple analytical treatment and still provides a useful first-order approximation to better understand the dynamics of axisymmetric systems.

This thesis is structured as follows. In Chapter 2, we explain how we aim to compare oblate and prolate systems and illustrate the non-trivial procedure to construct *conjugate* pairs, i.e., oblate and prolate models sharing the same mass, intrinsic (normalised) density profile and edge-on surface brightness profile. In Chapters 3, 4 and 5, we investigate more general aspects of axisymmetric systems. In Chapter 3 we exploit the Tensor Virial Theorem to study their global dynamical and energy-related properties. In Chapter 4, we analyse general characteristics of the gravitational field of axisymmetric ellipsoids and introduce the Jeans equations (JEs) for two-integral systems. In Chapter 5, we examine the physical consistency of prolate systems by considering the sign of the mean squared azimuthal velocity $\overline{v_\varphi^2}$ and determining the conditions under which the models become unphysical ($\overline{v_\varphi^2} < 0$). Finally, in Chapter 6, we numerically solve the JEs to obtain the intrinsic and projected kinematical fields for conjugate systems and derive dynamical constraints on their intrinsic shape. In Chapter 7, the main conclusions are briefly summarised.

CHAPTER 2

Comparing Oblate and Prolate Systems

In this chapter, we introduce the notation adopted throughout the thesis to describe axisymmetric ellipsoidal systems and we address the problem of comparing oblate and prolate systems. In Section 2.1 we present the rules to be followed for a physically meaningful comparison and in Sections 2.2 and 2.3 we illustrate the procedure to construct oblate and prolate systems satisfying these rules.

2.1 How to compare oblate and prolate systems

As we will see in this chapter, the idea of comparing oblate and prolate systems, even though it may look simple at first sight, is by no means an easy task. In fact, when comparing systems with different intrinsic shapes, some constraints are of course needed.

To clarify the nature of this problem, suppose for example that we are interested in answering a quite natural question, such as "is a prolate system more or less gravitationally bound than an oblate system?". It is immediate to realise that this question cannot be answered. In fact, suppose we start with a spherical galaxy and we construct from it an oblate and a prolate system. To produce the oblate system, one possibility is to expand the equator without squeezing the poles; alternatively, we could maintain the same equatorial size and squeeze the poles. Similarly, a prolate system can be obtained by reducing the equatorial size with fixed poles or by stretching the poles farther apart with fixed equator. Clearly, the gravitational energy of these systems can differ significantly: for instance, the compact oblate system is much more bound than the extended prolate one.

This elementary exercise shows immediately that a well-defined procedure must be determined in order to obtain a physically meaningful comparison between oblate and prolate systems. In this work, we devised a set of rules to be followed, which we now list and that will be discussed in depth in the following sections of this chapter.

- **Request R1: same mass**
  This request is quite obvious: when considering differences between properties such as gravitational energy, gravitational field strength, velocity dispersion and rotational velocity values, it is natural to compare systems with the same mass, independently of their size and shape. In Section 2.2 we illustrate a procedure that allows us to build axisymmetric systems, oblate and prolate, with arbitrary size, maintaining their mass fixed.

- **Request R2: same intrinsic (normalised) density profile**
  This request is also quite natural. Clearly, systems with different density profiles are characterised by different dynamics even at fixed flattening/elongation. Therefore, when comparing oblate and prolate systems we have to limit the comparison to pairs of systems sharing the same density profile, such as de Vaucouleur oblate and prolate systems, or Hernquist oblate and prolate systems.

- **Request R3: same surface brightness profile**
  The third request is the least obvious. It is related to the physical size and shape of oblate and prolate systems and is motivated by observational reasons. In practice, we ask what are the dynamical differences between an oblate and a prolate system that, in projection, have the same surface brightness profile. The fact that this request can be satisfied, simultaneously with R1 and R2, is far from obvious. As we will see in Section 2.3, determining the conditions on the size and shape of oblate and prolate systems under which this occurs is not straightforward and it is, in fact, an important result of this thesis.

To summarise, in this chapter we present a rigorous procedure to construct pairs of oblate and prolate galaxy models with arbitrary flattening/elongation, that share the same mass, the same intrinsic density profile and the same surface brightness distribution once projected on the sky. This step is fundamental for the remaining parts of the thesis because

it provides the basis for a quantitative investigation of the differences between oblate and prolate systems.

2.2 R1 and R2: same mass and intrinsic density profile

In this work, we will limit our study to axisymmetric stellar systems whose density distribution ρ is constant on ellipsoidal surfaces defined by

$$\frac{R^2}{a^2} + \frac{z^2}{a^2 q^2} = m^2, \quad m \geq 0, \tag{2.1}$$

where $R = \sqrt{x^2 + y^2}$ is the cylindrical radius, $a > 0$ is a generic scale length, $q > 0$ is the axial ratio (i.e., the ratio between the z-semiaxis and the R-semiaxis of each ellipsoidal surface, so that $q = 1$ corresponds to a sphere, $q < 1$ corresponds to an oblate system and $q > 1$ corresponds to a prolate system). The z-axis is chosen to be the symmetry axis of the system and m is a parameter mapping the ellipsoidal surfaces, so that varying m generates a family of homothetic ellipsoids.

We now want to impose the constraints R1 and R2. We start by considering a generic ellipsoid with density

$$\rho(m) = \rho_n \tilde{\rho}(m), \tag{2.2}$$

where ρ_n is a normalisation constant to be determined and $\tilde{\rho}(m)$ is a generic dimensionless function that we assume fixed in order to satisfy R2.

We then impose condition R1. The total mass M of the ellipsoid can be easily obtained by a volume integration as:

$$M = \int_V \rho dV = \rho_n 4\pi a^3 q \mathcal{M}, \quad \mathcal{M} \equiv \int_0^\infty m^2 \tilde{\rho}(m) dm. \tag{2.3}$$

Equation (2.2) for the density can therefore be rewritten as

$$\rho(m) = \frac{M}{4\pi a^3 q \mathcal{M}} \tilde{\rho}(m). \tag{2.4}$$

The expression above allows us, for fixed $\tilde{\rho}(m)$ and M, to arbitrarily vary a and q (i.e., size and shape), while ensuring that the total mass remains fixed.

2.3 R3: same two-dimensional surface brightness profile

We now consider the projection on the plane of the sky of a generic axisymmetric ellipsoid $\rho(m)$ as in (2.4), with arbitrary size and shape, but constant total mass M. We limit ourselves to the edge-on case, assuming that the line of sight (los) is aligned, for example, with the x-axis. We also assume that the observer is at infinite distance from the system and that the latter is "transparent" (i.e., without overlap of stars along the los). Under

these assumptions, the surface density profile is

$$\Sigma(l) = 2\int_0^\infty \rho(m)dx = \frac{M}{2\pi a^2 q \mathcal{M}}\tilde{\Sigma}(l), \tag{2.5}$$

where

$$\tilde{\Sigma}(l) \equiv \int_l^\infty \frac{\tilde{\rho}(m)mdm}{\sqrt{m^2 - l^2}}, \quad l^2 = \frac{y^2}{a^2} + \frac{z^2}{a^2 q^2}. \tag{2.6}$$

Equation (2.6) describes the isophotes in the (y, z) projection plane, where l can be interpreted as an elliptical radius. This equation shows that the isophotes have the same axial ratio q as the intrinsic density profile and $\tilde{\Sigma}(l)$ remains the same function of l for every scale length a and axial ratio q. In other words, $\tilde{\Sigma}(l)$ depends only on $\tilde{\rho}(m)$.

We now investigate the possibility of constructing oblate and prolate ellipsoids that produce the same projected image and are, thus, indistinguishable through photometric observations, i.e., they satisfy the request R3. Assessing whether such degeneracies exist is crucial for understanding the limitations of photometry in constraining the intrinsic shape of galaxies and to identify when complementary approaches may be necessary.

From equations (2.5) and (2.6), it is obvious that if we ask for the same $\Sigma(l)$ in the two systems, the shape of l must be the same. Therefore, we call q_o the axial ratio of the oblate system and q_p that of the prolate system and, since for both cases z is the symmetry axis, as shown in Figure 2.1, it is immediate that the following condition must hold:

$$q_p = \frac{1}{q_o}. \tag{2.7}$$

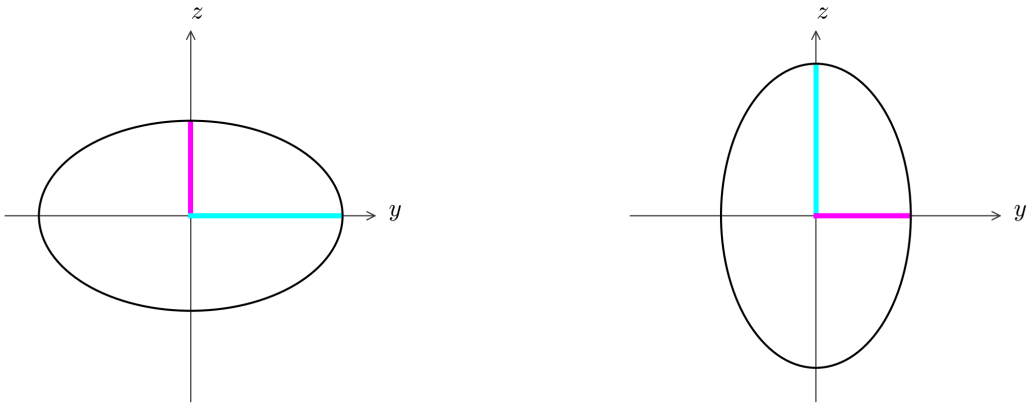

Figure 2.1. Example of an isophote of the projected oblate system (left) and an isophote, with the same shape, of the projected prolate system (right). The axial ratio of the oblate system is the ratio between the magenta line and the cyan line. The axial ratio of the prolate system is the ratio between the cyan line and the magenta line.

With this condition satisified, $\Sigma_o(l)$ of the oblate system and $\Sigma_p(l)$ of the prolate system are not yet the same, due to the denominator in equation (2.5). Let us consider an oblate system and let a_o and q_o its parameters appearing in equations (2.4) and (2.5). In

particular, we have

$$\Sigma_o(l) = \frac{M}{2\pi a_o^2 q_o \mathcal{M}} \tilde{\Sigma}(l), \quad l^2 = \frac{y^2}{a_o^2} + \frac{z^2}{a_o^2 q_o^2}. \tag{2.8}$$

Let us now consider a prolate system with the same $\tilde{\rho}(m)$ and total mass M as the oblate one, but with length scale a_p and axial ratio q_p. Therefore,

$$\Sigma_p(l) = \frac{M}{2\pi a_p^2 q_p \mathcal{M}} \tilde{\Sigma}(l), \quad l^2 = \frac{y^2}{a_p^2} + \frac{z^2}{a_p^2 q_p^2}. \tag{2.9}$$

Being M, $\mathcal{M}$ and $\tilde{\Sigma}(l)$ the same in the two systems, the remaining request is that

$$a_p^2 q_p = a_o^2 q_o \tag{2.10}$$

and, from the condition 2.7,

$$a_p = a_o q_o. \tag{2.11}$$

Summarising the main logical steps:

1. We considered a family of axisymmetric ellipsoidal models $\rho(m)$ of fixed total mass M and given (normalised) density profile $\tilde{\rho}(m)$, with symmetry axis along z and with arbitrary scale length a and axial ratio q.

2. We projected the system edge-on (e.g., along the x direction) and we obtained $\Sigma(l)$ given by equation (2.5), with isophotes in the (y, z) projection plane whose equation is given in (2.6). By construction, the projection has the same $\tilde{\Sigma}(l)$ and total mass (i.e., total luminosity) for arbitrary values of a and q.

3. Finally, considering an oblate system with scale length a_o and axial ratio q_o and a prolate system with scale length a_p and axial ratio q_p, we obtained that the two ellipsoids have $\Sigma_o(l) = \Sigma_p(l)$ provided $q_p = 1/q_o$, $a_p^2 q_p = a_o^2 q_o$ and $a_p = a_o q_o$ (where only two of these three conditions are independent, since any one can be derived from the other two). With these constraints, all the requests R1, R2, R3 are satisfied, allowing us to conduct our experiments. From now on we refer to pairs of systems satisfying these requests as *conjugate systems*.

Note that the spatial density is *not* the same, as

$$\rho_o(m) = \frac{M}{4\pi a_o^3 q_o \mathcal{M}} \tilde{\rho}(m), \tag{2.12}$$

$$\rho_p(m) = \frac{M}{4\pi a_p^3 q_p \mathcal{M}} \tilde{\rho}(m), \tag{2.13}$$

thus

$$\rho_p(m) = \frac{\rho_o(m)}{q_o}, \tag{2.14}$$

i.e., the conjugate prolate ellipsoid is denser than the oblate one by a factor $1/q_o = q_p$. This is consistent with the fact that, along the line of sight, the prolate system is more compact and therefore requires a higher density to reproduce the same projection as the oblate system.

To provide a visual representation of conditions (2.7), (2.10) and (2.11), Figure 2.2 shows an example of two ellipsoidal surfaces, one oblate and one prolate, obtained from equation (2.1) for a fixed m, and satisfying the three conditions. The two systems are oriented in the same way, to make the comparison clearer, and viewed close to edge-on. The coloured segments indicate which axes are equal in length and the figure clearly shows that the prolate system is shorter than the oblate one along the line of sight.

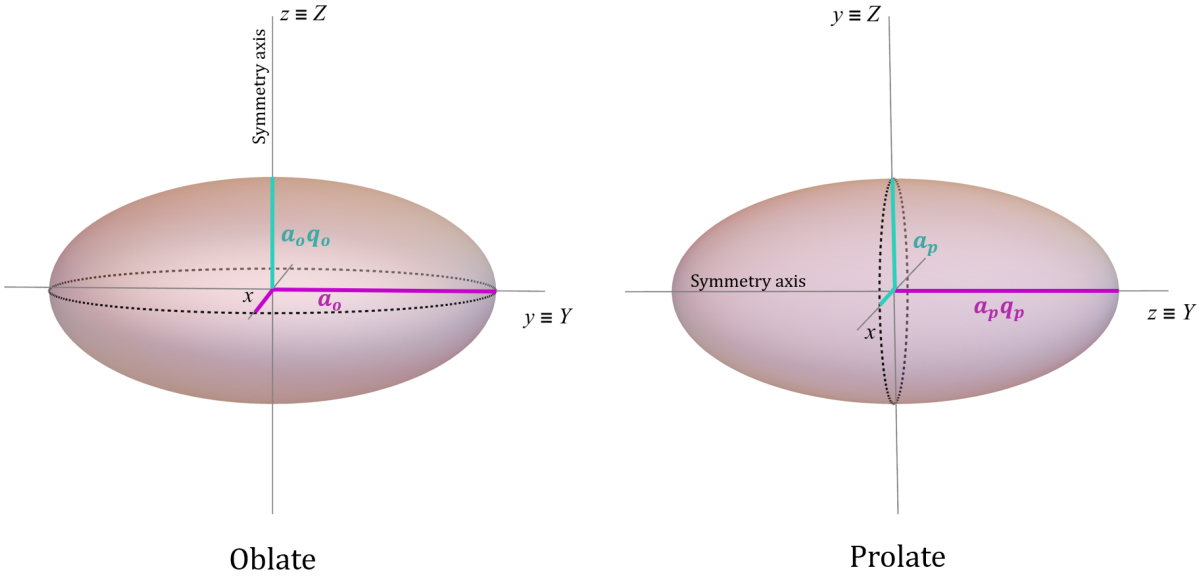

Figure 2.2. Example of two ellipsoidal surfaces, one oblate (left) and one prolate (right), satisfying (2.1) for a fixed m and conditions (2.7), (2.10) and (2.11). They are viewed close to edge-on and oriented in the same way, so that, in the oblate case $y \equiv Y$ and $z \equiv Z$, and in the prolate case $y \equiv Z$ and $z \equiv Y$, where we have uniquely denoted the projection plane as (Y, Z).

To simplify the notation, from now on, when not strictly necessary, we will drop the subscript "o" a and "p" and simply use the generic a and q.

We conclude this section with an example that aims to illustrate, even if only for a simple case, the validity of the considerations done. We consider two conjugate systems with a Gaussian density profile,

$$\rho(m) = \frac{M}{a^3 q \pi^{3/2}} e^{-m^2}, \tag{2.15}$$

whose surface density can be easily computed analytically, obtaining

$$\Sigma(l) = \frac{M}{a^2 q \pi} e^{-l^2}. \tag{2.16}$$

Figure 2.3 shows the comparison of ρ and Σ for the oblate and the prolate system, with axial ratio of the oblate (prolate) system $q_o = 1/2$ ($q_p = 2$). As expected, the two ellipsoids have indistinguishable projection and the prolate system is denser than the oblate one.

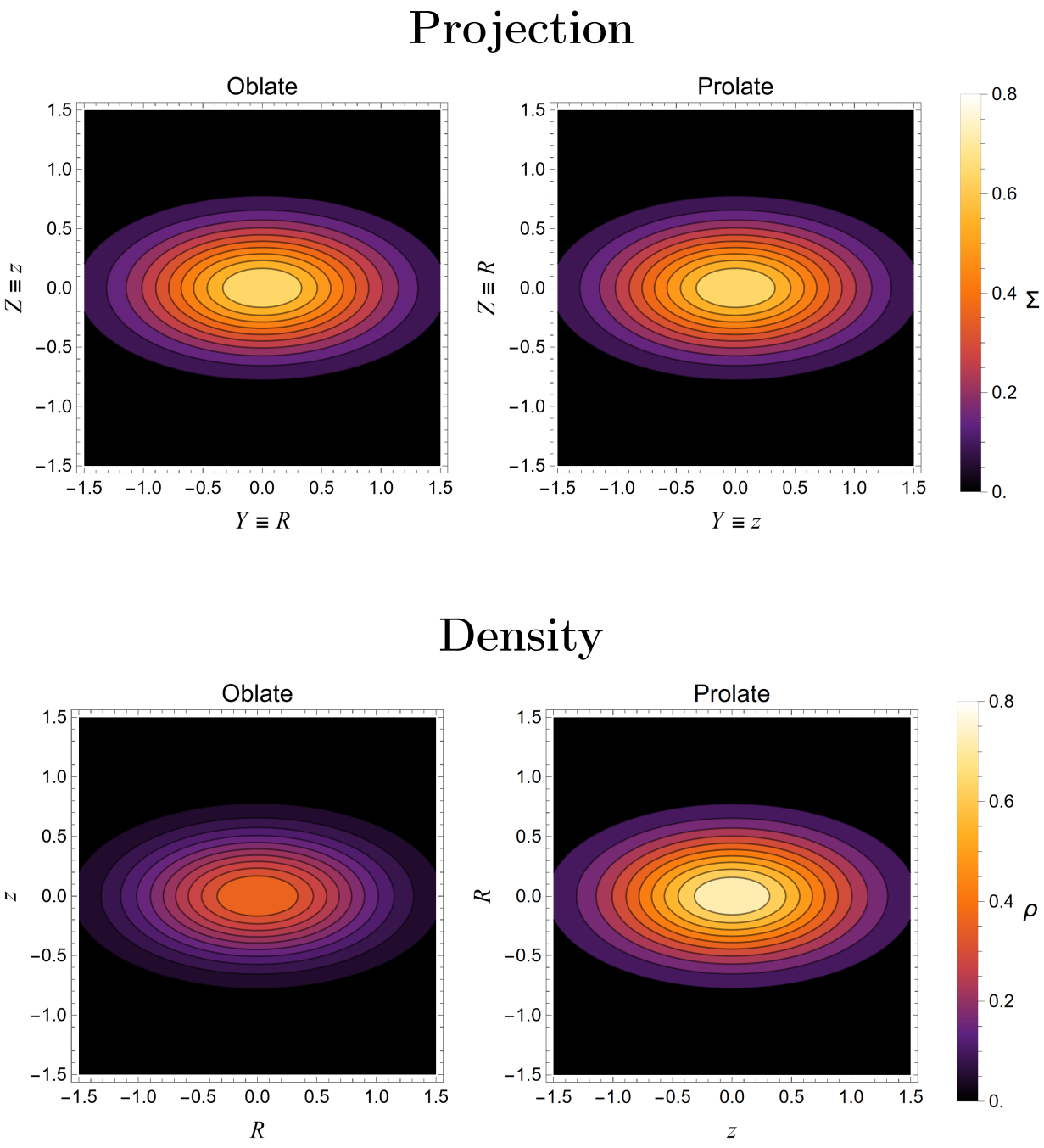

Figure 2.3. The upper panels show the surface density, in the (Y, Z) projection plane, of conjugate oblate (left) and prolate (right) systems with the Gaussian profile in equation (2.15) and axial ratio of the oblate ellipsoid $q_o = 1/2$ ($q_p = 2$). The surface density is in the common units M/a_o^2, where M is the total mass and a_o is the scale length of the oblate system. The lower panels show the intrinsic density profile in the (R, z) plane for the same pair of conjugate systems, in the common units M/a_o^3. In all plots, lengths are normalised to a_o.

To summarise, we have shown that it is possible to construct oblate and prolate ellipsoids which, when viewed edge-on, produce identical images. Consequently, it is impossible to determine, only through photometry, whether an axisymmetric galaxy is intrinsically oblate or prolate. In breaking this degeneracy the analysis of their dynamics and the identification of possible kinematical signatures that characterise the two shapes is essential. This topic will be addressed in detail in the following chapters.

CHAPTER 3

The Tensor Virial Theorem for Axisymmetric Ellipsoids

As discussed in Chapter 2, our final task is to understand what kind of dynamical differences can characterise conjugate oblate and prolate systems. However, before focusing on the specific case of conjugate pairs, we ask whether some general differences between oblate and prolate systems exist. This broader question will reveal important results that will also allow for a better understanding of conjugate pairs.

In this chapter, we introduce the Tensor Virial Theorem (Section 3.1) to investigate their global dynamical and energetic properties, and apply it first to general axisymmetric systems with density $\rho(m)$ (Section 3.1.1), and then to conjugate pairs (Section 3.1.2).

3.1 The Tensor Virial Theorem

A useful tool when studying self-gravitating systems in equilibrium is the Tensor Virial Theorem (TVT). It is a generalisation of the scalar virial theorem and is derived by multiplying the JEs (see Chapter 4) by the spatial coordinates and integrating over the whole configuration space (for further details see Binney and Tremaine 2008, Ciotti 2021).

In a general ellipsoidal system with density $\rho(\mathbf{x})$, the *second-order mass tensor* is given by

$$I_{ij} \equiv \int_{\mathbb{R}^3} \rho x_i x_j d^3\mathbf{x}. \tag{3.1}$$

Moreover, the *streaming* and *velocity dispersion kinetic energy tensors* are given, respectively, by

$$T_{ij} \equiv \frac{1}{2}\int_{\mathbb{R}^3} \rho \overline{v_i}\ \overline{v_j} d^3\mathbf{x}, \quad \Pi_{ij} \equiv \int_{\mathbb{R}^3} \rho \sigma_{ij}^2 d^3\mathbf{x}, \tag{3.2}$$

where $\overline{v_i}(\mathbf{x})$ is the mean velocity of stars along the i-th direction, obtained as a weighted average over the DF, and $\sigma_{ij}^2(\mathbf{x})$ denotes the ij component of the velocity dispersion tensor (see Appendix A). It is often convenient to also introduce the *total kinetic energy tensor*, given by

$$K_{ij} \equiv T_{ij} + \frac{1}{2}\Pi_{ij} = \frac{1}{2}\int_{\mathbb{R}^3} \rho \overline{v_i v_j} d^3\mathbf{x}. \tag{3.3}$$

Finally, calling Φ the total (e.g., including both stellar and dark matter contributions) potential, the *potential energy tensor* is given by

$$W_{ij} \equiv -\int_{\mathbb{R}^3} \rho x_i \frac{\partial \Phi}{\partial x_j} d^3\mathbf{x}. \tag{3.4}$$

For simplicity, in all this work, we limit ourselves to self-gravitating systems, where density and potential are related by the Poisson equation

$$\triangle\Phi(\mathbf{x}) = 4\pi G\rho(\mathbf{x}). \tag{3.5}$$

With the definitions given above, the TVT takes the form:

$$\frac{1}{2}\frac{\partial^2 I_{ij}}{\partial t^2} = 2T_{ij} + \Pi_{ij} + W_{ij}. \tag{3.6}$$

Under the assumption of stationary system (which is typically the case for galaxies), the left-hand side vanishes, thus the TVT reduces to

$$W_{ij} = -2T_{ij} - \Pi_{ij}, \tag{3.7}$$

or, equivalently,

$$W_{ij} = -2K_{ij} \tag{3.8}$$

This relation highlights how the global dynamical properties of a system (right-hand side) are linked to its inner structure (left-hand side).

Let us consider a general triaxial ellipsoid with density $\rho(m)$, with

$$m^2 = \frac{x^2}{a_1^2} + \frac{y^2}{a_2^2} + \frac{z^2}{a_3^2}. \tag{3.9}$$

It can be shown (see Roberts 1962) that $W_{ij} = 0$ for $i \neq j$ and the diagonal terms W_{ii} can be computed from the following non-trivial identity:

$$W_{ii} = -G\pi^2 a_1 a_2 a_3 a_i^2 w_i H, \tag{3.10}$$

where no summing over repeated indices is intended. The quantity H is defined as

$$H \equiv \int_0^\infty F(m)^2 dm, \quad F(m) \equiv 2\int_m^\infty t\rho(t)dt \tag{3.11}$$

and the functions w_i are given by

$$w_i \equiv a_1 a_2 a_3 \int_0^\infty \frac{d\tau}{(a_i^2+\tau)\sqrt{\Delta(\tau)}}, \quad \Delta(\tau) \equiv (a_1^2+\tau)(a_2^2+\tau)(a_3^2+\tau). \tag{3.12}$$

The definitions and relations above are entirely general and hold for any triaxial ellipsoidal system with $\rho = \rho(m)$. In the following, we will restrict our attention to axisymmetric systems discussing first general oblate and prolate systems, and then turning to the analysis of the more specific conjugate oblate-prolate pairs, defined in Chapter 2.

3.1.1 General axisymmetric ellipsoidal systems

Let us consider axisymmetric ellipsoidal systems with $\rho = \rho(m)$, where m is given in equation (2.1). In this case, $a_1 = a_2 = a$ and $a_3 = aq$, so that

$$W_{ii} = -G\pi^2 a^3 q a_i^2 w_i H \tag{3.13}$$

and

$$w_i = a^3 q \int_0^\infty \frac{d\tau}{(a_i^2+\tau)\sqrt{\Delta(\tau)}}, \quad \Delta(\tau) = (a^2+\tau)^2(a^2q^2+\tau). \tag{3.14}$$

The explicit expression of w_i for axisymmetric systems can be obtained in terms of elementary functions[1] and it is given in Appendix B.

In equation (3.13), since H is the same for $i = 1, 2, 3$, it simplifies in ratios such as W_{ii}/W_{jj} which are, thus, *independent* of the density profile and depend only on the axial ratio. This makes them particularly useful to gain insight into the self-gravity of ellipsoidal systems, without requiring any specific assumption on the density profile. In particular, we consider the ratio between the radial component of the potential energy tensor, given

[1] In the triaxial case the w_i functions contain elliptic integrals (see equation (3.12) in Ciotti 2021).

by

$$\begin{aligned} W_{RR} &= W_{xx} + W_{yy} = \\ &= -\int_{\mathbb{R}^3} \rho \left(\frac{\partial \Phi}{\partial x} x + \frac{\partial \Phi}{\partial y} y \right) d^3\mathbf{x} = \\ &= -\int_{\mathbb{R}^3} \rho \left(\frac{\partial \Phi}{\partial R} \frac{x^2}{R} + \frac{\partial \Phi}{\partial R} \frac{y^2}{R} \right) d^3\mathbf{x} = \\ &= -\int_{\mathbb{R}^3} \rho \frac{\partial \Phi}{\partial R} R d^3\mathbf{x} \end{aligned} \tag{3.15}$$

and the z-component,

$$W_{zz} = -\int_{\mathbb{R}^3} \rho \frac{\partial \Phi}{\partial z} z d^3\mathbf{x}. \tag{3.16}$$

Note that, in axisymmetric systems,

$$w_1 = w_2, \quad W_{xx} = W_{yy}, \tag{3.17}$$

thus, from equation (3.13), we have that

$$W_{RR} = -2G\pi^2 a^5 q w_1 H, \quad W_{zz} = -G\pi^2 a^5 q^3 w_3 H. \tag{3.18}$$

We can now write W_{RR}/W_{zz} as a function of the axial ratio. In the oblate case, we have

$$\frac{W_{RR}}{W_{zz}} = \frac{1}{q^2} \left(\frac{\arcsin\sqrt{1-q^2}}{\sqrt{1-q^2}} - q \right) \left(\frac{1}{q} - \frac{\arcsin\sqrt{1-q^2}}{\sqrt{1-q^2}} \right)^{-1}, \quad q < 1, \tag{3.19}$$

while, in the prolate case,

$$\frac{W_{RR}}{W_{zz}} = \frac{1}{q^2} \left(q - \frac{\operatorname{arctanh}\frac{\sqrt{q^2-1}}{q}}{\sqrt{q^2-1}} \right) \left(\frac{\operatorname{arctanh}\frac{\sqrt{q^2-1}}{q}}{\sqrt{q^2-1}} - \frac{1}{q} \right)^{-1}, \quad q > 1. \tag{3.20}$$

Figure 3.1 shows the behaviour of W_{RR}/W_{zz} as a functions of q for oblate and prolate systems. As expected, when the system is spherical ($q = 1$), $W_{xx} = W_{yy} = W_{zz}$, so that $W_{RR}/W_{zz} = 2$. As the shape departs from sphericity, the behaviour of W_{RR}/W_{zz} differs significantly between oblate and prolate systems.

In oblate systems, for any axial ratio q, $W_{RR}/W_{zz} > 2$ and increases for increasing flattening. Conversely, in prolate systems, as they become more elongated, the value of W_{RR}/W_{zz} monotonically decreases toward zero. Therefore, calling q_{crit} the axial ratio of prolate systems for which $W_{RR}/W_{zz} = 1$, for systems less elongated than q_{crit} ($q < q_{\text{crit}}$), $W_{RR} > W_{zz}$, while for systems more elongated than q_{crit} ($q > q_{\text{crit}}$), $W_{zz} > W_{RR}$. For sufficiently large q, W_{zz} can become arbitrarily larger than W_{RR}. This is particularly surprising, given that W_{RR} is the sum of two contributions (x and y), yet it can be outweighed by the single z-term. The value of q_{crit}, obtained by numerically solving equation (3.20) for $W_{RR}/W_{zz} = 1$, is $q_{\text{crit}} \approx 2.59$. In the figure, for convenience, W_{RR}/W_{zz} for prolate systems is plotted as a function of $1/q$. Therefore, in the plot, the critical value $q_{\text{crit}} \approx 2.59$ corresponds to $1/q_{\text{crit}} \approx 0.386$.

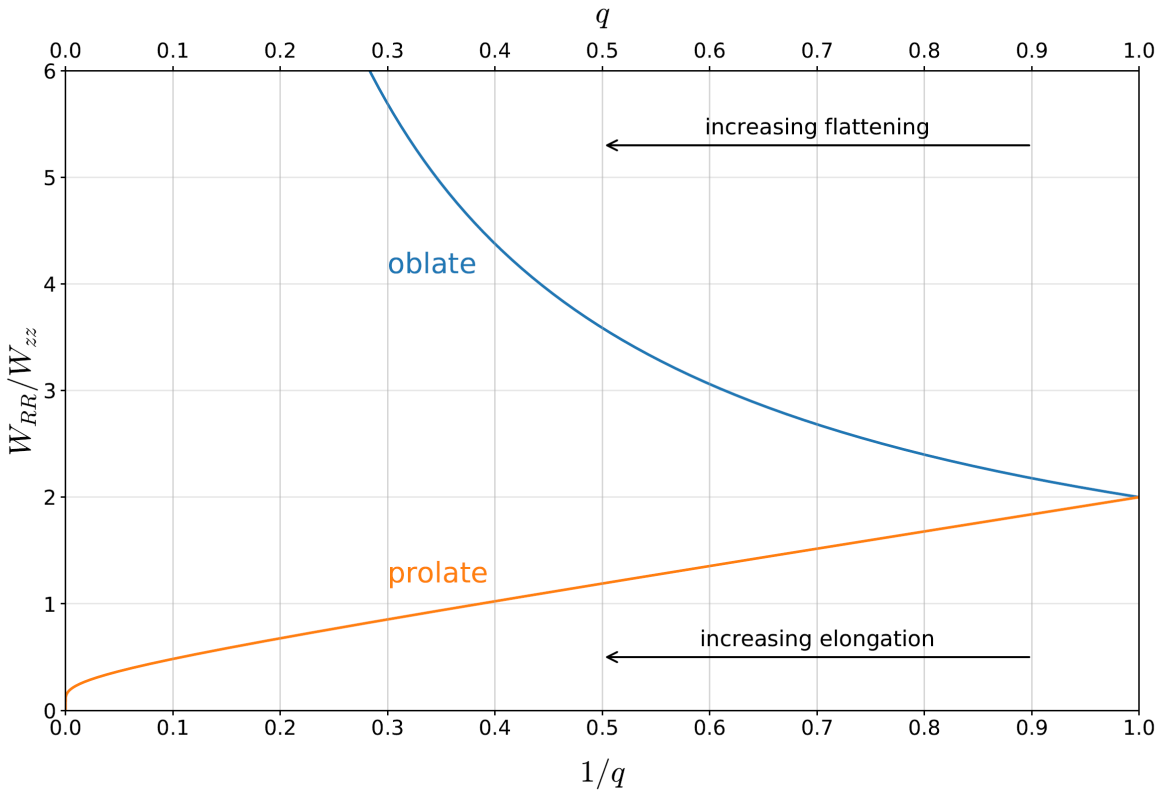

Figure 3.1. Ratio W_{RR}/W_{zz} for oblate (blue) and prolate (orange) systems. For oblate systems ($q < 1$) the ratio is shown as a function of q, while for prolate systems ($q > 1$) it is shown as a function of $1/q$. Moving from right to left, oblate ellipsoids become more flattened and prolate ellipsoids more elongated.

Being W_{RR} the sum of two equal contributions, it is also instructive to isolate one of the two and compare it directly with W_{zz}. For this reason, in Figure 3.2 we show the behaviour of W_{xx}/W_{zz} as a function of the axial ratio. Clearly, this is just half of the previously discussed ratio W_{RR}/W_{zz}, and therefore it contains the same information. However, its plot allows us to better understand and visualise the energy contribution along the individual directions, which can help us making some further considerations.

In particular, we observe that, in oblate systems, for any value of q, $W_{xx} > W_{zz}$, while the opposite holds in prolate systems. This raises a quite natural question which is whether, for a given oblate system with axial ratio q, the ratio W_{xx}/W_{zz} is equal to W_{zz}/W_{xx} in prolate systems with axial ratio $1/q$; in other words, whether prolate systems can, in this sense, be regarded simply as oblate systems with an "inverted" axial ratio.

A simple series expansion for $q \to 0$ shows that this is not the case. However, in the limit of nearly spherical systems this idea of reciprocity can be considered a good approximation. This behaviour is illustrated by the black dashed line in the figure, which represents the product of the two curves. If the ratio W_{xx}/W_{zz} for oblate systems were equal to W_{zz}/W_{xx} for prolate systems, the product of the ratios W_{xx}/W_{zz} would remain identically equal to unity for all axial ratios. Instead, the plot reveals that this condition is satisfied only in the regime of small flattenings/elongations. This indicates that, oblate and prolate systems are *not energetically "inverted" systems.*

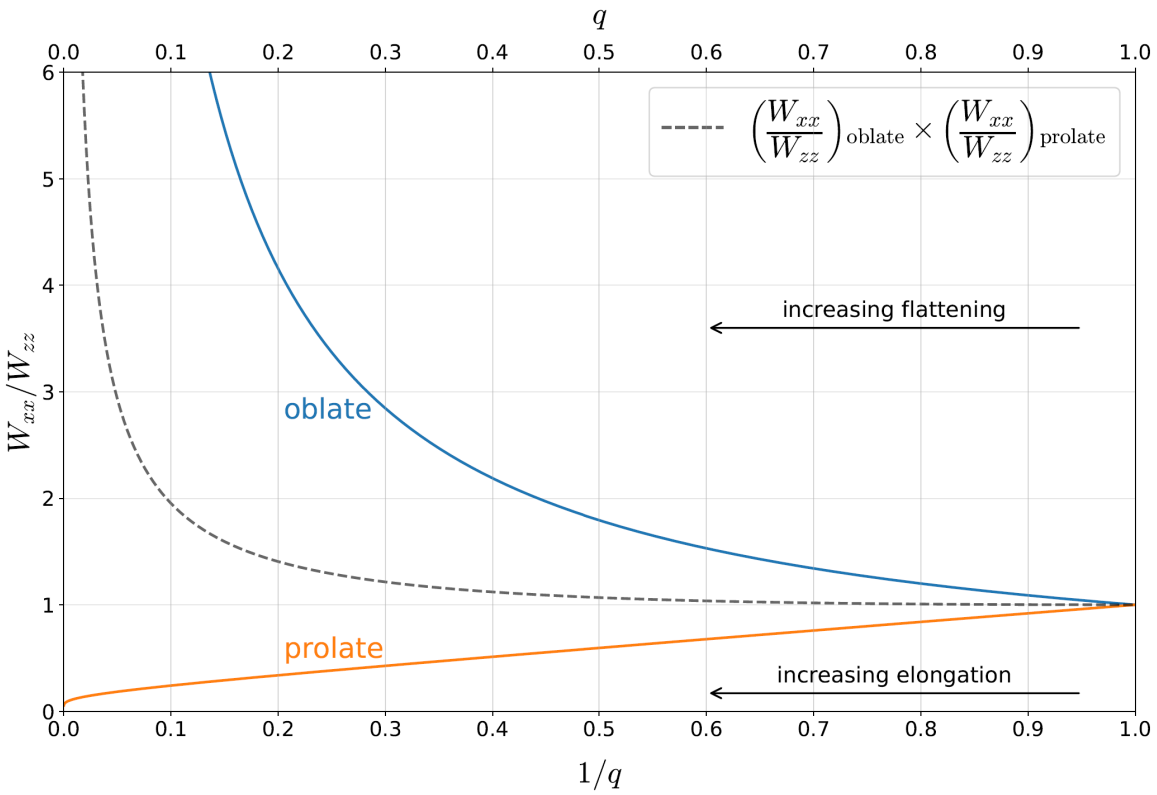

Figure 3.2. Ratio W_{xx}/W_{zz} for oblate (blue) and prolate (orange) systems. For oblate systems ($q < 1$) the ratio is shown as a function of q, while for prolate systems ($q > 1$) it is shown as a function of $1/q$. Moving from right to left, oblate ellipsoids become more flattened and prolate ellipsoids more elongated. The dashed black lines represents the product of the two curves.

If now we turn to consider the kinetic energy term of the TVT additional interesting information can be recovered. From equation (3.8), the ratio W_{RR}/W_{zz} is equal to

$$\frac{W_{RR}}{W_{zz}} = \frac{2K_{xx} + 2K_{yy}}{2K_{zz}} = \frac{\int_{\mathbb{R}^3} \rho(\overline{v_x^2} + \overline{v_y^2}) d^3\mathbf{x}}{\int_{\mathbb{R}^3} \rho \overline{v_z^2} d^3\mathbf{x}}. \tag{3.21}$$

Since we are studying axisymmetric systems, it is convenient to re-write equation (3.21) in cylindrical coordinates. One can easily verify that $\overline{v_x^2} + \overline{v_y^2} = \overline{v_R^2} + \overline{v_\varphi^2}$, thus we have

$$\frac{W_{RR}}{W_{zz}} = \frac{\int_{\mathbb{R}^3} \rho(\overline{v_R^2} + \overline{v_\varphi^2}) d^3\mathbf{x}}{\int_{\mathbb{R}^3} \rho \overline{v_z^2} d^3\mathbf{x}}. \tag{3.22}$$

Up to this point, no assumptions have been made regarding the dynamics of the systems.

Let us now restrict ourselves to classical two-integral systems, i.e., systems whose distribution function depends on the phase-space coordinates only through the classical two integrals of motion: the total energy E and the component L_z of the angular momentum along the symmetry axis (for a more detailed and extensive explanation, see Appendix A). In such systems, the velocity dispersion tensor is diagonal in cylindrical coordinates. The diagonal components σ_R^2, σ_z^2, σ_φ^2 are, respectively, the velocity dispersion of stars along the R, z and φ directions and are such that $\sigma_R^2 = \sigma_z^2 \equiv \sigma^2$. Moreover, in such systems, the

first-order velocity moments $\overline{v_R}$ and $\overline{v_z}$ vanish. Equation (3.22) thus becomes

$$\frac{W_{RR}}{W_{zz}} = \frac{\int_{\mathbb{R}^3} \rho(\sigma^2 + \overline{v_\varphi^2}) d^3\mathbf{x}}{\int_{\mathbb{R}^3} \rho\sigma^2 d^3\mathbf{x}} = 1 + \frac{\int_{\mathbb{R}^3} \rho\overline{v_\varphi^2} d^3\mathbf{x}}{\int_{\mathbb{R}^3} \rho\sigma^2 d^3\mathbf{x}}. \tag{3.23}$$

This expression shows that, in two-integral systems, $W_{RR}/W_{zz} \geq 1$.

We previously discussed that, in prolate ellipsoids, W_{RR}/W_{zz} takes values between 0 (infinitely elongated systems) and 2 (spherical systems). This result was obtained without making any assumptions on the dynamics of the system. Here, the condition $W_{RR}/W_{zz} \geq 1$ for the specific case of two-integral systems, implies that two-integral prolate systems cannot reach arbitrarily high elongations: their maximum possible axial ratio is $q_{\rm crit} \approx 2.59$ found before. We stress that this result holds *regardless of the specific density profile*.

It should be noted, however, that the existence of two-integral prolate systems with $q \leq q_{\rm crit}$ is not guaranteed and, unlike the general limit derived above, it *depends sensitively on the density profile*. This aspect cannot be treated with the TVT alone and requires a dedicated analysis, which will be the focus of Chapter 5.

Interestingly, unlike prolate systems, this issue does not arise in two-integral oblate systems, which have $W_{RR}/W_{zz} \geq 2$ increasing for increasing flattening. This implies that two-integral oblate systems can achieve arbitrary flattening, provided that the ratio

$$\frac{\int_{\mathbb{R}^3} \rho\overline{v_\varphi^2} d^3\mathbf{x}}{\int_{\mathbb{R}^3} \rho\sigma^2 d^3\mathbf{x}}$$

is sufficiently large.

Another important consideration concerns isotropic systems, where $\sigma_R^2 = \sigma_z^2 = \sigma_\varphi^2$. In this case, recalling that (see Appendix A)

$$\overline{v_\varphi^2} = \sigma_\varphi^2 + \overline{v_\varphi}^2, \tag{3.24}$$

equation (3.22) becomes

$$\frac{W_{RR}}{W_{zz}} = 2 + \frac{\int_{\mathbb{R}^3} \rho\overline{v_\varphi}^2 d^3\mathbf{x}}{\int_{\mathbb{R}^3} \rho\sigma^2 d^3\mathbf{x}}. \tag{3.25}$$

Therefore, this ratio is greater than 2 in isotropic systems. Since in prolate systems $W_{RR}/W_{zz} < 2$ for any axial ratio, isotropic prolate systems cannot exist. This, again, does not happen in oblate systems, which in principle can be isotropic and reach arbitrary flattenings.

These results highlight, once again, that oblate and prolate systems are not "two sides of the same coin": oblate systems seem to behave in a more predictable and "well-behaved" way, whereas prolate systems reveal unexpected and less intuitive properties.

Lastly, note that, since the specific scale length a simplifies in the ratio W_{RR}/W_{zz}, all the results of this section apply to general axisymmetric systems with arbitrary size. In particular, they remain valid in the specific case of conjugate systems. However, for conjugate pairs further aspects can be investigated. This will be the focus of the following section.

3.1.2 Conjugate systems

Having compared W_{zz} with W_{RR} within the same system and highlighted the main general differences between oblate and prolate systems, we next compare the same quantities across conjugate pairs. Specifically, we consider the ratios W^o_{zz}/W^p_{zz} and W^o_{RR}/W^p_{RR}, where "o" and "p" refer to the oblate and the prolate components of conjugate pairs, respectively. We point out that, when performing this computation, particular care is required: the scale lengths and the axial ratios of conjugate ellipsoids have to satisfy the conditions (2.7), (2.10) and (2.11), thus, differently from the previous case, a does not simplify. Moreover, note that, in this case, in equation (3.18), the value of H is not the same for the two configurations, since it depends not only on $\tilde{\rho}$ (which *is* the same), but also on the scaling coefficient of ρ which, as explained in Section 2.3, is different in oblate and prolate conjugate models in order to preserve the same surface brightness profile. Exploiting equation (2.4) and the condition (2.10), it is convenient to rewrite H in the following way:

$$H = \frac{M^2}{4\pi^2 a^6 q^2 \mathcal{M}^2} \int_0^\infty \left(\int_m^\infty t\tilde{\rho}(t)dt \right)^2 dm = \frac{\tilde{H}}{a^2}. \tag{3.26}$$

$\tilde{H}$ has now the same value in oblate and prolate conjugate systems and can therefore be simplified when computing W^o_{zz}/W^p_{zz} and W^o_{RR}/W^p_{RR}. The explicit expression of these ratios, expressed as a function of the axial ratio q_o of the oblate system, are the following:

$$\frac{W^o_{zz}}{W^p_{zz}} = q_o^3 \left(\frac{1}{q_o} - \frac{\arcsin\sqrt{1-q_o^2}}{\sqrt{1-q_o^2}} \right) \left(q_o \frac{\operatorname{arctanh}\sqrt{1-q_o^2}}{\sqrt{1-q_o^2}} - q_o \right)^{-1}, \tag{3.27}$$

$$\frac{W^o_{RR}}{W^p_{RR}} = \frac{1}{q_o} \left(q_o - \frac{\arcsin\sqrt{1-q_o^2}}{\sqrt{1-q_o^2}} \right) \left(q_o \frac{\operatorname{arctanh}\sqrt{1-q_o^2}}{\sqrt{1-q_o^2}} - \frac{1}{q_o} \right)^{-1}. \tag{3.28}$$

Figure 3.3 illustrates the behaviour of these ratios for different axial ratios q_o. We observe that, $W^o_{RR} > W^p_{RR}$ for any q_o and increases for increasing flattening/elongations of the conjugate pair. For $q_o \to 0$, the ratio $W^o_{RR}/W^p_{RR} \to \pi/2$. Conversely, $W^o_{zz} < W^p_{zz}$ for any q_o and the ratio $W^o_{zz}/W^p_{zz} \to 0$ as $q_o \to 0$. This outcome is not trivial, since the relative behaviour of W_{zz} and W_{RR} depends sensitively on the definition of conjugate systems, which is based on the relation between their scale lengths.

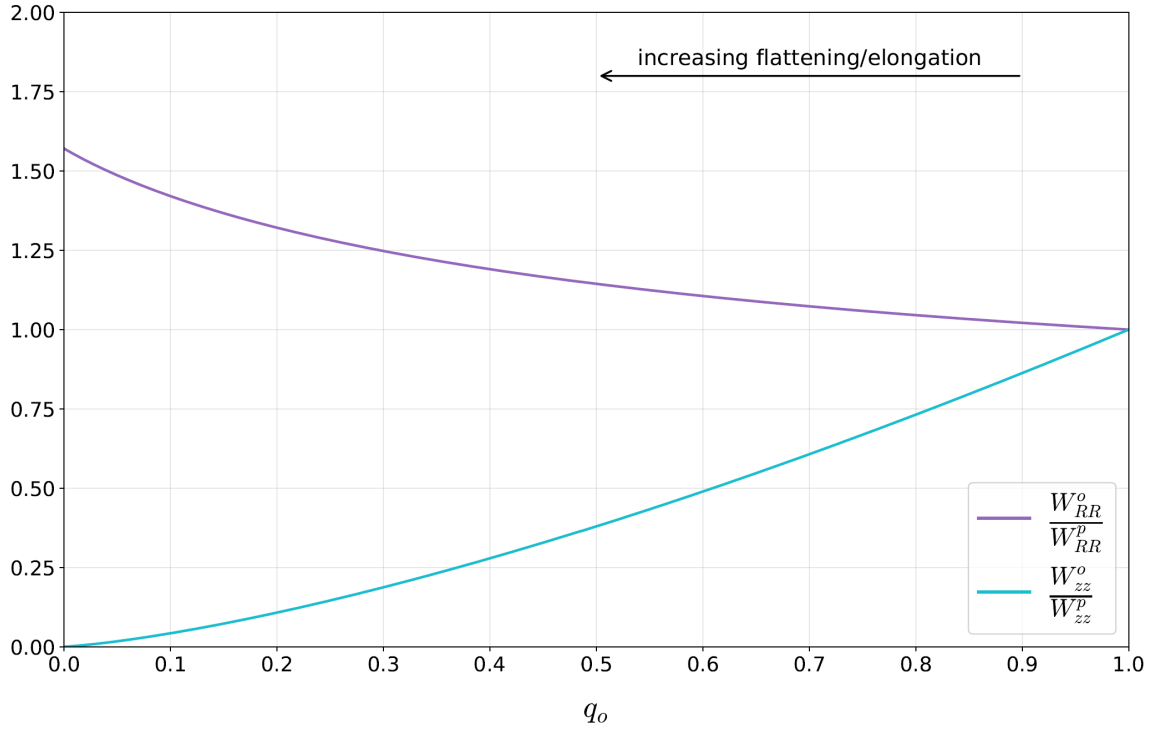

Figure 3.3. W^o_{RR}/W^p_{RR} (in purple) and W^o_{zz}/W^p_{zz} (in cyan), as a function of the axial ratio q_o of the oblate system. Going from right to left the oblate ellipsoid flattens and the prolate one becomes more elongated.

CHAPTER 4

Force Fields and Jeans Equations

The results of the previous chapter have been obtained by inspection of *global* properties of axisymmetric systems, i.e., the virial quantities, an approach that has proved to be particularly useful. Among the results that can be proved with this method, two stand out for being especially surprising: classical two-integral prolate systems cannot have arbitrary elongation and isotropic prolate systems cannot exist. The Virial Theorem involves, by construction, "averages" over the whole system, and so it is not immediately clear *why* prolate systems are subject to such constraints, while oblate systems are not.

Furthermore, in this context, a question may arise. As discussed in the previous chapter, two-integral systems have the same velocity dispersion along the two principal directions of the meridional plane. How, then, can the system sustain a flattened or elongated shape? For oblate systems an intuitive explanation is that they are flattened by rotation. For prolate systems, however, rotation does not provide a viable explanation. This is precisely what makes the physics of prolate systems difficult to grasp already at a very basic level.

To address these questions, it is necessary to reconsider the problem from a more fundamental perspective, examining *local* properties of axisymmetric ellipsoids. This chapter is devoted to this goal. In Section 4.1, we will recall the expression for the potential of axisymmetric ellipsoidal systems. Then, we will revisit an argument originally due to Newton in his study of the shape of the Earth (e.g. Chandrasekhar 1969), which provides a simple yet powerful interpretative tool for understanding equilibrium in fluid homogeneous axisymmetric systems. In Section 4.1.2, we will then extend this reasoning to systems with general density distributions $\rho(m)$. Finally, in Section 4.2, we will introduce the JEs and explain the role of dynamics in the equilibrium of axisymmetric systems.

4.1 The gravitational field of axisymmetric ellipsoids

Consider a generic two-integral axisymmetric system in equilibrium with density $\rho(m)$, where m is given in (2.1). What is it that allows it to be flattened or elongated in the meridional plane? A (tempting) intuitive idea is that at each isodensity surface m, the gravitational field $\mathbf{g}$, in the direction of the elongation, is weaker than that in the direction along which the system is more compact, as shown in Figure 4.1, and so maybe $\sigma_R^2 = \sigma_z^2$ elongates the system in the direction of the weaker field. As we will see in this chapter, the gravitational field actually behaves as expected, but the origin of the prolate vs. oblate shape is more complicated.

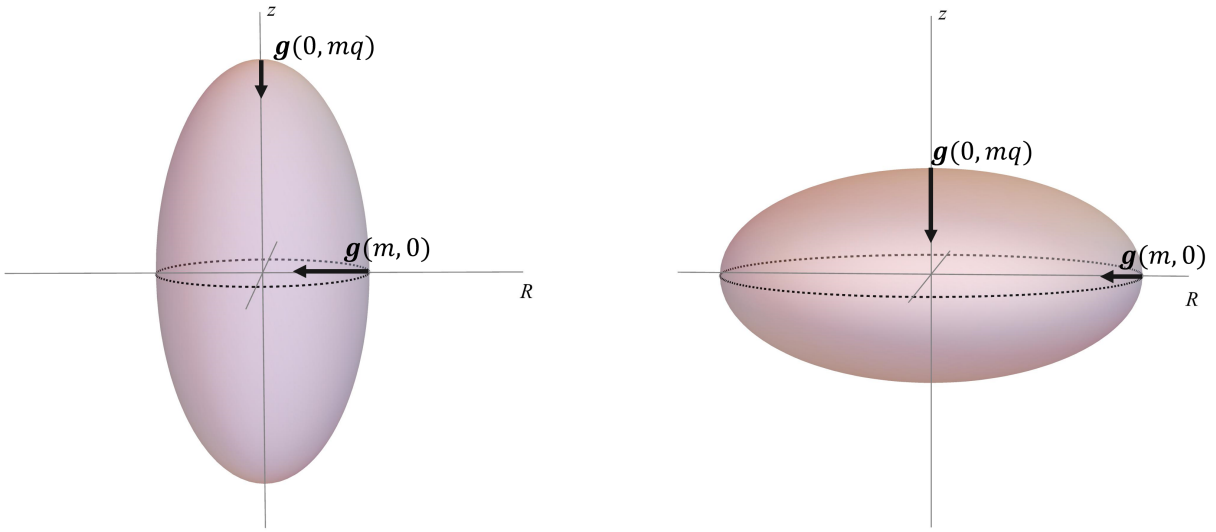

Figure 4.1. Qualitative representation of the intensity of the gravitational field $\mathbf{g}$ in axisymmetric systems. In the prolate ellipsoid (left), $\mathbf{g}$ is weaker along z and stronger along R. In the oblate ellipsoid (right), $\mathbf{g}$ is weaker along R and stronger along z.

Before proceeding with the description of Newton's approach, let us recall the expression for the potential produced by systems with density $\rho(m)$ (see Chandrasekhar 1969, see also Binney and Tremaine 2008 and Ciotti 2021). This is given by

$$\Phi(R,z) = -G\pi a^3 q \int_0^\infty \frac{F(m_\tau)}{\sqrt{\Delta(\tau)}} d\tau, \tag{4.1}$$

where the function F is defined as in (3.11), and

$$m_\tau^2 = \frac{R^2}{a^2+\tau} + \frac{z^2}{a^2q^2+\tau}. \tag{4.2}$$

At each point (R,z) of the system, the gravitational field is

$$\mathbf{g}(R,z) = -g_R \hat{\mathbf{e}}_\mathbf{R} - g_z \hat{\mathbf{e}}_\mathbf{z} \tag{4.3}$$

where $\hat{\mathbf{e}}_\mathbf{R}$ and $\hat{\mathbf{e}}_\mathbf{z}$ are the unit vectors along the R and z directions, respectively, and the

components g_R and g_z are:

$$\begin{cases} g_R(R,z) = \dfrac{\partial \Phi}{\partial R} = 2\pi G a^3 q R \displaystyle\int_0^\infty \frac{\rho_\tau d\tau}{(a^2+\tau)\sqrt{\Delta(\tau)}}, \\ g_z(R,z) = \dfrac{\partial \Phi}{\partial z} = 2\pi G a^3 q z \displaystyle\int_0^\infty \frac{\rho_\tau d\tau}{(a^2 q^2+\tau)\sqrt{\Delta(\tau)}}, \end{cases} \tag{4.4}$$

where $\rho_\tau = \rho(m_\tau)$.

In the special case of constant-density ellipsoids with density ρ_0, g_R and g_z become

$$\begin{cases} g_R(R,z) = \dfrac{\partial \Phi}{\partial R} = 2\pi G a^3 q R \rho_0 \displaystyle\int_0^\infty \frac{d\tau}{(a^2+\tau)\sqrt{\Delta(\tau)}} = 2\pi G R \rho_0 w_1, \\ g_z(R,z) = \dfrac{\partial \Phi}{\partial z} = 2\pi G a^3 q z \rho_0 \displaystyle\int_0^\infty \frac{d\tau}{(a^2 q^2+\tau)\sqrt{\Delta(\tau)}} = 2\pi G z \rho_0 w_3, \end{cases} \tag{4.5}$$

where w_1 and w_3 are defined in (3.12). The reference to constant-density ellipsoids is more important than what appears at first sight. In fact, Newton's argument, which we intend to adopt and which will be described in the next section, concerns fluid homogeneous ellipsoids.

4.1.1 A fluid analogue: Newton's homogeneous axisymmetric ellipsoid

When investigating the shape of the Earth, Newton proposed the following argument. He assumes that the Earth is a homogeneous oblate ellipsoid with density ρ_0 and with rigid-body rotation. Then, he imagines drilling a hole from a point of the equator to the centre of the Earth and a similar hole from the pole to the centre, as shown in Figure 4.2. He

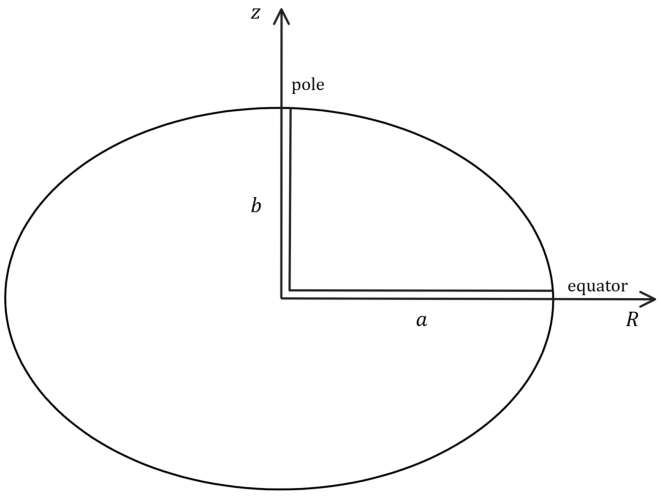

Figure 4.2. Illustration of an oblate ellipsoid, inspired by Newton's depiction in the *Philosophiæ Naturalis Principia Mathematica* when discussing the rotational flattening of the Earth.

then assumes that the holes are filled with a fluid of density ρ_0. Since the system is in equilibrium, the weight of the vertical and horizontal columns of fluid must be equal. We call a the length of the radial column and b the length of the vertical one. The weight of the vertical column is

$$\int_0^b \rho_0 g_z dz = \rho_0 \frac{b}{2} g_{\rm pole}, \tag{4.6}$$

where the equality follows from equation (4.5) and $g_{\rm pole}$ is the intensity of the gravitational field at the pole. Along the radial direction, considering only the density and the gravitational field, the weight of the column is

$$\int_0^a \rho_0 g_z dz = \rho_0 \frac{a}{2} g_{\rm eq}, \tag{4.7}$$

where $g_{\rm eq}$ is the gravitational field at the equator. However, we must also take into account the centrifugal support. Its effect is that of reducing the radial weight and, since both the gravitational field and the centripetal acceleration scale linearly with R, the effective weight of the radial column is

$$\rho_0 \frac{a}{2} g_{\rm eq}(1-f), \tag{4.8}$$

where $f > 0$ is a "reduction" factor defined as the ratio between the centripetal acceleration at the equator and the gravitational field at the equator. From (4.6) and (4.8), the equilibrium of the fluid implies

$$\rho_0 \frac{b}{2} g_{\rm pole} = \rho_0 \frac{a}{2} g_{\rm eq}(1-f), \tag{4.9}$$

which gives

$$1 - f = q \frac{g_{\rm pole}}{g_{\rm eq}}, \quad q \equiv \frac{b}{a} < 1 \tag{4.10}$$

From equation (4.5) we have

$$\frac{g_{\rm pole}}{g_{\rm eq}} = q \frac{w_3}{w_1}, \tag{4.11}$$

and substituting w_1 and w_3 with their expansion for small flattening, given in equation (3.13) of Ciotti (2021), we find

$$\frac{g_{\rm pole}}{g_{\rm eq}} \approx 1 + \frac{\eta}{5}, \quad \eta \equiv 1 - q. \tag{4.12}$$

We then substitute this result in equation (4.10), finding

$$1 - f \approx 1 - \frac{4\eta}{5}. \tag{4.13}$$

We conclude that some rotation is needed in order to keep the system in equilibrium. The amount of rotation is related to the flattening of the system through the relation

$$f \approx \frac{4\eta}{5}. \tag{4.14}$$

Now, in analogy with the oblate case, let us consider a prolate homogeneous ellipsoid

as in Figure 4.3 with density ρ_0. As we did for the oblate case, we imagine drilling a hole from the pole to the centre and another hole from the equator to the centre. In this case, we call a the length of the vertical column and b the length of the radial one. The two columns are filled with a fluid of density ρ_0.

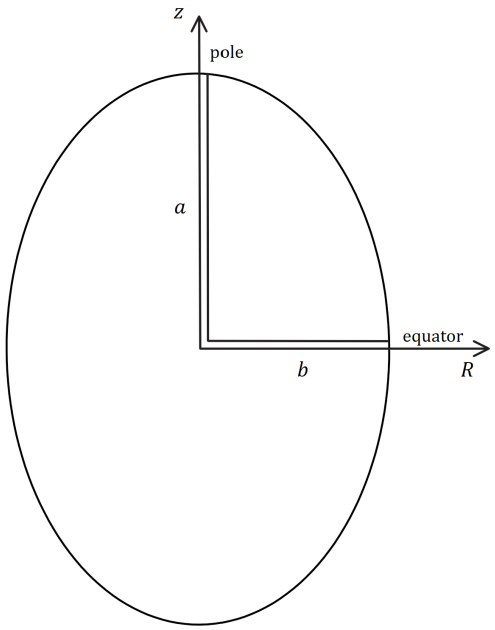

Figure 4.3. Illustration of a prolate ellipsoid, inspired by Newton's depiction in the *Philosophiæ Naturalis Principia Mathematica* when discussing the rotational flattening of the Earth.

Now, the weight of the vertical column of fluid is

$$\rho_0 \frac{a}{2} g_{\text{pole}}, \tag{4.15}$$

while the effective weight of the horizontal column is

$$\rho_0 \frac{b}{2} g_{\text{eq}} (1 - f). \tag{4.16}$$

Since the fluid is in equilibrium, we have again

$$1 - f = q \frac{g_{\text{pole}}}{g_{\text{eq}}}, \tag{4.17}$$

but this time,

$$q \equiv \frac{a}{b} > 1. \tag{4.18}$$

so that $\eta < 0$. Expanding for small elongations, we have

$$\frac{g_{\text{pole}}}{g_{\text{eq}}} \approx 1 - \frac{|\eta|}{5}, \tag{4.19}$$

and

$$1 - f = 1 + \frac{4|\eta|}{5}. \tag{4.20}$$

Being $f > 0$, equation (4.20) is never satisfied. Consequently, no homogeneous, fluid prolate system can be in equilibrium.
The main conclusion that one draws from this approach is that, at variance with what intuition might suggest, comparing the gravitational field at the pole and at the equator is not sufficient to assess the system's equilibrium. In the oblate case, although equation (4.12) shows that $g_{\text{pole}} > g_{\text{eq}}$, when we consider the weights of the vertical and radial columns, which depend on both gravitational field and length of the column, we find that the longer radial column actually dominates. Some degree of rotation is thus required to reduce its weight. In the prolate case, the situation is reversed: despite $g_{\text{pole}} < g_{\text{eq}}$, the vertical column outweighs the radial one. However, in this case, rotation cannot compensate for this effect; on the contrary, it makes it worse. It is, therefore, this inability to balance the two columns through rotation that ultimately makes fluid prolate systems unfeasible.

4.1.2 General axisymmetric systems with $\rho(m)$

The usefulness of Newton's approach lies in translating the problem of equilibrium into a very simple yet enlightening balance-of-weights argument. Even though it was originally devised for homogeneous rotating fluids with small flattening/elongation, we now ask whether the same intuition extends to more general ellipsoidal systems with arbitrary axial ratio and a stratified density $\rho(m)$. If such an extension were possible, it could help us, as in the constant-density ellipsoid, to visualise in a simple way the intrinsic difference between oblate and prolate systems. To this end, in the following, we present a set of results that show in a rigorous way how Newton's intuitive reasoning can be generalised to arbitrary density profiles $\rho(m)$.

Theorem 1. *Let*

$$m^2 = R^2 + \frac{z^2}{q^2}, \quad q > 0, \tag{4.21}$$

and let the density of an axisymmetric ellipsoidal system be $\rho = \rho(m)$, with

$$\frac{d\rho}{dm} \leq 0. \tag{4.22}$$

Let $g_R(R, z)$ and $g_z(R, z)$ be the magnitude of the gravitational field of the ellipsoid along R and z, respectively, at the point (R, z). Then, $\forall m$,

$$\begin{aligned} g_R(m, 0) &< g_z(0, mq) \quad \textit{if} \quad q < 1 \ \textit{(oblate)}, \\ g_R(m, 0) &> g_z(0, mq) \quad \textit{if} \quad q > 1 \ \textit{(prolate)}. \end{aligned} \tag{4.23}$$

Proof. See Appendix C. □

This first result confirms, for both constant and decreasing density profiles $\rho(m)$, the intuitive picture of Figure 4.1: at a fixed m, gravity is stronger along the shortest axis and weaker along the longest axis. As we discussed, however, this alone does not explain

equilibrium in axisymmetric systems. Therefore, we also extend the analogy of the two columns of fluid to general ellipsoids with stratified density $\rho(m)$. We begin by presenting, in Theorem 2, an expression for the difference between the "weight" of the vertical column and that of the radial column, for truncated ellipsoids. This expression can be easily extended to the case of untruncated ellipsoids by taking the truncation radius to infinity. In addition to what done by Newton, our expression compares the vertical and the horizontal column not only at the centre of the system, but at every point (R, z). For illustrative purposes, Figure 4.4 shows an example of the radial and vertical columns at a generic point (R, z).

Theorem 2. *Let*

$$m^2 = R^2 + \frac{z^2}{q^2}, \quad q > 0, \tag{4.24}$$

and let the density of an axisymmetric ellipsoidal system be

$$\rho = \begin{cases} \rho(m) & m \leq m_t, \\ 0 & m > m_t. \end{cases} \tag{4.25}$$

where $m_t > 0$ is a truncation radius. Then, defining

$$R_t(z) = \sqrt{m_t^2 - \frac{z^2}{q^2}}, \quad z_t(R) = q\sqrt{m_t^2 - R^2}, \tag{4.26}$$

the following relation holds $\forall (R, z)$:

$$\begin{aligned} \int_R^{R_t} \rho \frac{\partial \Phi}{\partial R'} dR' - \int_z^{z_t} \rho \frac{\partial \Phi}{\partial z'} dz' = \int_R^{R_t} \int_z^{z_t} \left(\frac{\partial \rho}{\partial R'} \frac{\partial \Phi}{\partial z'} - \frac{\partial \rho}{\partial z'} \frac{\partial \Phi}{\partial R'} \right) dz' dR' \\ + \int_R^{R_t} \rho(R', z_t') \frac{d\Phi(R', z_t')}{dR'} dR'. \end{aligned} \tag{4.27}$$

Proof. See Appendix C. □

Note that

$$\int_R^{R_t} \rho \frac{\partial \Phi}{\partial R'} dR' \equiv \mathcal{W}_R, \quad \int_z^{z_t} \rho \frac{\partial \Phi}{\partial z'} dz' \equiv \mathcal{W}_z$$

are, respectively, the weights of the radial and the vertical density column at each point (R, z). From now on, we will refer to their difference as $\delta\mathcal{W}$.

Finally, let us study the sign of $\delta\mathcal{W}$. For simplicity of notation, we set $a = 1$, since here we are not interested in considering a specific scale length. The derivatives with respect to R and z of a generic decreasing density profile $\rho(m)$ are

$$\begin{cases} \dfrac{\partial \rho}{\partial R} = \dfrac{R}{m} \dfrac{d\rho}{dm} = -\dfrac{R}{m} \left| \dfrac{d\rho}{dm} \right|, \\ \\ \dfrac{\partial \rho}{\partial z} = \dfrac{z}{q^2 m} \dfrac{d\rho}{dm} = -\dfrac{z}{q^2 m} \left| \dfrac{d\rho}{dm} \right|, \end{cases} \tag{4.28}$$

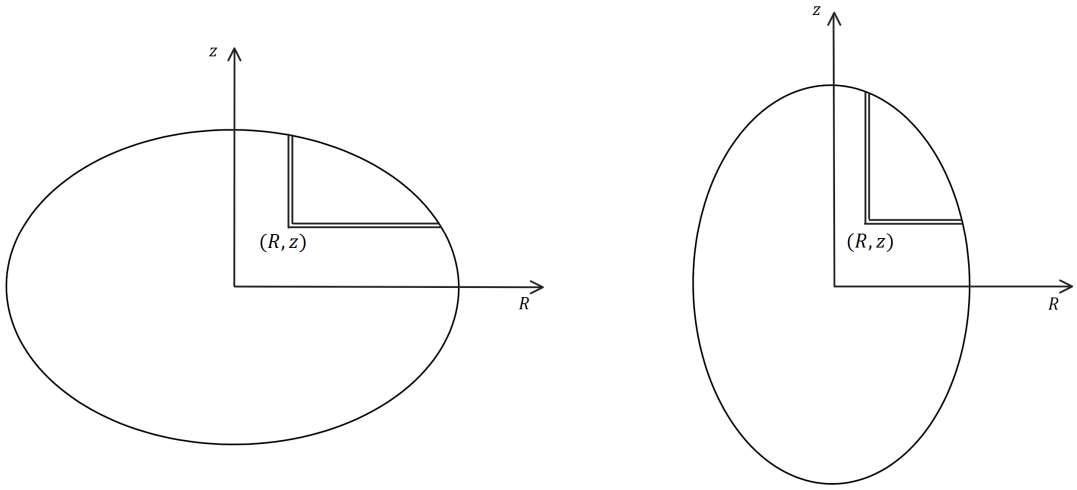

Figure 4.4. Illustration of the radial and vertical column at a generic point (R, z), for an oblate (left) and a prolate (right) ellipsoid.

and the derivatives of the potential are given in equation (4.4). Therefore, after some algebra, we can rewrite equation (4.27) as

$$\delta\mathcal{W} \equiv \int_R^{R_t} \rho \frac{\partial\Phi}{\partial R'} dR' - \int_z^{z_t} \rho \frac{\partial\Phi}{\partial z'} dz' = (1-q^2) \int_R^{R_t} \int_z^{z_t} \mathcal{F}(R', z') dz' dR' + (1-q^2) \int_R^{R_t} \mathcal{G}(R', z'_t) dR', \tag{4.29}$$

where

$$\mathcal{F}(R, z) \equiv \frac{2\pi G}{q} \frac{Rz}{m} \left| \frac{d\rho}{dm} \right| \int_0^\infty d\tau \frac{\rho_\tau \tau}{(1+\tau)(q^2+\tau)\sqrt{\Delta(\tau)}}. \tag{4.30}$$

and

$$\mathcal{G}(R, z) \equiv 2\pi G q R \rho(R, z) \int_0^\infty d\tau \frac{\rho_\tau \tau}{(1+\tau)(q^2+\tau)\sqrt{\Delta(\tau)}}, \tag{4.31}$$

Note that the functions $\mathcal{F}$ and $\mathcal{G}$ are nowhere negative. Therefore, the sign of $\delta\mathcal{W}$ is determined by the sign of $1 - q^2$.

For spatially untruncated ellipsoids, whose density is a decreasing function of m, so that $\rho = 0$ for $m \to \infty$, equation (4.29) simply becomes

$$\delta\mathcal{W} = (1-q^2) \int_R^\infty \int_z^\infty \mathcal{F}(R', z') dz' dR'. \tag{4.32}$$

We conclude that, at each point (R, z) of an axisymmetric ellipsoid (truncated or untruncated) with constant or decreasing density $\rho(m)$, $\delta\mathcal{W} \geq 0$ in oblate systems and $\delta\mathcal{W} \leq 0$ in prolate systems. In other words, at each point of oblate systems, the radial column is always heavier than the vertical one, while in prolate systems, the opposite occurs. Note that this result is obtained by considering only the density of the system and the corresponding gravitational field.

We now ask what are the conditions on dynamics that can compensate for this imbalance, allowing the system to be in equilibrium. We already showed that, in fluid ellipsoidal

systems, which have isotropic velocity dispersion, the balance can be reached only in the oblate case, thanks to rotation. However, stellar systems, at variance with normal fluids, can be characterised by quite complicated orbital structures. This part of the problem is described by the Jeans Equations (JEs), which are introduced in the next section.

4.2 The Jeans equations for axisymmetric two-integral systems

When studying the dynamics of galaxies, the comparison between theoretical models and observations primarily relies on the velocity moments of the DF, which contains all the information about the density distribution and the mean kinematics of the stars in the system (see Appendix A for a more extended explanation). Although velocity moments are straightforward to compute when the DF is known, the DF itself is generally not obtainable in practice. Therefore, alternative methods are needed to infer velocity moments from the macroscopic properties of the system. In this context, the JEs play a crucial role. They relate the velocity moments to the density and gravitational potential of the system. Specifically, in this thesis, we focus on stationary, axisymmetric, two-integral systems. Under these assumptions the JEs, in cylindrical coordinates, are (Binney and Tremaine 2008; Ciotti 2021)

$$\begin{cases} \dfrac{\partial \rho\sigma^2}{\partial z} = -\rho\dfrac{\partial \Phi}{\partial z}, \\ \\ \dfrac{\partial \rho\sigma^2}{\partial R} - \dfrac{\rho\Delta}{R} = -\rho\dfrac{\partial \Phi}{\partial R}, \quad \Delta \equiv \overline{v_\varphi^2} - \sigma^2. \end{cases} \tag{4.33}$$

Note that the system of equation (4.33) is closed[1], allowing us to determine the two unknowns $\overline{v_\varphi^2}$ and σ^2. The quantity $\overline{v_\varphi^2}$ can then be further decomposed into its dispersion (σ_φ^2) and ordered ($\overline{v_\varphi}^2$) components. This point will be addressed later, in Chapter 6.

4.2.1 Solving the Jeans equations

In the following, we outline the procedure to solve the JEs. The first equation in (4.33), gives

$$\rho\sigma^2 = \int_z^{z_t} \rho\frac{\partial \Phi}{\partial z'} dz', \tag{4.34}$$

where $\rho\sigma^2(R, z_t) = 0$ necessarily. By comparison with the equation of hydrodynamics, $\rho\sigma^2$ can be interpreted as a "pressure" exerted by stars. On the right-hand side, we note the expression for the "weight" $\mathcal{W}_z$ of the vertical column above each point (R, z). The term $\rho\sigma^2$ can then be substituted in the radial equation of (4.33) to find

$$\overline{v_\varphi^2} = R\frac{\partial \Phi}{\partial R} + \frac{R}{\rho}\frac{\partial \rho\sigma^2}{\partial R} + \sigma^2. \tag{4.35}$$

[1]For generic axisymmetric systems the JEs involve more unknowns than equations and require additional closure relations. The assumption of a two-integral DF is one of the simplest. It ensures $\sigma_R^2 = \sigma_z^2$ and that all mixed velocity moments $\overline{v_i v_j}$ vanish, thus providing the extra conditions needed to close the system.

This represents the most immediate way to solve the JEs. However, we now introduce another equivalent approach to find $\overline{v_\varphi^2}$, as it highlights some important properties of the solution and allows us to link the JEs to the argument of the two columns discussed in the previous section. Integrating the radial equation of (4.33) at fixed z, one finds

$$\rho\sigma^2 = \int_R^{R_t} \rho \frac{\partial \Phi}{\partial R'} dR' - \int_R^{R_t} \frac{\rho\Delta}{R'} dR'. \tag{4.36}$$

This shows that the same pressure exerted by stars in the z-direction to sustain the vertical column, is the one exerted in R-direction to sustain the effective weight of the radial column, which is $\mathcal{W}_R$ plus the additional term

$$-\int_R^{R_t} \frac{\rho\Delta}{R'} dR'. \tag{4.37}$$

This term must then correspond to the difference $-\delta\mathcal{W}$ between the two weights, thus by comparison with equation (4.27), we have

$$\frac{\rho\Delta}{R} = \int_z^{z_t} \left(\frac{\partial \rho}{\partial R}\frac{\partial \Phi}{\partial z'} - \frac{\partial \rho}{\partial z'}\frac{\partial \Phi}{\partial R} \right) dz' + \rho(R, z_t)\frac{d\Phi(R, z_t)}{dR}, \tag{4.38}$$

from which $\overline{v_\varphi^2}$ is recovered as $\overline{v_\varphi^2} = \Delta + \sigma^2$ (see also equation (13.103) in Ciotti 2021).

4.2.2 Sign of Δ and its role in the equilibrium of two-integral systems

We focus now on the sign of Δ and what it implies in the dynamics of stellar systems. Using the same procedure of Section 4.1.2, one finds

$$\frac{\rho\Delta}{R} = (1 - q^2) \left[\int_z^{z_t} \mathcal{F}(R, z')dz' + \mathcal{G}(R, z_t) \right], \tag{4.39}$$

with $\mathcal{F}$ and $\mathcal{G}$ given in equations (4.30) and (4.31). Therefore, the sign of Δ corresponds to the sign of $1 - q^2$ and we have immediately

Theorem 3.

$$\begin{aligned} &\textit{Oblate} && \Delta \geq 0, \\ &\textit{Spherical} && \Delta = 0, \\ &\textit{Prolate} && \Delta \leq 0, \end{aligned} \tag{4.40}$$

where in oblate and prolate systems $\Delta = 0$ is verified only on the z-axis. From the definition of Δ, this implies $\overline{v_\varphi^2} = \sigma^2$ on the z-axis in both oblate and prolate models and, everywhere else, $\overline{v_\varphi^2} < \sigma^2$ in prolate systems and $\overline{v_\varphi^2} > \sigma^2$ in oblate systems. Being $\overline{v_\varphi^2} = \sigma_\varphi^2 + \overline{v_\varphi}^2$ this means that prolate systems have $\sigma_\varphi^2 < \sigma^2$, except on the z-axis, where $\sigma_\varphi^2 = \sigma^2$. This, again, confirms that isotropic prolate systems do not exist. Conversely, in oblate systems, both $\sigma_\varphi^2 \leq \sigma^2$ and $\sigma_\varphi^2 \geq \sigma^2$ are possible depending on the value and decomposition of $\overline{v_\varphi^2}$, thus isotropy is a valid possibility for oblate ellipsoids. Isotropic oblate systems are

typically referred to as "isotropic rotators" and they have been observed and widely studied in the literature (e.g., Binney and Tremaine 2008; Cappellari 2016).

It should be noted that the sign of Δ as a function of the axial ratio q is not a new result in the literature (see e.g., Ex. 13.29 in Ciotti 2021). Similar results regarding the sign of Δ and the impossibility of constructing isotropic prolate systems have also been found, with a different method, in non-stratified ellipsoids, by Jiang and Moss (2002).

In this context, the contribution of this thesis is to provide a simple physical interpretation of *why* Δ must have this sign: it reflects the imbalance between the radial and vertical density columns at each point. In particular, if we look at equation (4.36) we see that, if $\Delta \geq 0$, the effective weight of the radial column is lower than $\mathcal{W}_R$, whereas if $\Delta \leq 0$, the effective weight is higher than $\mathcal{W}_R$. Since in prolate systems the vertical column is heavier than the radial one, additional support is required, and a negative Δ naturally plays this role. Conversely, in oblate systems, where the radial column is heavier, a positive Δ is required. In isotropic systems ($\sigma_R^2 = \sigma_z^2 = \sigma_\varphi^2$), we have $\Delta = \overline{v_\varphi^2} - \sigma_\varphi^2 = \overline{v_\varphi}^2$, and equation (4.36) becomes

$$\rho\sigma^2 = \int_R^{R_t} \rho \frac{\partial \Phi}{\partial R'} dR' - \int_R^{R_t} \rho \frac{\overline{v_\varphi}^2}{R'} dR', \tag{4.41}$$

which shows that, in these systems, the weight of the radial column can only be reduced by the centrifugal support given by rotation, analogously to what we discussed in the hydrodynamic case (Section 4.1.1).

In summary, Δ plays a fundamental role in the equilibrium of two-integral systems, acting as a "balancing" term of the effective radial weight. This explains why two-integral prolate systems with anisotropic velocity dispersions can be in equilibrium, whereas isotropic prolate systems cannot.

CHAPTER 5

Consistency of Two-Integral Prolate Systems

In the previous chapter we introduced the JEs, which now allow us to recover the velocity fields of our models and to compare the internal dynamics of conjugate systems. Such a comparison, however, is meaningful only if the models are physically consistent. A necessary (though not sufficient) condition for physical consistency is $\overline{v_\varphi^2} \geq 0$ everywhere. If this condition fails, the model is immediately unphysical. Therefore, in this chapter, we address the possibility of the average azimuthal squared velocity $\overline{v_\varphi^2}$ becoming negative. While this issue never occurs in oblate systems, it is common in the prolate case. As a result, particular care must be taken when constructing two-integral prolate models.

We focus our analysis on three representative density profiles: Gaussian, power-law, and deprojected Sérsic profile. In Section 5.1, we determine whether models characterized by these profiles can be physically viable and we identify, when possible, conditions on the model parameters that guarantee $\overline{v_\varphi^2} \geq 0$. In Section 5.2, for the Gaussian and power-law cases, we further provide a detailed characterisation of the unphysical regions, analysing their shape, location, and dependence on model parameters to gain deeper insight into the nature and extent of the inconsistency. Finally, in Section 5.3, we discuss the limitations of relying solely on the sign of $\overline{v_\varphi^2}$ as a consistency criterion and clarify its relation to the more fundamental requirement of a positive distribution function.

5.1 Sign of $\overline{v_\varphi^2}$ in prolate systems

By definition, as an average of squared velocities, $\overline{v_\varphi^2}$ must be positive. Therefore, if the integration of the JEs leads to a negative value, the model is not physically acceptable and must be discarded. The need to examine this issue arises naturally from some of the results obtained in the previous chapters. In Chapter 3, for example, we saw that, in two-integral systems, the ratio W_{RR}/W_{zz}, which depends only on q, can be written as

$$\frac{W_{RR}}{W_{zz}} = 1 + \frac{\int_{\mathbb{R}^3} \rho\overline{v_\varphi^2} d^3\mathbf{x}}{\int_{\mathbb{R}^3} \rho\sigma^2 d^3\mathbf{x}}. \tag{5.1}$$

The necessary condition $\overline{v_\varphi^2} \geq 0$ implies $W_{RR}/W_{zz} \geq 1$. However, the inverse is not guaranteed: having $W_{RR}/W_{zz} \geq 1$ does not ensure that $\overline{v_\varphi^2} \geq 0$ everywhere in the system. In fact, $\overline{v_\varphi^2}$ can still become negative in some regions of space while keeping $\int_{\mathbb{R}^3} \rho\overline{v_\varphi^2} d^3\mathbf{x} \geq 0$. In other words, for a given q, the ratio W_{RR}/W_{zz} is fixed, but the local values of σ^2 and $\overline{v_\varphi^2}$ are *not* fixed and depend on the adopted density profile.

Another indication that $\overline{v_\varphi^2}$ may become negative comes from the considerations in Chapter 4, where we saw that in prolate systems $\Delta \leq 0$ everywhere. Since $\overline{v_\varphi^2} = \Delta + \sigma^2$, one may ask whether, for some density profiles and axial ratios q, even after adding σ^2 to the negative Δ, $\overline{v_\varphi^2}$ remains negative.

Let us consider, for example, a two-integral, truncated constant-density ellipsoid. The values of Δ and σ^2 are given in equation (13.177) of Ciotti (2021). By summing these two expressions, one can easily see that, in the prolate case, there exist regions inside the truncation radius where $\overline{v_\varphi^2} < 0$, whereas in the oblate case $\overline{v_\varphi^2} \geq 0$ everywhere. Therefore, two-integral truncated prolate systems with constant density cannot exist. This simple example demonstrates that $\overline{v_\varphi^2}$ can indeed become negative in some systems, emphasising the importance of checking its sign to rule out inconsistencies.

In the following, we limit our treatment to untruncated systems, as this simplifies the calculations and provides a reasonable approximation for real galaxies. Nevertheless, one could extend the analysis to include truncated systems with non-constant density[1] to explore the role of the truncation radius in the consistency of these models.

We begin our analysis of the sign of $\overline{v_\varphi^2}$ by recovering a general expression for $\rho\overline{v_\varphi^2}$. Summing $\rho\sigma^2$ given in equation (4.34) with $\rho\Delta$ in (4.38) yields

$$\rho\overline{v_\varphi^2} = \rho\Delta + \rho\sigma^2 = \frac{2\pi G a^2}{q^2} \int_{z/a}^{\infty} \int_0^{\infty} \frac{\rho\rho_\tau \tilde{z}}{(1+\frac{\tilde{\tau}}{q^2})^{3/2}(1+\tilde{\tau})} \left[1 - \frac{\tilde{\tau}(q^2-1)\tilde{R}^2}{(1+\tilde{\tau})q^2 m} \frac{|\rho'|}{\rho}\right] d\tilde{z} d\tilde{\tau}, \tag{5.2}$$

where $\tilde{\tau} \equiv \tau/a^2$, $\tilde{R} \equiv R/a$, $\tilde{z} \equiv z/a$, $\rho_\tau \equiv \rho(m_\tau)$, with m_τ defined as in (4.2), and $\rho' = \frac{d\rho}{dm}$. We note immediately that, in the case of oblate ellipsoids ($q < 1$), as expected, $\overline{v_\varphi^2}$ is positive everywhere, independently of the axial ratio and of the adopted density profile. In prolate ellipsoids ($q > 1$), instead, while on the z-axis ($\tilde{R} = 0$) $\overline{v_\varphi^2}$ is positive, as one moves away from the z-axis, determining the sign of $\overline{v_\varphi^2}$ is not straightforward and it depends on the specific density profile. In the following, we analyse three particular density profiles: Gaussian profile, power-law profile and deprojected Sérsic profile.

[1] To this end, one possibility could be to consider Ferrers ellipsoids (see e.g., Ciotti 2021, Ferrers 1877).

5.1.1 Gaussian density profile

Let us consider a Gaussian density profile, defined as

$$\rho(m) = \rho_0 e^{-m^2}, \quad m^2 = \tilde{R}^2 + \frac{\tilde{z}^2}{q^2}, \quad q > 1, \tag{5.3}$$

where ρ_0 is an arbitrary normalisation constant.

Despite not being a representative density profile for galaxies its simple analytical form makes the Gaussian profile a useful starting point for simple calculations and some first-order considerations.
With this density profile, equation (5.2) becomes

$$\rho\overline{v_\varphi^2} = \frac{2\pi G a^2}{q^2} \int_{z/a}^{\infty} \int_0^{\infty} \frac{\rho\rho_\tau \tilde{z}}{(1+\frac{\tilde{\tau}}{q^2})^{3/2}(1+\tilde{\tau})} \left[1 - \frac{2\tilde{\tau}(q^2-1)\tilde{R}^2}{(1+\tilde{\tau})q^2}\right] d\tilde{z}d\tilde{\tau}, \tag{5.4}$$

which can be easily integrated over $\tilde{z}$, allowing us to write $\overline{v_\varphi^2}$ as a one-dimensional integral in $\tilde{\tau}$,

$$\overline{v_\varphi^2} = \pi G a^2 \int_0^{\infty} \rho_\tau \frac{(1+\tilde{\tau})q^2 - 2\tilde{\tau}(q^2-1)\tilde{R}^2}{(2q^2+\tilde{\tau})(1+\frac{\tilde{\tau}}{q^2})^{1/2}(1+\tilde{\tau})^2} d\tilde{\tau}. \tag{5.5}$$

This more compact expression for $\overline{v_\varphi^2}$ simplifies the study of its sign. It is straightforward to show that the integrand is positive when

$$\tilde{R}^2 \leq \frac{q^2}{2(q^2-1)} \frac{1+\tilde{\tau}}{\tilde{\tau}}, \tag{5.6}$$

and since $1 < (1+\tilde{\tau})/\tilde{\tau} < \infty$, if $\tilde{R}^2 \leq \frac{q^2}{2(q^2-1)}$, the integrand is positive for every value of $\tilde{\tau}$, which leads to $\overline{v_\varphi^2} \geq 0$. Conversely, where $\tilde{R}^2 > \frac{q^2}{2(q^2-1)}$ the integrand becomes negative for high enough values of $\tilde{\tau}$, opening the possibility that the integral itself may be negative. In other words, $\overline{v_\varphi^2}$ could be negative for some values of $\tilde{R}$ sufficiently large.

Let us prove now that for any given axial ratio $q > 1$, there always exists a value of $\tilde{R}$ where $\overline{v_\varphi^2}$ becomes negative. Since it is sufficient to find at least one point where this occurs, let us fix, for simplicity, $z = 0$. We saw that, in order for this hypothesis to be verified, the condition $\tilde{R}^2 > \frac{q^2}{2(q^2-1)}$ is necessary. Therefore, let us choose, for example, $\tilde{R} = \tilde{R}_0 = \frac{q}{\sqrt{q^2-1}}$. With these choices, equation (5.5) becomes

$$\overline{v_\varphi^2}\,(R_0,\ 0) = G\rho_0 a^2 \pi \int_0^{\infty} e^{-\frac{q^2}{(q^2-1)(1+\tilde{\tau})}} \frac{1-\tilde{\tau}q^2}{(2q^2+\tilde{\tau})(1+\frac{\tilde{\tau}}{q^2})^{1/2}(1+\tilde{\tau})^2} d\tilde{\tau}. \tag{5.7}$$

We can numerically evaluate this expression for any values of $q > 1$, but we limit the computation to $1 < q < 3$ since, as shown in Chapter 3, two-integral prolate systems with $q \gtrsim 2.59$ do not exist. The resulting values of $\overline{v_\varphi^2}$ are shown in Figure 5.1, where we see that $\overline{v_\varphi^2}(R_0, 0) < 0$. This proves our hypothesis. Consequently, two-integral prolate models with a Gaussian density profile are inconsistent.

The arbitrary choice of $\tilde{R} = \tilde{R}_0$ was particularly convenient for this proof. However, since $\tilde{R}_0$ tends to infinity as $q \to 1$, one may question whether the inconsistency, although

formally present, typically arises only at very large radii, where the stellar density is negligible and the galaxy is, in practice, no longer physically present. To address this point, in Figure 5.2 we present some examples of numerical integration of equation (5.5), on the equatorial plane, for different values of q. These examples show that smaller q enlarge the positive region. Nevertheless, even in almost spherical systems $\overline{v_\varphi^2} < 0$ at relatively small $\tilde{R}$.

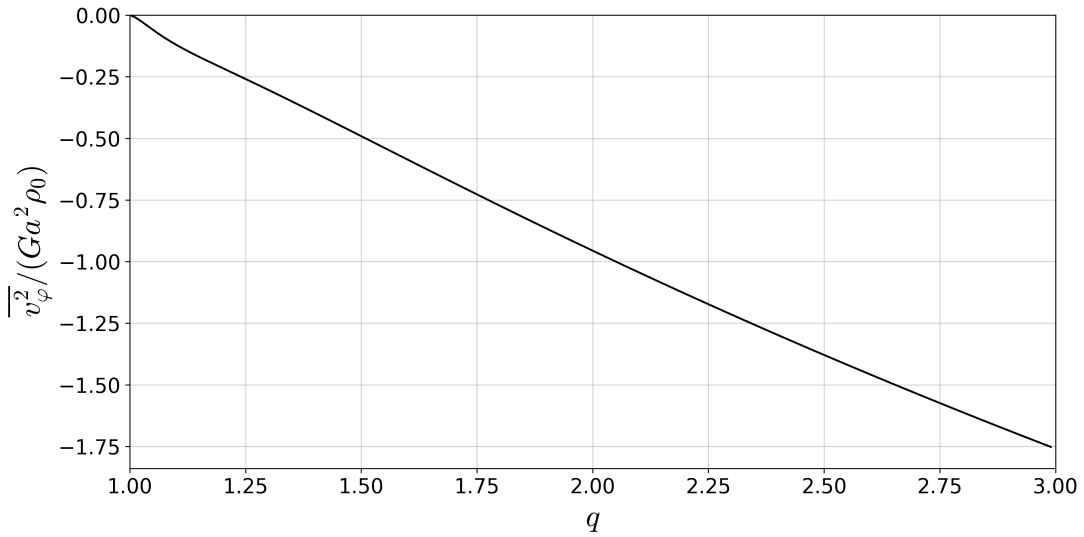

Figure 5.1. Values of $\overline{v_\varphi^2}$, in units of $Ga^2\rho_0$, on the equatorial plane ($z = 0$) for Gaussian, two-integral prolate systems, at $\tilde{R} = q/\sqrt{q^2-1}$. The values are obtained from numerical integration of equation (5.7), for $1 < q < 3$.

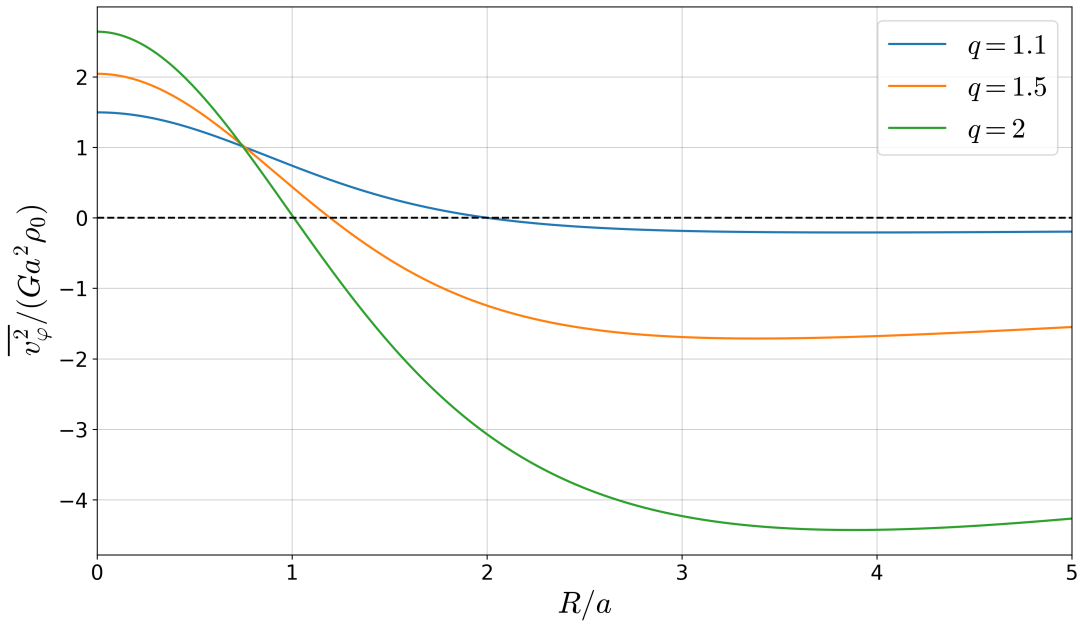

Figure 5.2. Values of $\overline{v_\varphi^2}$, in units of $Ga^2\rho_0$, on the equatorial plane ($z = 0$) for Gaussian, two-integral prolate systems. The values are obtained from numerical integration of equation (5.5), for three different axial ratios $q = 1.1, 1.5, 2$.

5.1.2 Power-law density profile

We now study the sign of $\overline{v_\varphi^2}$ in two-integral prolate systems, with a power-law density profile defined as

$$\rho(m) = \rho_0 m^{-\alpha}, \quad m^2 = \tilde{R}^2 + \frac{\tilde{z}^2}{q^2}, \quad \alpha > 0, \quad q > 1, \tag{5.8}$$

where ρ_0 is an arbitrary normalisation constant. This profile is particularly relevant when modelling galaxies, as several commonly adopted density profiles asymptotically behave like power-laws at large radii.

Substituting this density profile into equation (5.2), we obtain

$$\begin{aligned}\rho\overline{v_\varphi^2} &= \frac{2\pi G a^2}{q^2}\int_{z/a}^{\infty}\int_0^{\infty} \frac{\rho\rho_\tau \tilde{z}}{(1+\frac{\tilde{\tau}}{q^2})^{3/2}(1+\tilde{\tau})}\left[1 - \frac{\tilde{\tau}(q^2-1)\tilde{R}^2\alpha}{(1+\tilde{\tau})q^2m^2}\right] d\tilde{z}\, d\tilde{\tau} \\ &= \frac{2\pi G a^2}{q^2}\int_{z/a}^{\infty}\int_0^{\infty} \frac{\rho\rho_\tau \tilde{z}}{(1+\frac{\tilde{\tau}}{q^2})^{3/2}(1+\tilde{\tau})}\left[1 + \frac{(q^2-1)\tilde{R}^2\alpha}{(1+\tilde{\tau})q^2m^2} - \frac{(q^2-1)\tilde{R}^2\alpha}{q^2m^2}\right] d\tilde{z}\, d\tilde{\tau}.\end{aligned} \tag{5.9}$$

Since ρ is always non-negative, the sign of $\overline{v_\varphi^2}$ is determined by the sign of the double integral in $\tilde{z}$ and $\tilde{\tau}$. The potentially negative contribution arises from the term in parentheses:

$$\left[1 + \frac{(q^2-1)\tilde{R}^2\alpha}{(1+\tilde{\tau})q^2m^2} - \frac{(q^2-1)\tilde{R}^2\alpha}{q^2m^2}\right]. \tag{5.10}$$

In the limit $\tilde{\tau} \to \infty$, the second term, which contributes to making the parenthesis positive, vanishes, and the expression in (5.10) tends to

$$1 - \frac{(q^2-1)\tilde{R}^2\alpha}{q^2m^2}.$$

Therefore, a sufficient condition to ensure that the integral remains positive is

$$\frac{(q^2-1)\tilde{R}^2\alpha}{q^2m^2} \leq 1. \tag{5.11}$$

Since $\tilde{R}^2/m^2 \leq 1$, if $\alpha \leq 1$ the inequality (5.11) is satisfied for any axial ratio q. If, instead, $\alpha > 1$ it is satified if

$$q \leq \sqrt{\frac{\alpha}{\alpha-1}}. \tag{5.12}$$

This condition ensures that $\overline{v_\varphi^2} \geq 0$ everywhere in the system. If it is not fulfilled, the integrand in (5.9) becomes negative for some values of $\tilde{\tau}$. Nevertheless, the model may still have positive $\overline{v_\varphi^2}$ as long as the overall integral remains positive. In fact, condition (5.12) is only a *sufficient* condition for the positivity of $\overline{v_\varphi^2}$. However, we performed some numerical experiments and saw that this condition is very close to the *necessary* condition, even though we have not been able to determine it analytically. Therefore, condition (5.12)

provides a very good estimate of the maximum possible value of q for a given power-law density profile with slope α. Moreover, it suggests a noteworthy general trend: in two-integral prolate ellipsoids, the flatter the density profile, the more elongated the system can be.

5.1.3 Sérsic density profile

Finally, we analyse the sign of $\overline{v_\varphi^2}$ in two-integral prolate systems with a Sérsic surface brightness profile, widely regarded as the most accurate for early-type galaxies. It is defined, in the spherical case, as

$$I(R) = I_0 e^{-b\eta^{1/n}}, \quad \eta \equiv R/R_e, \tag{5.13}$$

where n is the Sérsic index, I_0 is the central surface brightness, R is the radius in the projection plane, R_e is the effective radius (i.e. the radius in the projection plane enclosing half of the total luminosity of the profile) and b is a dimensionless parameter depending on n. The brightness profile of many elliptical galaxies is well approximated by the Sérsic profile with $n = 4$ which is referred to as the de Vaucouleurs (1948) profile. However, more detailed studies have shown that ellipticals span a wide range of Sérsic indices (Caon et al. 1993; Graham and Guzmán 2003). Hence, in this section, we consider $2 \leq n \leq 6$.

The Sérsic law describes a projected quantity, but throughout this section we refer to its corresponding deprojected density profile, which can be recovered with various methods, both analytical and numerical and can be generalised to ellipsoidal systems (Ciotti, De Deo, et al. 2025; Ciotti 2021).

Beyond its observational relevance, the need to investigate this density profile arises from its asymptotic behaviour at large radii:

$$\rho(m) \sim \frac{e^{-bm^{1/n}}}{m^{1-1/2n}}, \quad m \to \infty. \tag{5.14}$$

In this regime, the density is expressed as a combination of an exponential term and a power-law term. As a result, it is not straightforward to determine whether two-integral prolate models with a Sérsic profile can be physically consistent. A dedicated analysis is therefore required to clarify this point.

Substituting (5.14) in equation (5.2), we obtain

$$\rho\overline{v_\varphi^2} = \frac{2\pi G a^2}{q^2} \int_{z/a}^{\infty} \int_0^{\infty} \frac{\rho\rho_\tau \tilde{z}}{(1+\frac{\tilde{\tau}}{q^2})^{3/2}(1+\tilde{\tau})} \left[1 - \frac{\tilde{\tau}(q^2-1)\tilde{R}^2}{(1+\tilde{\tau})q^2m^2}\left(1 - \frac{1}{2n} + \frac{b}{n}m^{1/n}\right)\right] d\tilde{z}d\tilde{\tau}, \tag{5.15}$$

We numerically integrate this equation for $n = 2$, 4, 6 and for different values of q, to gain insight into the typical behaviour of $\overline{v_\varphi^2}$ for different Sérsic indices and different axial ratios. Note that the potentially negative term

$$\left[1 - \frac{\tilde{\tau}(q^2-1)\tilde{R}^2}{(1+\tilde{\tau})q^2m^2}\left(1 - \frac{1}{2n} + \frac{b}{n}m^{1/n}\right)\right]$$

increases with increasing z, making the condition $\overline{v_\varphi^2} \geq 0$ easier to satisfy away from

the equatorial plane ($z = 0$). To ensure that our analysis is conservative and captures the most restrictive case, we perform the numerical integration at $z = 0$. An additional consideration concerns determining the value of the parameter b, which depends on n through the transcendental equation $\Gamma(2n) = \gamma(2n, b)$, where $\Gamma(x)$ and $\gamma(a, x)$ are the complete and lower incomplete gamma functions, respectively. Since b cannot be expressed in closed form, for our computations we adopt the asymptotic expansion of $b(n)$ derived by Ciotti and Bertin (1999), truncated at the third term:

$$b = 2n - \frac{1}{3} + \frac{4}{405n}. \tag{5.16}$$

The results of the numerical integration are shown in Figure 5.3. We find that, in all cases considered, $\overline{v_\varphi^2}$ always becomes negative beyond a sufficiently large value of $\tilde{R}$[2]. For a fixed value of the Sérsic index n, increasing the axial ratio q narrows the region with positive $\overline{v_\varphi^2}$. Conversely, for a fixed q, increasing n tends to enlarge the positive region. In the Gaussian case, we observed that $\overline{v_\varphi^2}$ turns negative already at relatively small $\tilde{R}$, even in nearly spherical systems. With Sérsic profiles, however, we note that the region where $\overline{v_\varphi^2} \geq 0$ can be significantly extended by choosing smaller values of q and higher values of n. For instance, in the case $n = 4$ and $q = 1.16$, $\overline{v_\varphi^2}$ becomes negative beyond $\tilde{R} \approx 44$, a region where the stellar density is essentially negligible. This is not surprising: the exponential decay in the Sérsic profile is shallower than in the Gaussian, and, as discussed in the previous section, a flatter density profile generally favours consistency. Therefore, unlike the Gaussian case, two-integral prolate galaxies with a Sérsic surface brightness distribution can be physically viable.

In particular, a reasonable approximation for the radius beyond which the stellar density of galaxies becomes negligible is $\approx 10R_e$. In the context of elliptical galaxies, R_e corresponds to the scale length a, hence, on the equatorial plane, $10R_e$ correspond to $\tilde{R} = 10$. Therefore, we determine, for different values of the Sérsic index n, the maximum value q_{10} of the axial ratio for which $\overline{v_\varphi^2}$ remains positive within $\tilde{R} = 10$. The approximate values of q_{10}, obtained numerically from equation (5.15), for $n = 2, 3, 4, 5, 6$, are presented in Table 5.1, where we observe that models with higher Sérsic indices (characterised by a shallower density slope in the outer regions) can be more elongated. This, again, is in agreement with the conclusion that flatter density profiles allow for more elongated systems.

$\boldsymbol{n}$	2	3	4	5	6
$\boldsymbol{q_{10}}$	1.11	1.17	1.21	1.25	1.27

Table 5.1: Maximum axial ratio q_{10} for which a two-integral prolate system with Sérsic index $n = 2, 3, 4, 5, 6$ satisfies $\overline{v_\varphi^2} \geq 0$ on the equatorial plane ($z = 0$) within $10R_e$ which correspond to $\tilde{R} = 10$.

[2]The plots are obtained considering only the asymptotic behaviour of ρ for large m, as this simplifies the computations and since the previous density profiles considered suggest that consistency problems arise at large radii. However, some numerical experiments with the complete deprojected Sérsic profile given in Ciotti, De Deo, et al. (2025) have been performed, and the positivity of $\overline{v_\varphi^2}$ in the central regions has been checked.

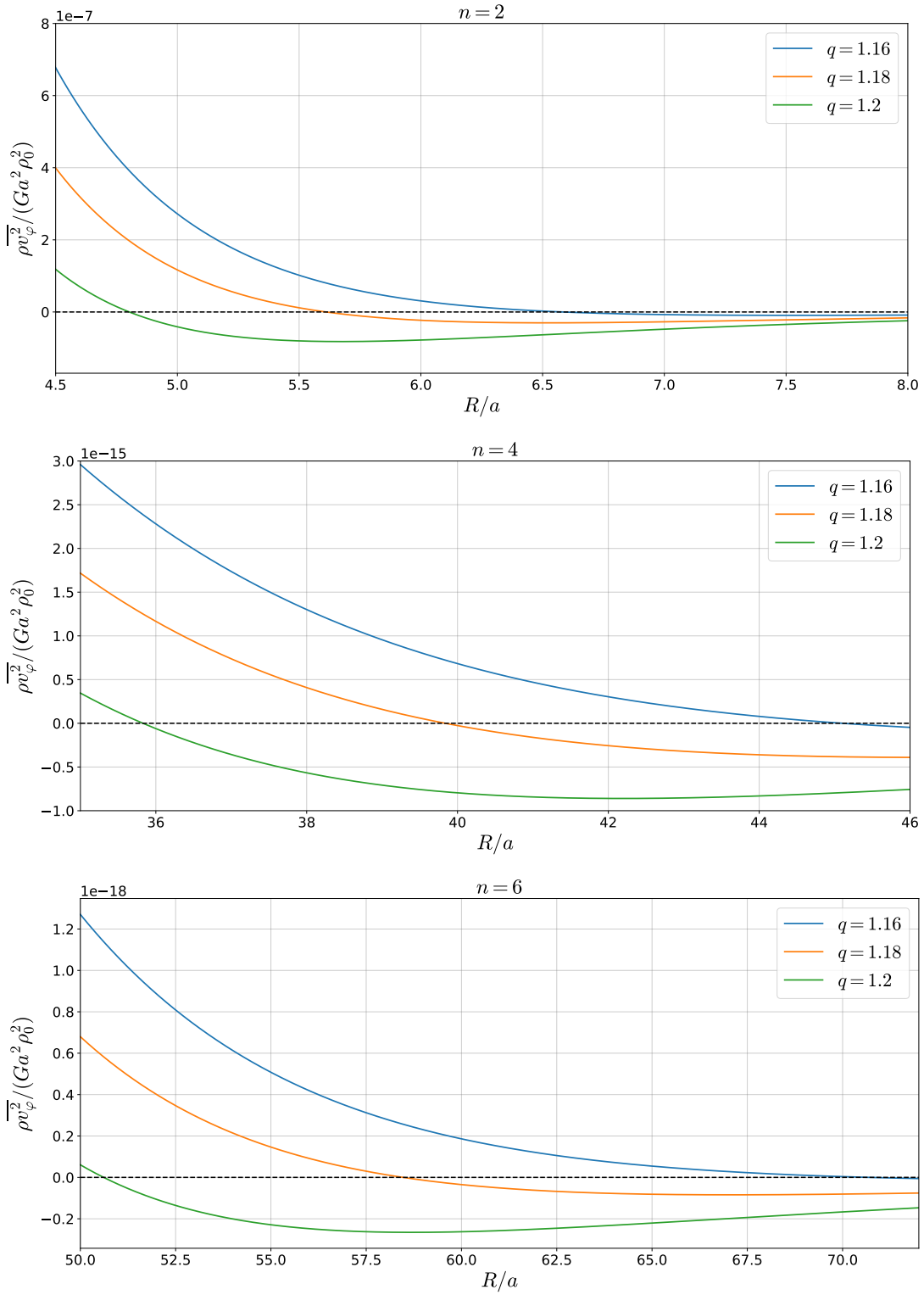

Figure 5.3. Values of $\rho\overline{v_\varphi^2}$ in units of $Ga^2\rho_0^2$, on the equatorial plane ($z = 0$), in two-integral prolate systems with Sérsic profile with index $n = 2$ (top), $n = 4$ (middle), $n = 6$ (bottom). The three curves refer to three values of the axial ratio $q = 1.16, 1.18, 1.2$.

5.2 Regions with $\overline{v_\varphi^2} < 0$ in prolate systems

Having established that two-integral prolate models can have regions where $\overline{v_\varphi^2}$ becomes negative, we now turn to a more detailed characterisation of these inconsistent regions, determining their shape and location for different model parameters to better understand the nature and extent of the inconsistency.

To carry out this analysis we write again $\rho\overline{v_\varphi^2}$ as the sum of $\rho\Delta$ and $\rho\sigma^2$, but this time we adopt the simplifying assumption of a spherical potential, i.e., $\Phi = \Phi(r)$, where $r = \sqrt{\tilde{R}^2 + \tilde{z}^2}$. This approximation is motivated by the fact that the gravitational potential is in general rounder than the underlying density distribution and, as discussed, inconsistency arises already in almost spherical systems. This assumption is particularly useful, as it allows us to eliminate the integral over τ. To simplify the notation, in what follows we work entirely in dimensionless variables: $\tilde{R} \to R$, $\tilde{z} \to z$, so that $r = \sqrt{R^2 + z^2}$ and $m^2 = R^2 + z^2/q^2$.

From equation (4.38), we thus have

$$\begin{aligned} \rho\Delta &= R\int_z^\infty \left(\frac{\rho' R}{m}\frac{\Phi'\hat{z}}{r} - \frac{\rho'\hat{z}}{q^2 m}\frac{\Phi' R}{r}\right) d\hat{z} \\ &= R\left(1 - \frac{1}{q^2}\right)\int_z^\infty \frac{\rho'\Phi' R\hat{z}}{mr} d\hat{z}, \end{aligned} \tag{5.17}$$

where $\rho' \equiv \frac{\partial\rho}{\partial m}$ and $\Phi' \equiv \frac{\partial\Phi}{\partial r}$. From equation (4.34),

$$\rho\sigma^2 = \int_z^\infty \frac{\rho\Phi'\hat{z}}{r} d\hat{z}. \tag{5.18}$$

Hence we obtain

$$\rho\overline{v_\varphi^2} = \int_z^\infty \frac{\Phi'\hat{z}}{r}\left[\rho + \frac{\rho' R^2}{m}\left(1 - \frac{1}{q^2}\right)\right] d\hat{z}. \tag{5.19}$$

Using this equation, we now study separately the Gaussian profile and the power-law density profiles.

5.2.1 Gaussian density profile

Let us substitute into equation (5.19)

$$\rho = \rho_0 e^{-m^2}, \quad \Phi = -\frac{\Phi_0}{r}, \tag{5.20}$$

where ρ_0 and Φ_0 are arbitrary normalisation constants. We obtain

$$\rho\overline{v_\varphi^2} = \rho_0\Phi_0\left[1 - \frac{2(q^2-1)R^2}{q^2}\right] e^{-R^2}\int_z^\infty \frac{\hat{z}}{r^3} e^{-\frac{\hat{z}^2}{q^2}} d\hat{z}. \tag{5.21}$$

As already discussed in Section 5.1.1, for any value of $q > 1$ there exist a region where $\overline{v_\varphi^2} < 0$. This becomes evident under the assumption of spherical potential. Moreover, this simple calculation shows that the extent of the inconsistent region depends only on the

cylindrical radius R. In particular, the following condition holds:

$$\overline{v_\varphi^2} < 0 \quad \text{where } R > \sqrt{\frac{q^2}{2(q^2-1)}} \tag{5.22}$$

This represents a simple estimate of the boundary beyond which Gaussian models have $\overline{v_\varphi^2} < 0$. In Figure 5.4 we provide a visual representation of the positive region (in green) and negative region (in red) and how they vary with different q.

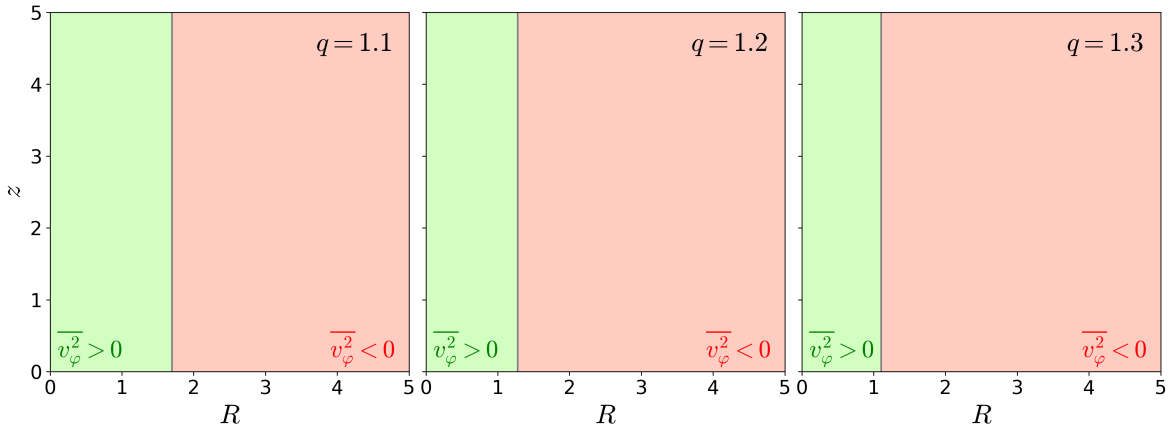

Figure 5.4. Regions in the (R, z)-plane where $\overline{v_\varphi^2} > 0$ (green) and $\overline{v_\varphi^2} < 0$ (red), for a Gaussian density profile, with three different values of the axial ratio $q = 1.1, 1.2, 1.3$. R and z are normalised to the scale length a.

5.2.2 Power-law density profile

For the power-law density profile, we substitute into equation (5.19)

$$\rho = \rho_0 m^{-\alpha}, \quad \Phi = -\frac{\Phi_0}{r}, \tag{5.23}$$

which gives

$$\begin{aligned} \rho\overline{v_\varphi^2} &= \rho_0\Phi_0 \int_z^\infty \frac{\hat{z}}{r^3}\left[\frac{1}{m^\alpha} - \frac{\alpha R^2}{m^{\alpha+2}}\left(1-\frac{1}{q^2}\right)\right] d\hat{z} \\ &= \rho_0\Phi_0 \frac{1}{R^{1+\alpha}} \int_s^\infty \frac{t}{(1+t^2)^{3/2}(1+t^2/q^2)^{\alpha/2}}\left(1 - \frac{\alpha(1-1/q^2)}{1+t^2/q^2}\right) dt, \end{aligned} \tag{5.24}$$

where we defined $t \equiv \hat{z}/R$ and $s \equiv z/R$. As expected, if the condition (5.12) is satisfied, $\overline{v_\varphi^2} \geq 0$. If this condition is not satisfied, the integrand is negative for small values of t and becomes positive for sufficiently large t. Therefore there exist s_0 high enough so that $\overline{v_\varphi^2} \geq 0$ for $s > s_0$. This means that the positive region is inside a conical surface defined by the equation $z^2 = s_0 R^2$.

Figure 5.5 shows some examples of the shape of the positive and negative regions[3],

[3]The value of s_0 corresponding to the boundary between consistent and inconsistent region is computed from (5.24) by numerically solving the equation $\rho\overline{v_\varphi^2} = 0$, using the `Python` routines `scipy.integrate.quad` for the integral and `scipy.optimize.root_scalar` for the root finding.

for different values of α and q. We note that, for a given q, s_0 increases as α increases, narrowing the positive conical region. The same trend is obtained increasing q for a fixed value of α.

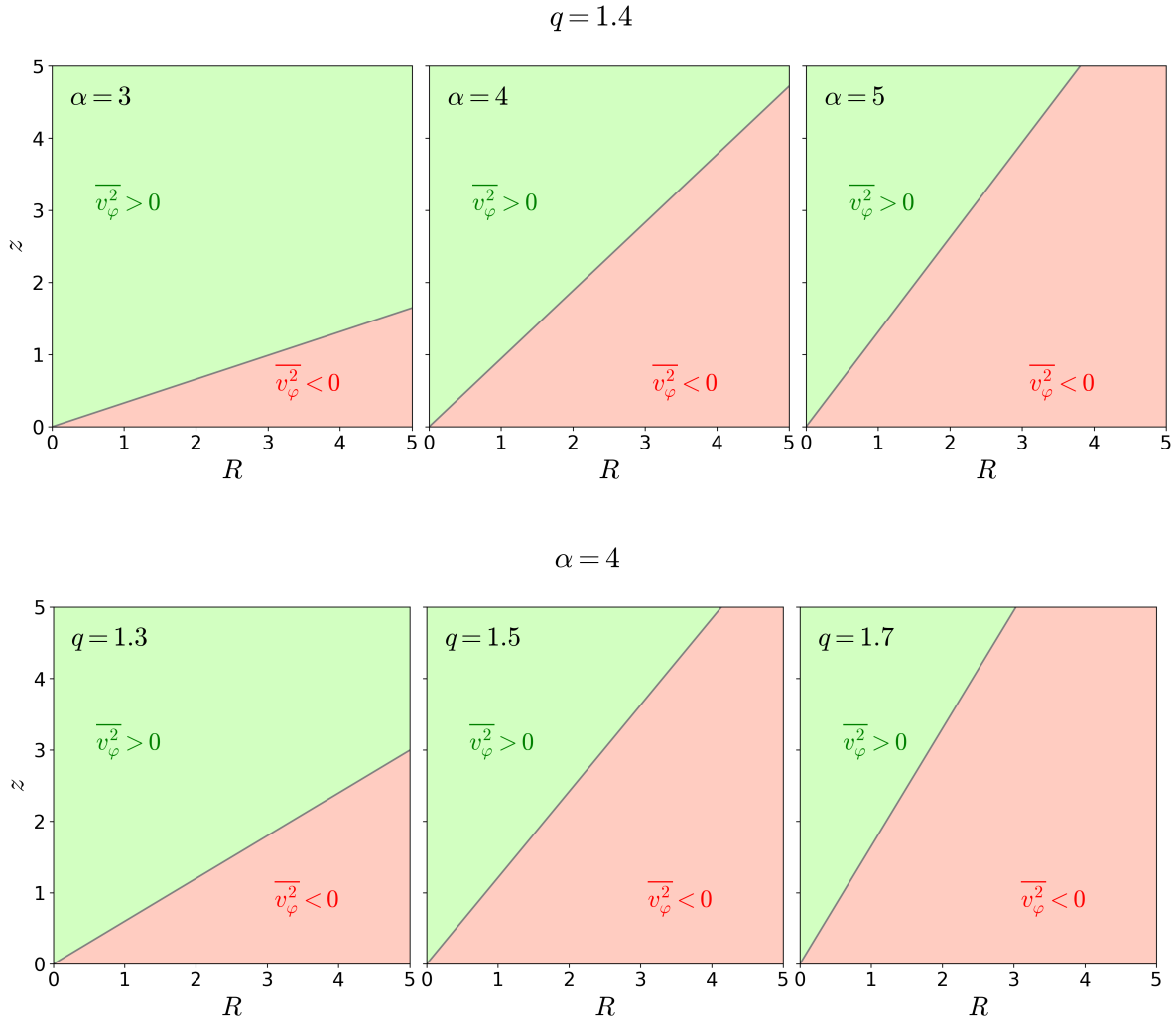

Figure 5.5. Regions in the (R, z)-plane where $\overline{v_\varphi^2} > 0$ (green) and $\overline{v_\varphi^2} < 0$ (red) in two-integral prolate models with a power-law density profile. R and z are normalised to the scale length a. Top panel: the axial ratio $q = 1.4$ is fixed and the power-law exponent is, from left to right, $\alpha = 3, 4, 5$. Bottom panel: the power-law exponent $\alpha = 4$ is fixed and the axial ratio is, from left to right, $q = 1.3, 1.4, 1.5$.

5.3 Consistency and distribution function

We conclude this chapter with an important remark. So far, we have focused on the condition $\overline{v_\varphi^2} \geq 0$. However, satisfying this condition does *not* necessarily imply that the model is physically consistent. In the context of stellar dynamics, the term "consistency" refers specifically to the positivity of the distribution function (DF) f everywhere in phase space. By definition, $\overline{v_\varphi^2}$ is the average of the squared azimuthal velocity over the velocity space, weighted by the DF (see Appendix A). Therefore, if $\overline{v_\varphi^2} < 0$, f is necessarily negative in some regions of phase space, and the model is inconsistent. On the other hand, if

$f \geq 0$ everywhere in phase space, then, necessarily $\overline{v_\varphi^2} \geq 0$. However, the inverse is not true: $\overline{v_\varphi^2}$ could be positive even if $f < 0$ in some regions of phase space. To summarise the requirements for consistency, including also the constraint derived in Chapter 3, we schematically illustrate them as follows.

$$f \geq 0 \quad \not\Longrightarrow \quad \overline{v_\varphi^2} \geq 0 \quad \not\Longrightarrow \quad \frac{W_{RR}}{W_{zz}} \geq 1$$

$$\frac{W_{RR}}{W_{zz}} < 1 \quad \not\Longrightarrow \quad \overline{v_\varphi^2} < 0 \quad \not\Longrightarrow \quad f < 0$$

To address the consistency of our models, we should, in principle, derive the corresponding DF and check its sign. For two-integral systems, i.e., $f = f(E, L_z)$, there exist some techniques to recover the DF once the density profile is chosen and, for completeness, we list some of them below. However, recovering the DF of our models is beyond the scope of this thesis and we will not discuss it further.

In axisymmetric systems where the density can be expressed as $\rho(R, \Phi)$, some inversion methods can be applied. These techniques require the analytic continuation of ρ in the complex plane and include:

1. methods based on *integral transforms*, such as the Lynden-Bell (1962) method, the Hunter (1975) method and the Dejonghe (1986) method;

2. the method proposed by Hunter and Qian (1993) based on the *theorem of residues* for functions of complex variables.

The latter was used, for example, to derive the DF in elliptically stratified power-law models, by Qian et al. (1995). In Figure 5.6, we report one of their figures, which illustrates, for each power-law exponent α (which corresponds to $-\alpha$ of this thesis) the values of the axial ratio q allowed for a positive DF. We note that oblate systems have a positive DF for any q. Conversely, in prolate systems, the maximum axial ratio for a positive DF decreases for steeper density profiles. Similar results were found by Evans (1994).

In general, even though we will not derive the DF of our models, one could reasonably expect that, when $\overline{v_\varphi^2}$ starts becoming negative in some region, the DF is already negative in a substantial portion of phase space. Consequently, the conditions for consistency could be much more stringent than those derived for the positivity of $\overline{v_\varphi^2}$, which already limit prolate models to be almost spherical.

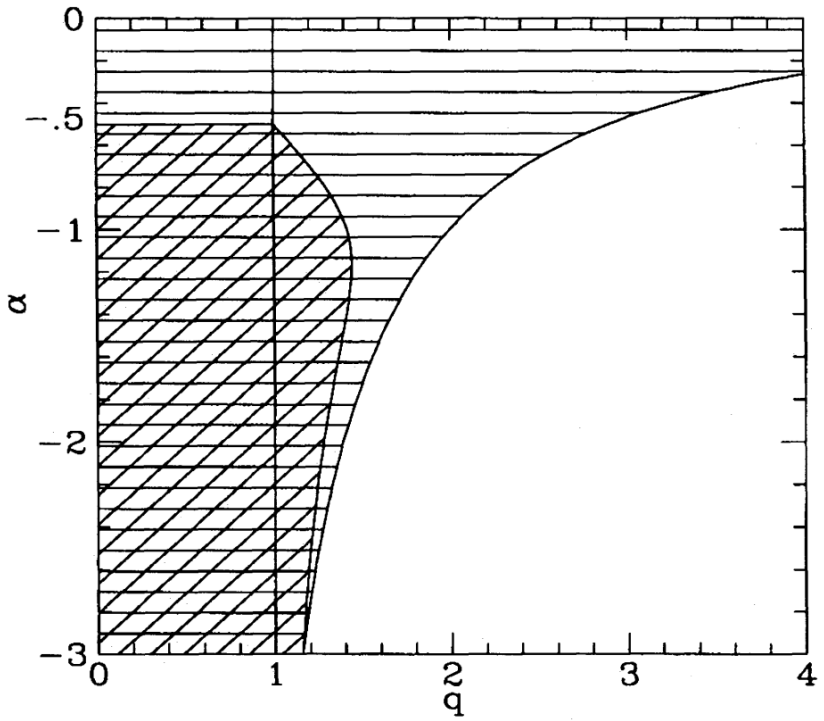

Figure 5.6. Figure reported from Qian et al. (1995), illustrating, with the horizontally hatched area, the region in the (q, α) parameter space where two-integral power-law ellipsoidal systems are consistent (i.e., they have non-negative distribution function everywhere in phase space). The diagonally hatched area indicates the region corresponding to model consistency in the presence of a central black hole (not discussed in this thesis).

CHAPTER 6

Intrinsic and Projected Kinematical Fields in Conjugate Systems

Building upon the general results found in the previous chapters, we now turn to the comparison of the internal dynamics of conjugate systems. In Section 6.1, we compute their intrinsic kinematical fields, i.e., σ^2 and $\overline{v_\varphi^2}$, by numerically solving the JEs, and we analyse the differences between oblate and prolate models. In Section 6.2, we then derive their projected kinematical fields, which are more directly linked to observations. We first recall the edge-on projection equations for the line-of-sight rotational velocity $v_{\rm los}$ and the line-of-sight velocity dispersion $\sigma_{\rm los}$ in axisymmetric systems. Solving these equations requires choosing a decomposition of $\overline{v_\varphi^2}$ into its dispersion (σ_φ^2) and ordered ($\overline{v_\varphi}^2$) components. Since the often used Satoh (1980) k-decomposition cannot be used for prolate systems, in Section 6.2.2, we introduce the λ-decomposition, valid for both oblate and prolate models. Finally we discuss the analogies and differences between oblate and prolate conjugate systems, both in the non-rotating and rotating case.

6.1 Intrinsic kinematical fields

In the previous chapters, we explored global differences between oblate and prolate systems. These differences are independent of the specific scale-length considered. Therefore, they are still present in conjugate oblate-prolate pairs. With this in mind, we now compute σ^2 and $\overline{v_\varphi^2}$ in conjugate systems, with the aim of identifying possible distinct kinematical trends between oblate and prolate models. As an illustrative case, we adopt the widely used Hernquist (1990) profile in its ellipsoidal form

$$\rho(m) = \frac{M}{2\pi a^3 q} \frac{1}{m(1+m)^3}, \tag{6.1}$$

as it is sufficiently simple to treat analytically and it reproduces quite well the density profile of elliptical galaxies. As additional illustrative examples, the intrinsic fields obtained for the Jaffe (1983) and Gaussian density profiles are presented in Appendix D.

6.1.1 Numerical integration of the Jeans equations

The numerical integration of the JEs is carried out by using a specifically developed code in the `Mathematica`[1] software. The code takes the density ρ as input and then computes its derivatives analytically as in equation (4.28). The velocity dispersion σ^2 and the azimuthal velocity squared $\overline{v_\varphi^2}$ are then obtained by solving equations (4.34) and (4.38), respectively, through the `NIntegrate` numerical routine. Finally, contour plots are generated using the function `ContourPlot`, with the default option `PlotPoints = 15`, which corresponds to an initial grid of 15 sample points per direction. The software then automatically refines this grid adaptively to provide a sufficiently fine sampling to describe the variations across the (R, z)-plane. For symmetry reasons we restrict the computation to the first quadrant of the (R, z)-plane.

6.1.2 Results

We consider conjugate models with an axial ratio chosen to ensure that the prolate system satisfies $\overline{v_\varphi^2} \geq 0$ everywhere. From condition (5.12), noting that the maximum slope of the Hernquist profile is $\rho \propto m^{-4}$ as $m \to \infty$, the limiting axial ratio that ensures the positivity of $\overline{v_\varphi^2}$ in the prolate system is $q_p = 2/\sqrt{3}$, which corresponds to $q_o = \sqrt{3}/2 \approx 0.866$. The resulting σ^2 and $\overline{v_\varphi^2}$ for the oblate and prolate models are shown in Figure 6.1 and a zoom on the central region is shown in Figure 6.2.

We find that the two quantities have comparable values in both systems, although σ^2 is globally higher in the prolate model, whereas $\overline{v_\varphi^2}$ is globally higher in the oblate model. Both σ^2 and $\overline{v_\varphi^2}$ vanish at the centre, a well-known property of density profiles with asymptotic behaviour $\rho \propto r^{-1}$ at small radii, such as the Hernquist profile (e.g., Appendix C in Bertin et al. 2002). Moreover, in the oblate case, contours of equal value of σ^2 are elongated along the z-axis, while in the prolate case, they are elongated along the R-axis. The opposite occurs for $\overline{v_\varphi^2}$. However, since the two models are compared with the same projected orientation, the oblate z-axis is oriented as the prolate R-axis. As a

[1] Wolfram Research, Inc., Mathematica, Version 14.1, Champaign, IL (2024)

result, no qualitative difference between the two systems is observed in the way σ^2 and $\overline{v_\varphi^2}$ are spatially distributed.

Although the results in Chapter 5 restrict physically possible prolate models to nearly spherical shapes, we plot σ^2 and $\overline{v_\varphi^2}$ for another pair of conjugate models with $q_p = 2$ i.e., $q_o = 1/2$, to illustrate the general trend for increasing flattening/elongation. Compared to the previous case, the difference between the oblate and the prolate model increases, with the maximum value of σ^2 in the prolate system being approximately double the one in the oblate system. As far as $\overline{v_\varphi^2}$ is concerned, as expected, the prolate system develops an inconsistent region whose shape closely resembles the analytical prediction for power-law profiles in Section 5.1.2. The small deviation from the analytical prediction is simply due to the fact that the Hernquist profile is not a pure power-law.

In addition to these results, we can exploit the numerical code to better understand and visualise the properties of axisymmetric systems discussed Chapter 4. We begin by computing the "pressures" $\rho\sigma^2$ and $\rho\overline{v_\varphi^2}$, shown in Figure 6.4. We find that both $\rho\sigma^2$ and $\rho\overline{v_\varphi^2}$ are almost perfectly stratified on the density profile. The small deviations from isodensity contours explain why, when we divide by the density, the contours of equal value of σ^2 and $\overline{v_\varphi^2}$ elongate along z or R. Additionally, we recall that $\rho\sigma^2$ can be interpreted both as the pressure exerted in the R- and z-directions, and as the weight of the vertical density column above each point. This figure thus allows us to visualise how the weight of the vertical density column varies across the (R, z)-plane. We then compute the weight difference $\delta\mathcal{W}$ between the radial and vertical density columns at each point. We already know that this difference is positive in oblate systems and negative in prolate ones, hence we plot its absolute value in Figure 6.5. We observe that $\delta\mathcal{W}$ is *not* constant, but decreases at larger distance from the centre of the system. Moreover, it is approximately stratified on the density and its absolute value is very similar in the conjugate oblate and prolate systems. In Figure 6.5 the absolute value of Δ is also showed. We observe that its maximum value in the prolate system is higher than its maximum value in the oblate system. Moreover, the maxima are located along the R-direction in both oblate and prolate systems. A simple explanation for this fact is that, as we showed in Chapter 4,

$$\delta\mathcal{W} = \int_R^\infty \frac{\rho\Delta}{R'} dR', \tag{6.2}$$

thus

$$\frac{\rho\Delta}{R} = -\frac{\partial\delta\mathcal{W}}{\partial R}. \tag{6.3}$$

Since $\delta\mathcal{W}$ is approximately stratified on the density, its radial variation is maximum on the equatorial plane ($z = 0$).

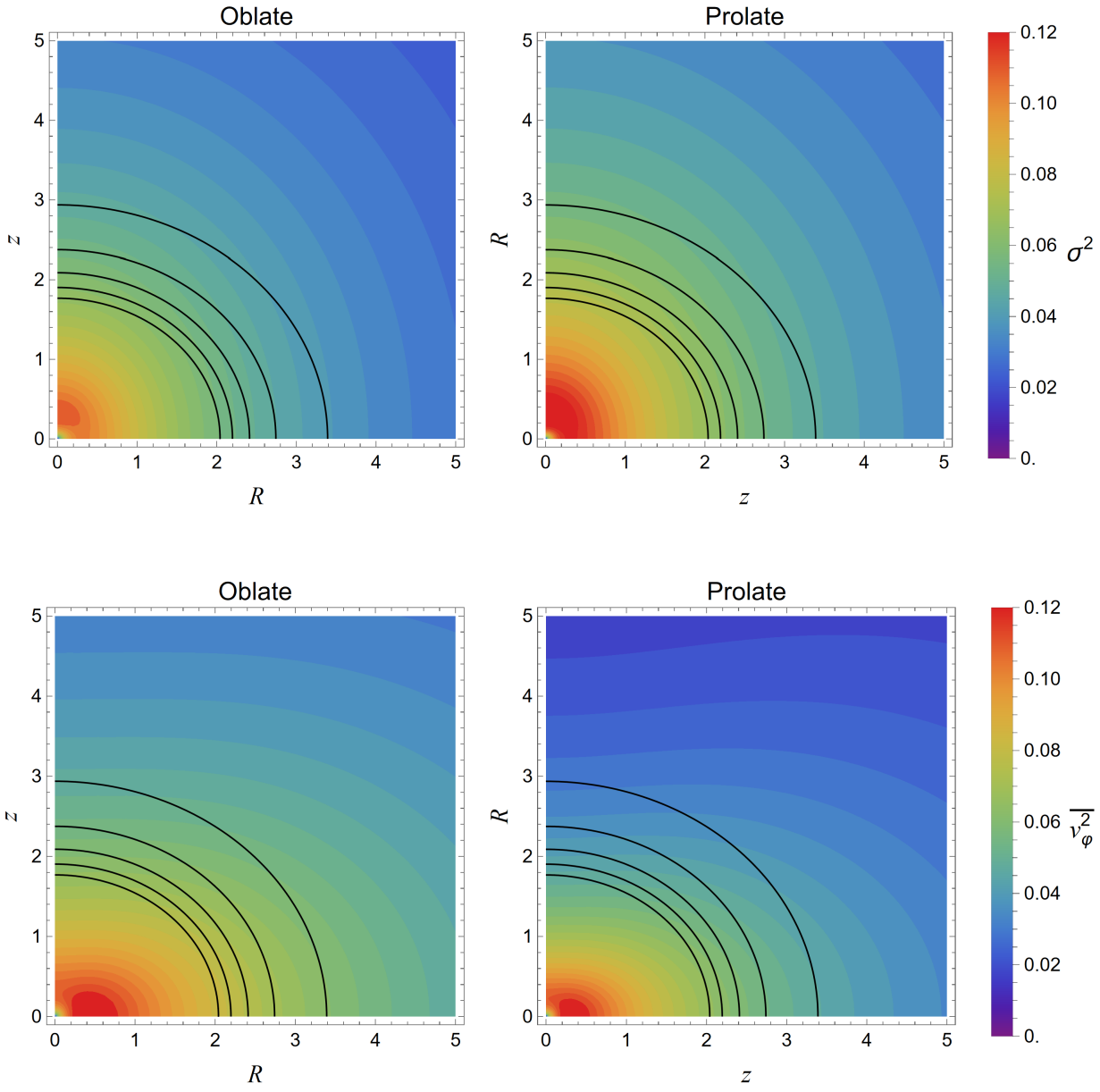

Figure 6.1. Maps in the (R,z)-plane of σ^2 (upper panels) and $\overline{v_\varphi^2}$ (lower panels) for oblate (left panels) and prolate (right panels) conjugate Hernquist models with axial ratio of the oblate system $q_o = \sqrt{3}/2$, in common units of GM/a_o. R and z are in units of the oblate scale length a_o, and z denotes the symmetry axis. Black solid lines represent isodensity contours of the stellar distribution. The colour scale is the same for σ^2 and $\overline{v_\varphi^2}$.

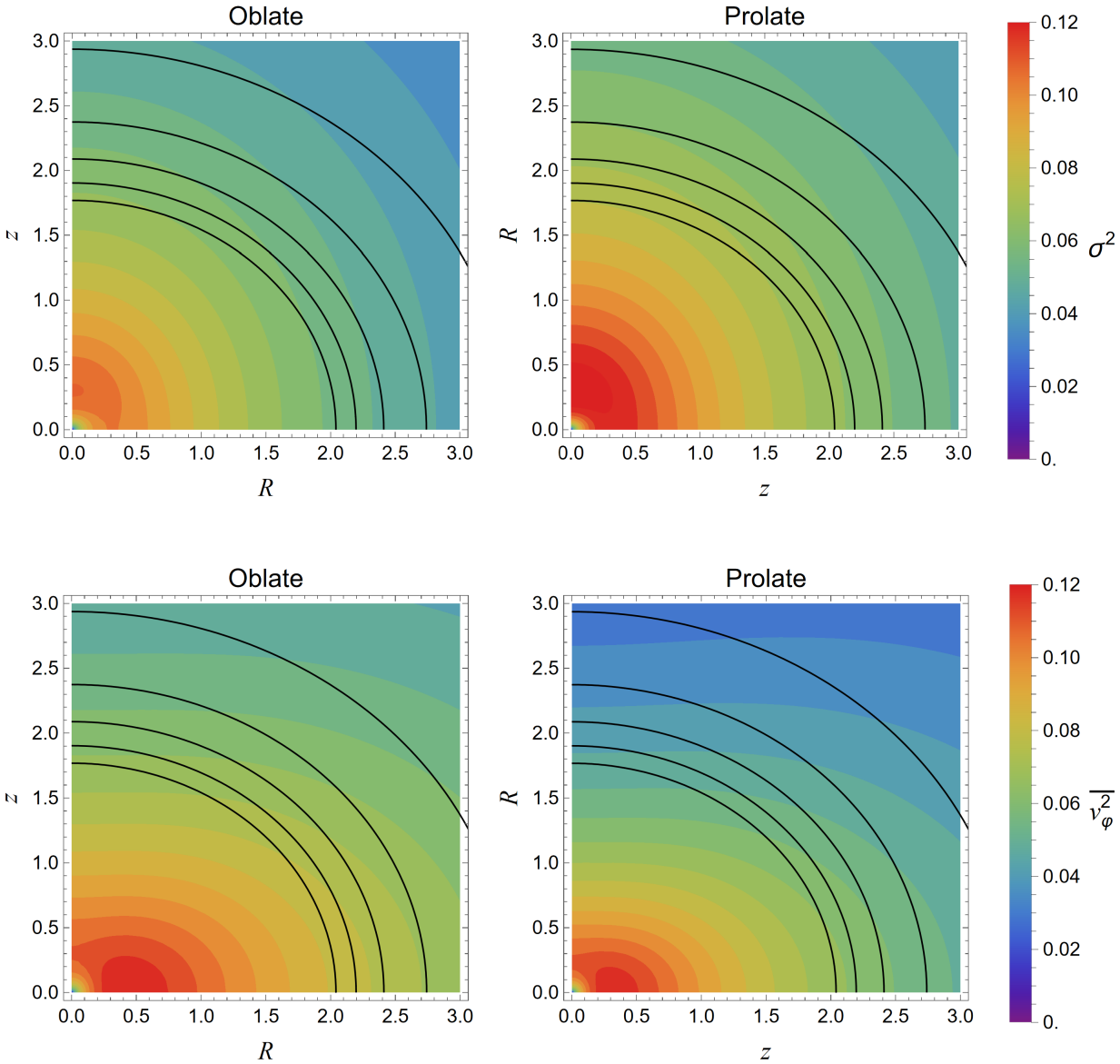

Figure 6.2. Zoomed maps in the (R,z)-plane of σ^2 (upper panels) and $\overline{v_\varphi^2}$ (lower panels) for oblate (left panels) and prolate (right panels) conjugate Hernquist models with axial ratio of the oblate system $q_o = \sqrt{3}/2$, in common units of GM/a_o. R and z are in units of the oblate scale length a_o, and z denotes the symmetry axis. Black solid lines represent isodensity contours of the stellar distribution. The colour scale is the same for σ^2 and $\overline{v_\varphi^2}$.

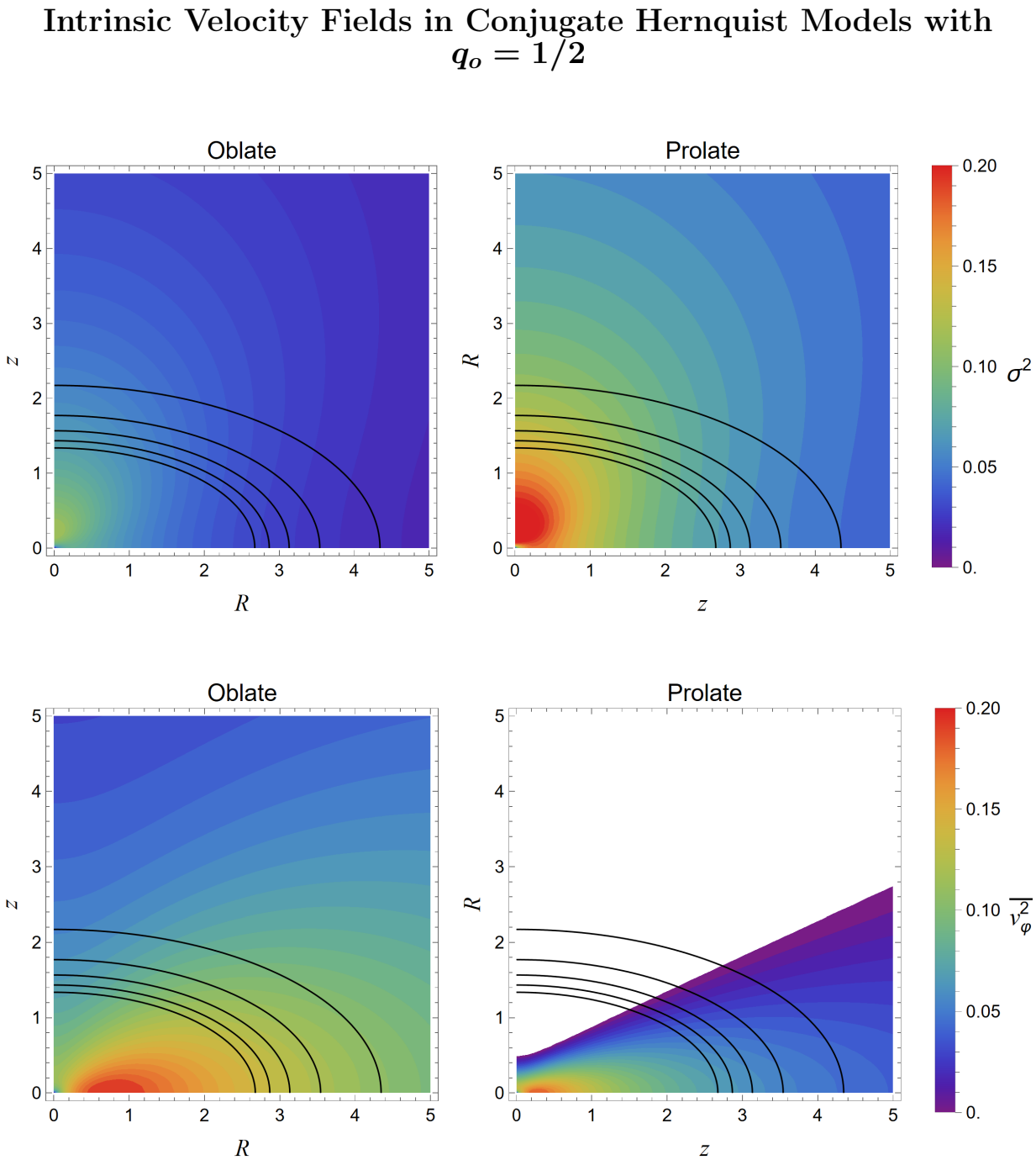

Figure 6.3. Maps in the (R,z)-planeof σ^2 (upper panels) and $\overline{v_\varphi^2}$ (lower panels) for oblate (left panels) and prolate (right panels) conjugate Hernquist models with axial ratio of the oblate system $q_o = 1/2$, in common units of GM/a_o. R and z are in units of the oblate scale length a_o, and z denotes the symmetry axis. Black solid lines show isodensity contours of the stellar distribution. The white region in the bottom right panel corresponds to negative values of $\overline{v_\varphi^2}$. The colour scale is the same for σ^2 and $\overline{v_\varphi^2}$.

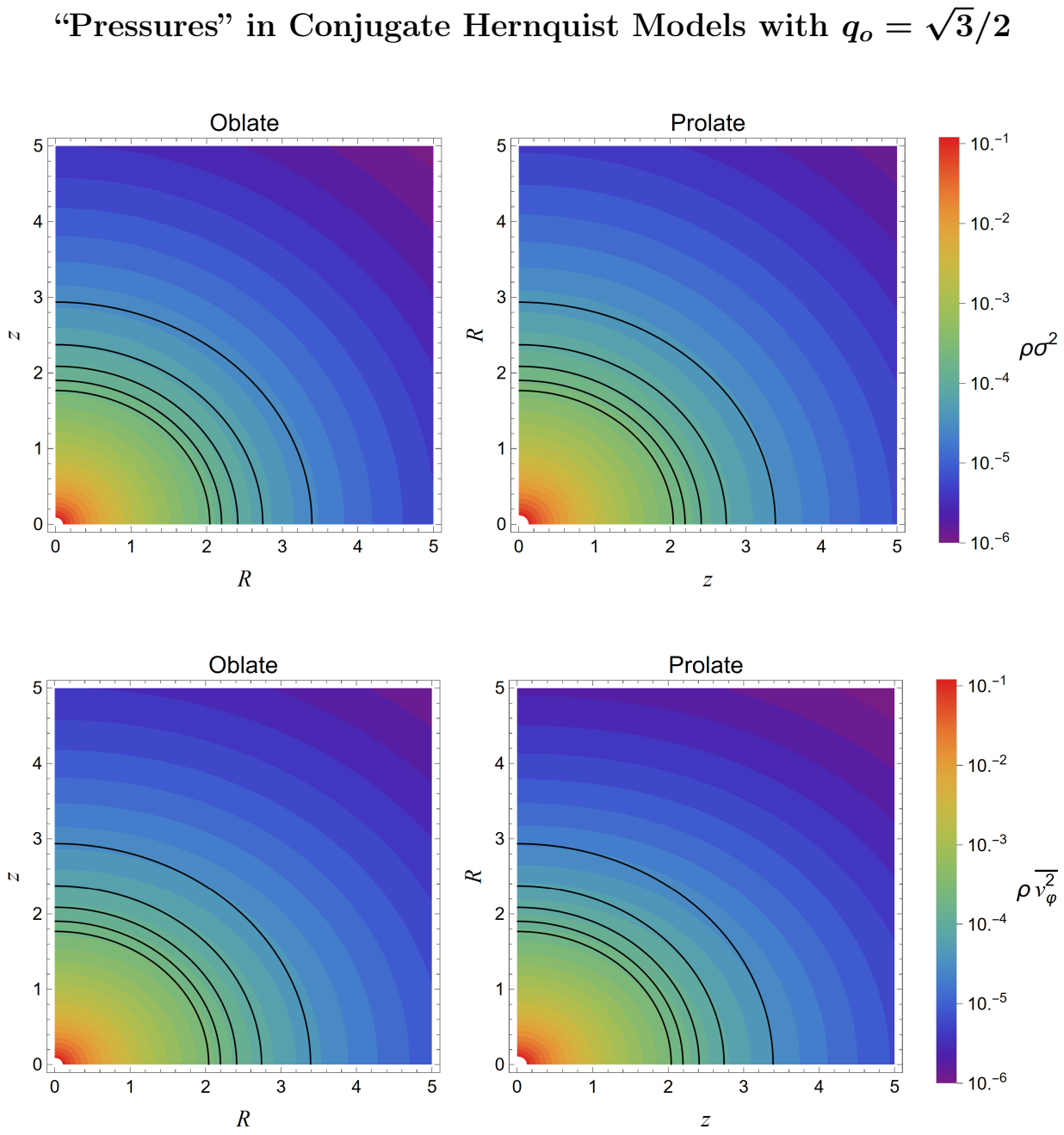

Figure 6.4. Maps in the (R,z)-plane of $\rho\sigma^2$ (upper panels) and $\rho\overline{v_\varphi^2}$ (lower panels) for oblate (left panels) and prolate (right panels) conjugate Hernquist models, with axial ratio of the oblate system $q_o = \sqrt{3}/2$, in common units of GM^2/a_o^4. R and z are in units of the oblate scale length a_o, and z denotes the symmetry axis. Black solid lines represent isodensity contours of the stellar distribution. The logarithmic colour scale is the same for $\rho\sigma^2$ and $\rho\overline{v_\varphi^2}$.

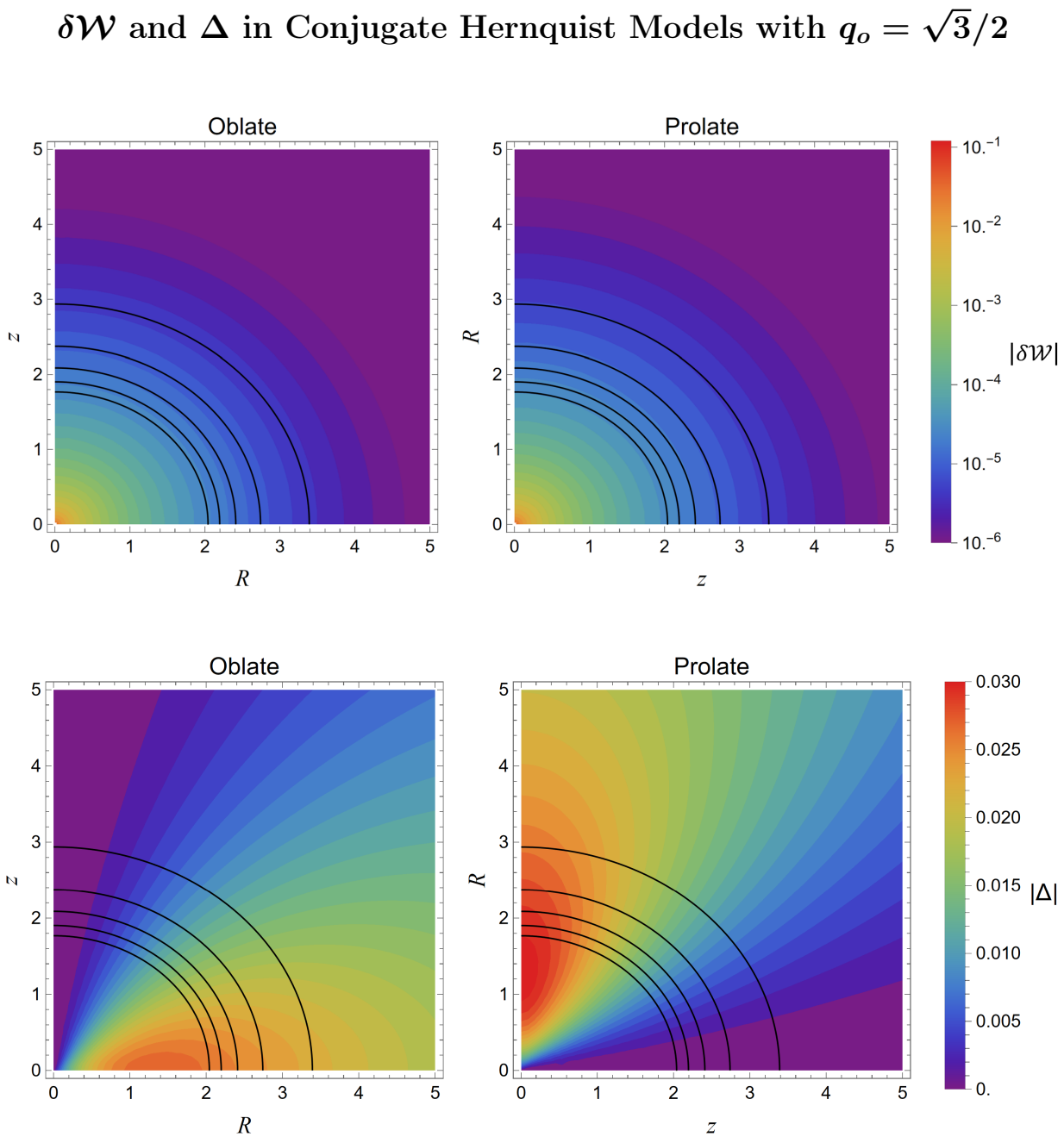

Figure 6.5. Upper panels: maps in the (R,z)-plane of $|\delta\mathcal{W}|$ for oblate (left) and prolate (right) conjugate Hernquist models, with axial ratio of the oblate system $q_o = \sqrt{3}/2$, in common units of GM^2/a_o^4. Bottom panels: maps in the (R,z)-plane of $|\Delta|$ for oblate (left) and prolate (right) conjugate Hernquist models, with axial ratio of the oblate system $q_o = \sqrt{3}/2$, in common units of GM/a_o. In all panels, R and z are in units of the oblate scale length a_o, z denotes the symmetry axis and black solid lines represent isodensity contours of the stellar distribution.

6.2 Projected kinematical fields

In Section 6.1, we considered the intrinsic dynamical quantities σ^2 and $\overline{v_\varphi^2}$ for conjugate oblate-prolate systems. However, the quantities that are actually accessible through observations are the projection of the intrinsic velocity fields on the plane of the sky. Therefore, to allow our models to be compared with observational data, we must compute the line-of-sight (los) velocity dispersion $\sigma_{\rm los}$ and line-of-sight rotational velocity $v_{\rm los}$. Moreover, since no qualitative differences emerged in the intrinsic fields between oblate and prolate models, it is natural to ask whether significant differences arise once they are projected.

6.2.1 Projections formulae

We present here the projection formulae in the edge-on case. We choose the line to sight to be aligned with the x-axis. The line-of-sight rotational velocity $v_{\rm los}$, which indicates ordered motion along the line of sight, is obtained as

$$\Sigma v_{\rm los} = \int_{-\infty}^{\infty} \rho\overline{v_\varphi}\langle \hat{\mathbf{e}}_\varphi, \hat{\mathbf{e}}_x\rangle dx, \tag{6.4}$$

where Σ is the surface mass density, $\hat{\mathbf{e}}_\varphi = (-\sin\varphi, \cos\varphi, 0)$ is the unit vector in the azimuthal direction, $\hat{\mathbf{e}}_x = (1,0,0)$ is unit vector along the x-axis and with $\langle\,\cdot\,,\,\cdot\,\rangle$ we indicate the standard inner product. Since $\sin\varphi = y/R$ and recalling that $R = \sqrt{x^2+y^2}$, a simple change of variables yields

$$\Sigma v_{\rm los} = 2y\int_y^{\infty} \frac{\rho\overline{v_\varphi}}{\sqrt{R^2-y^2}} dR. \tag{6.5}$$

The line-of-sight velocity dispersion $\sigma_{\rm los}$ can be written as (Ciotti and Pellegrini 1996; Posacki et al. 2013)

$$\sigma_{\rm los}^2 = \sigma_{\rm P}^2 + V_{\rm P}^2 - v_{\rm los}^2, \tag{6.6}$$

where

$$\Sigma\sigma_{\rm P}^2 = \int_{-\infty}^{\infty} \rho\langle \sigma^2\hat{\mathbf{e}}_x, \hat{\mathbf{e}}_x\rangle dx, \quad \Sigma V_{\rm P}^2 = \int_{-\infty}^{\infty} \rho\overline{v_\varphi}^2\langle \hat{\mathbf{e}}_\varphi, \hat{\mathbf{e}}_x\rangle^2 dx. \tag{6.7}$$

We thus have, after some algebra,

$$\Sigma\sigma_{\rm los}^2 = 2\int_y^{\infty} \frac{R^2\sigma^2 + y^2\Delta}{R\sqrt{R^2-y^2}}\rho dR - \Sigma v_{\rm los}^2. \tag{6.8}$$

6.2.2 The λ-decomposition for $\overline{v_\varphi^2}$

When computing $v_{\rm los}$ and $\sigma_{\rm los}$, knowing the ordered velocity $\overline{v_\varphi}$ along the azimuthal direction is necessary, as it enters the projection formulae. However from the JEs we can only derive $\overline{v_\varphi^2} = \sigma_\varphi^2 + \overline{v_\varphi}^2$. Therefore, we need to choose a decomposition of $\overline{v_\varphi^2}$ in its streaming and dispersion components. The most commonly used one for axisymmetric models is the Satoh (1980) k-decomposition:

$$\overline{v_\varphi} = k\sqrt{\Delta}, \quad \sigma_\varphi^2 = \sigma^2 + (1-k^2)\Delta, \tag{6.9}$$

where k is a constant parameter with $0 \leq k^2 \leq 1$. However, this decomposition can be used only when $\Delta \geq 0$ everywhere in the model and we saw in Chapter 4 that this is true only for oblate systems. Since we want to compare oblate and prolate models, we need a different decomposition, valid for both systems. A general one, which can be applied to both oblate and prolate models is the following, which we refer to as the λ-*decomposition*:

$$\overline{v_\varphi} = \lambda\sqrt{\overline{v_\varphi^2}}, \quad \sigma_\varphi^2 = (1-\lambda^2)\overline{v_\varphi^2}, \tag{6.10}$$

where λ is a constant parameter with $0 \leq \lambda^2 \leq 1$. $\lambda = 0$ corresponds to no net rotation in the azimuthal direction, and $\lambda^2 = 1$ corresponds to a maximally rotating system.

6.2.3 Results

We compute $\sigma_{\rm los}$ and $v_{\rm los}$ in Hernquist non-rotating and rotating conjugate models, adopting the λ-decomposition described above. To ensure $\overline{v_\varphi^2} \geq 0$ in the prolate model, we compare, as in the intrinsic case, an oblate system with axial ratio $q_o = \sqrt{3}/2$ and its conjugate prolate system with $q_p = 2/\sqrt{3}$. The values of $\sigma_{\rm los}$ and $v_{\rm los}$ are derived numerically using a specifically developed code in the `Mathematica` software, with a procedure analogous to that explained in Section 6.1.1.

Non-rotating systems

We start by considering the simplest case, in which both the oblate and prolate ellipsoids are non-rotating ($\lambda = 0$), i.e., $v_{\rm los} = 0$, so that $\sigma_{\rm los} = \sigma_{\rm P}$, from equation (6.6). The corresponding maps are shown in Figure 6.6.

We observe that the spatial distribution of $\sigma_{\rm los}$ is qualitatively similar in both models: the maximum value is located near the centre of the projection plane and the values decrease outward. In the prolate model, $\sigma_{\rm los}$ reaches a higher central value compared to the oblate case and decreases more steeply with distance from the centre. However, despite the different intrinsic shape of the two ellipsoids, the overall range of $\sigma_{\rm los}$ values remains remarkably close in both models. This similarity is likely a consequence of the fact that, in order to ensure consistency, the axial ratio must remain close to unity, restricting the models to nearly spherical configurations.

To quantify the relative variation between the two models, Figure 6.7 shows their percentage difference, computed as

$$\delta = 100 \times \frac{\sigma_{\rm los}^o - \sigma_{\rm los}^p}{\sigma_{\rm los}^o}. \tag{6.11}$$

Within the considered region, which for the Hernquist profile corresponds to approximately two effective radii, that is the typical region probed by observations, the two models differ by $\approx 10\%$ in the central region and up to $\approx 20\%$ in the outer regions.

Such small deviations, combined with the similar spatial distribution of $\sigma_{\rm los}$ in the two systems, suggest that, in absence of rotation, distinguishing between oblate and prolate galaxies only through the line-of-sight velocity dispersion may be challenging in practice.

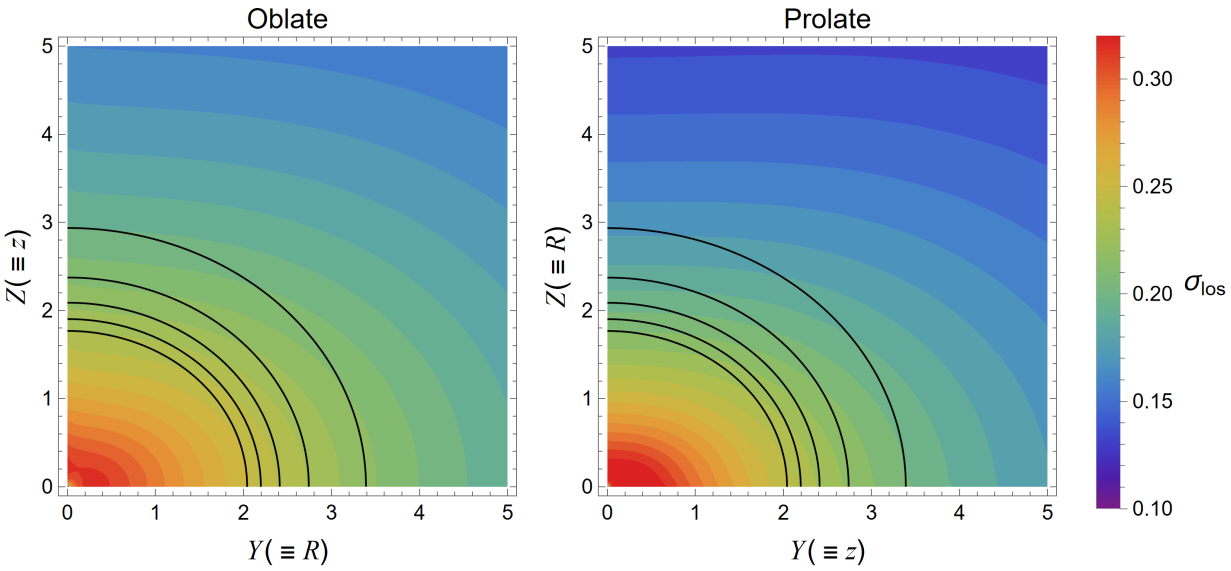

Figure 6.6. Maps in the (Y,Z) projection plane of σ_{los} for non-rotating ($\lambda = 0$) oblate (left) and prolate (right) conjugate Hernquist models, with axial ratio of the oblate system $q_o = \sqrt{3}/2$, in common units of $\sqrt{GM/a_o}$. Y and Z are in units of the oblate scale-length a_o. Black solid lines represent isodensity contours of the stellar distribution.

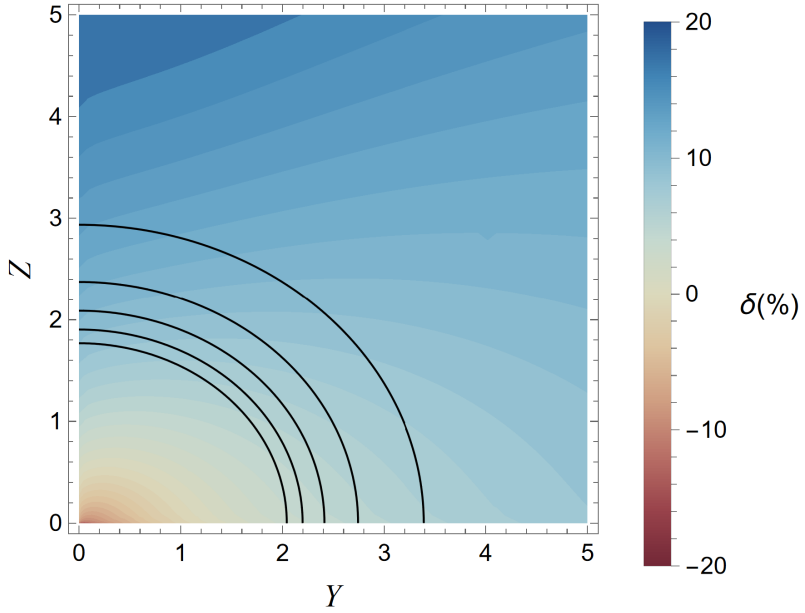

Figure 6.7. Percentage relative difference, computed as in equation (6.11), of σ_{los}, in non-rotating conjugate Hernquist models with axial ratio of the oblate system $q_o = \sqrt{3}/2$. (Y, Z) is the projection plane. Y and Z are in units of the oblate scale length a_o. Black solid lines indicate isodensity contours of the stellar distribution.

Rotating systems

We now compare rotating conjugate Hernquist systems, adopting different values of the parameter λ. Clearly, if rotation is present, oblate and prolate ellipsoids rotate around their symmetry axes which correspond to the projected semi-minor axis (oblate) and semi-major axis (prolate). As a result, we expect to be able to easily distinguish the two intrinsic shapes.

In Figure 6.8 we show $\sigma_{\rm los}$ and $v_{\rm los}$, in the projection plane, for $\lambda = 1/\sqrt{2}$, so that $\overline{v_\varphi^2}$ is equally divided between mean streaming motion and velocity dispersion. As expected, $v_{\rm los}$ is different in the two models: we observe a gradient along the projected major axis in the oblate case, and a gradient along the projected minor axis in the prolate case. As far as $\sigma_{\rm los}$ is concerned, the two maps start to differ significantly, which is to be expected, since $\sigma_{\rm los}$ depends on $v_{\rm los}$.

In Figure 6.9 we present $v_{\rm los}$ and $\sigma_{\rm los}$ for $\lambda = 1$, corresponding to purely rotating systems. We can see that $v_{\rm los}$ and $\sigma_{\rm los}$ reach higher values compared to the previous case, but the general behaviour is analogous to that discussed before. Additionally, we note that, for a fixed λ, the oblate system rotates faster than its conjugate prolate.

We conclude that, when ordered rotation is present, oblate and prolate shapes can be clearly distinguished.

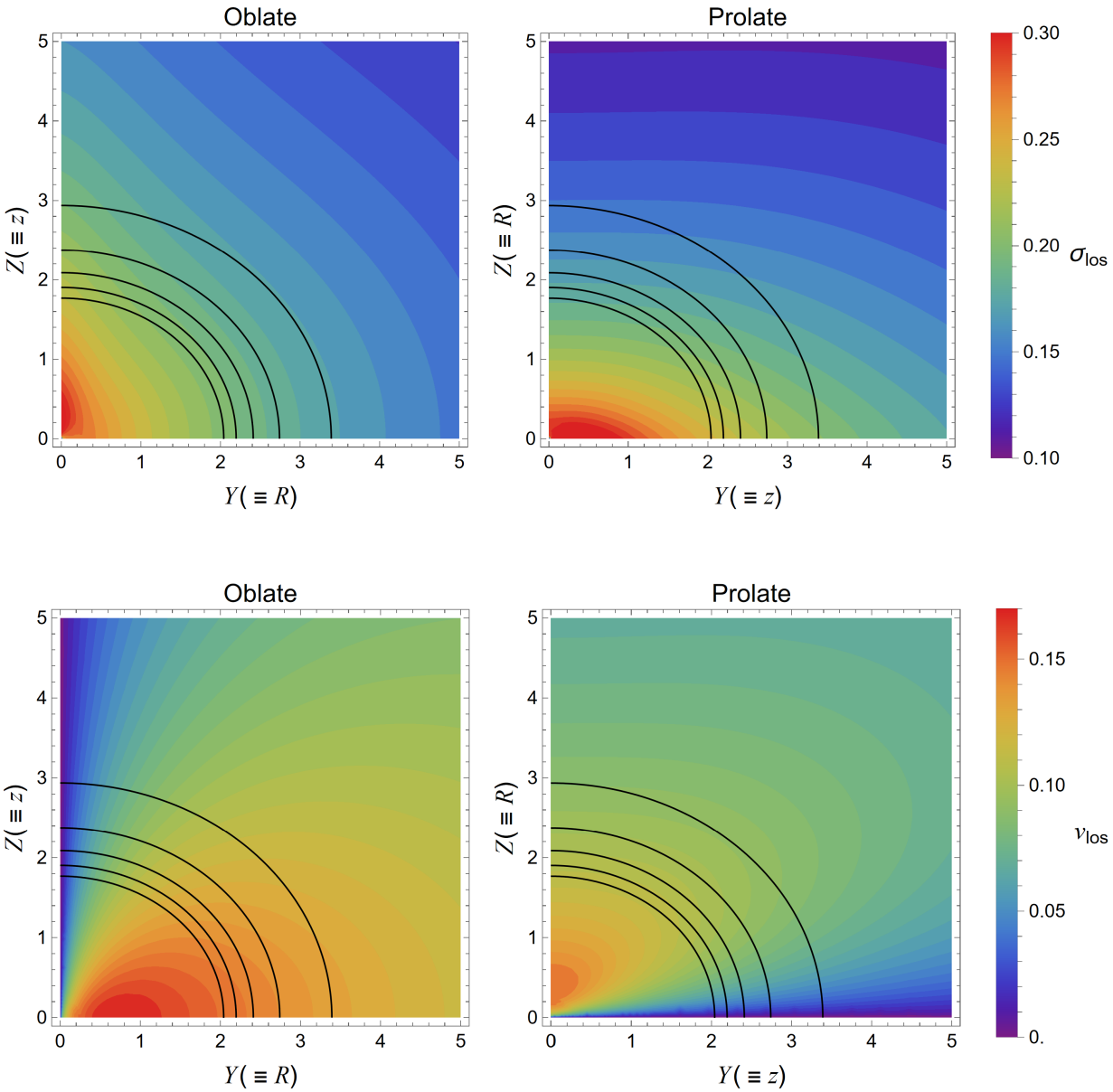

Figure 6.8. Maps in the (Y,Z) projection plane of $\sigma_{\rm los}$ for rotating ($\lambda = 1/\sqrt{2}$) oblate (left) and prolate (right) conjugate Hernquist models, with axial ratio of the oblate system $q_o = \sqrt{3}/2$, in common units of $\sqrt{GM/a_o}$. Y and Z are in units of the oblate scale-length a_o. Black solid lines represent isodensity contours of the stellar distribution.

Projected Rotating ($\lambda = 1$) Conjugate Hernquist Models with $q_o = \sqrt{3}/2$

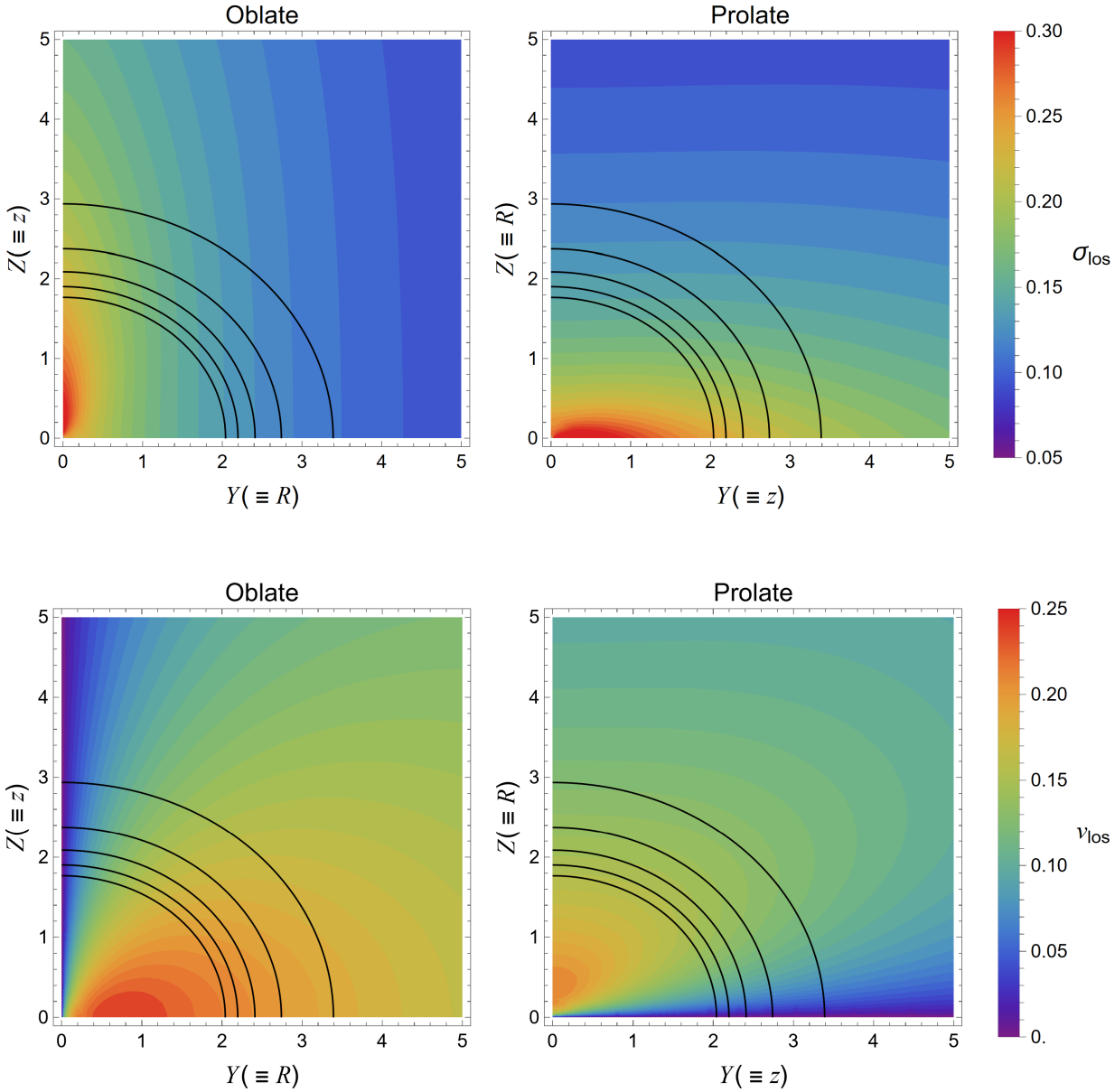

Figure 6.9. Maps in the (Y,Z) projection plane of $\sigma_{\rm los}$ for rotating ($\lambda = 1$) oblate (left) and prolate (right) conjugate Hernquist models, with axial ratio of the oblate system $q_o = \sqrt{3}/2$, in common units of $\sqrt{GM/a_o}$. Y and Z are in units of the oblate scale-length a_o. Black solid lines represent isodensity contours of the stellar distribution.

CHAPTER 7

Discussion and Conclusions

Elliptical galaxies are stellar systems that can be described fairly well as ellipsoidally stratified systems. Observations show that they can be triaxial or axisymmetric, and in the last case both oblate and prolate. The internal dynamics of oblate systems is understood quite well (mainly because they can be imagined in a qualitative sense as rotating fluid systems), while prolate galaxies present some additional difficulties for a satisfactory understanding (for example, no self-gravitation prolate fluid systems at equilibrium can exist).

In this thesis we carried out a theoretical analysis of various aspects of the structure and dynamics of prolate systems. We found it particularly useful to introduce and compare *conjugate pairs* of oblate and prolate galaxies, defined as pair of oblate-prolate models with the same total mass, the same intrinsic density profile, and the same edge-on surface brightness distribution.

The main results obtained in this work can be summarised as follows.

- In Chapter 2, we first discussed in depth why the comparison of oblate and prolate systems, even though trivial at first sight, is not so. In fact, it is immediate to realise that, given a spherical galaxy of fixed mass, one could construct from it either a very small or very large prolate model, and likewise a very small or very large oblate one. Clearly, comparing the dynamical properties of a large prolate model with those of a small, denser oblate model would lead to different results than comparing the opposite pair. It follows that additional constraints must be applied for such a comparison. In this chapter we showed how, remarkably and non-trivially, the following three conditions are necessary and sufficient to establish a physically meaningful comparison: same total mass, same intrinsic (normalised) density profile, same surface brightness profile. We proved that, considering systems with density stratified on ellipsoids, i.e., $\rho = \rho(m)$, it is indeed possible to construct oblate–prolate pairs satisfying simultaneously all these requirements, provided that two specific relations between their scale-lengths and axial ratios hold. We referred to such pairs as *conjugate systems*. Models in the same conjugate pair, despite having the same surface brightness profile, do not have the same density. The prolate system is, in fact, uniformly denser than its conjugate oblate counterpart.

- Chapter 3 is entirely based on the use of the Tensor Virial Theorem to determine the main "global" energetic differences between oblate and prolate systems with density

$\rho(m)$, first for generic systems, and then for the specific case of conjugate pairs. In particular, we focused on ratios between diagonal components of the potential energy tensor W_{ij}. We computed W_{RR}/W_{zz} (where $W_{RR} = W_{xx} + W_{yy} = 2W_{xx}$) and found that, in oblate systems, this ratio is > 2 and increases for increasing flattenings. In contrast, in prolate systems the value of this ratio decreases for increasing elongations (starting from 2 in the spherical limit) and falls below 1 for $q \approx 2.59$. We further discussed this point considering the ratio $W_{xx}/W_{zz} = W_{RR}/2W_{zz}$. We found that, given an oblate system of flattening q, its W_{xx}/W_{zz} value is not the inverse of W_{xx}/W_{zz} in the corresponding prolate system with axial ratio $1/q$. Therefore, in this sense, oblate and prolate systems are *not energetically "inverted" systems*. Restricting our analysis to classical two-integral systems, two further results emerged: isotropic prolate systems cannot exist (being mathematically equivalent to fluid systems), and two-integral prolate systems cannot exceed an axial ratio of approximately $q \approx 2.59$. In the subsequent comparison of conjugate systems, we computed W^o_{RR}/W^p_{RR} and found that this ratio is always greater than unity and converges to $\pi/2$ for $q_o \to 0$, while W^o_{zz}/W^p_{zz} is lower than unity and tends to 0 for $q_o \to 0$. All these results are completely independent of the adopted density profile, due to Roberts (1962)'s theorem.

- In Chapter 4 we moved from the study of the virial properties, to the analysis of the internal dynamics, starting from its most basic ingredient i.e., the gravitational field. We revisited an argument originally proposed by Newton and provided a simple and intuitive way to understand the conditions for equilibrium in axisymmetric ellipsoidal systems. We first proved that, for ellipsoidally stratified systems with $\frac{d\rho}{dm} \leq 0$, at any given isodensity surface m, the gravitational field along the symmetry axis $g_z(0, mq)$ is weaker than that in the radial direction $g_R(m, 0)$ for prolate ellipsoids, while the opposite occurs in oblate ones. We also showed that, if instead of the gravitational field we fix a point in the ellipsoid and look at the "weights" of the vertical and radial density columns outside that point, the vertical one is heavier in prolate systems, while the radial one dominates in oblate systems. It is the balance of these columns point by point which ultimately enables equilibrium. We then showed how the JEs for two-integral systems can be interpreted within this framework. We found that, in prolate systems, the condition on weights, that are now interpreted in terms of "pressure", physically explains the known analytical result of $\Delta \equiv \overline{v^2_\varphi} - \sigma^2 \leq 0$ everywhere, a condition possible only with anisotropic velocity dispersion. In contrast, oblate systems have $\Delta \geq 0$ everywhere, hence, they can, in principle, be in equilibrium also in the fully isotropic case.

- In Chapter 5, we continued the study of the JEs and investigated the sign of $\overline{v^2_\varphi}$ in two-integral systems to discard inconsistent models. Of course, in oblate systems, $\overline{v^2_\varphi} \geq 0$ everywhere, regardless of the axial ratio and density profile. For prolate systems, we analysed three representative density profiles: Gaussian, power-law and Sérsic. We found that Gaussian models are always inconsistent, while for power-law profiles, we derived a sufficient condition for the positivity of $\overline{v^2_\varphi}$, showing that shallower profiles can support more elongated systems. For Sérsic models, we found that they are inevitably inconsistent at large radii, although the critical radius at which this occurs can be extended beyond $\approx 10R_e$ for nearly spherical systems. Finally, we provided a more detailed analysis of the inconsistent regions for Gaussian

and power-law profiles. In Gaussian models $\overline{v_\varphi^2} < 0$ outside a cylinder centred on the symmetry axis, with radius decreasing as q increases. In power-law models, $\overline{v_\varphi^2} < 0$ outside a conical surface, whose opening angle decreases for increasing q and increasing steepness of the density profile.

- In Chapter 6, we finally focused on analogies and differences between oblate and prolate systems in conjugate pairs, comparing their kinematical fields. We numerically recovered σ^2 and $\overline{v_\varphi^2}$ and then derived the projected kinematical quantities $v_{\rm los}$ and $\sigma_{\rm los}$ adopting the λ-decomposition $\overline{v_\varphi} = \lambda\sqrt{\overline{v_\varphi^2}}$, which enables the introduction of rotational support also in systems with $\Delta < 0$, as far as $\overline{v_\varphi^2} \geq 0$. In non-rotating systems, $\sigma_{\rm los}$ is strikingly similar between oblate and prolate conjugate pairs, with relative variations up to 20% in the typical regions probed by observations. In rotating systems, instead, the fact that oblate and prolate ellipsoids can have ordered rotation only around their symmetry axis allows for an immediate distinction between the two shapes. We noticed also that, for equal value of λ, the oblate system rotates faster than the prolate one. We conclude that conjugate systems are more likely to be kinematically distinguished only in presence of ordered rotation.

With this thesis, we have therefore provided convincing evidence that oblate and prolate galaxies are not simply "inverse" systems obtained by just "compressing" or elongating a sphere along a given direction, but they are intrinsically *different* objects with the *only* common properties of being ellipsoids and axisymmetric.

All the results regarding consistency obtained and presented in this thesis concern collisionless axisymmetric systems described by a two-integral phase-space distribution function. The natural follow-up to this work will therefore be the study of the effects of breaking the rigid constraints imposed by two-integral distribution functions, to investigate how the consistency region in parameter space expands when a third integral of motion is included and what are the intrinsic limitations of prolate geometry on the model existence, even in the three-integral case.

APPENDIX A

Concepts of Stellar Dynamics

A.1 The distribution function

At any given time t, the dynamical state of a collisionless stellar system is fully described by its distribution function (DF), $f(\mathbf{x}, \mathbf{v}, t)$, where $\mathbf{x}$ and $\mathbf{v}$ denote the position in configuration space and the velocity, respectively. The DF is such that $f(\mathbf{x}, \mathbf{v}, t)d^3\mathbf{x}d^3\mathbf{v}$ is the mass of stars in the phase-space volume $d^3\mathbf{x}d^3\mathbf{v}$ centred in $(\mathbf{x}, \mathbf{v})$. Thus f represents the mass density of stars in the phase space at time t, and when integrated over the entire phase space, it gives the total mass of the system.

As f evolves in time, imposing that the total mass of the system is conserved leads to the continuity equation:

$$\frac{\partial f}{\partial t} + \frac{\partial f}{\partial w_i}\dot{w}_i = 0, \tag{A.1}$$

where the Einstein convention is adopted, implying a summation over repeated indices. In equation (A.1), w_i, with $i = 1, ..., 6$, are the components of the vector $\mathbf{w}$, which denotes a point in phase-space. In Cartesian coordinates, it has components $\mathbf{w} = (\mathbf{x}, \mathbf{v})$, and its time derivative is $\dot{\mathbf{w}} = (\mathbf{v}, -\nabla\Phi)$, where Φ is the total gravitational potential in which the system is embedded.

Substituting these expressions into equation (A.1), we obtain the collisionless Boltzmann equation (CBE) in Cartesian coordinates:

$$\frac{\partial f}{\partial t} + v_i\frac{\partial f}{\partial x_i} - \frac{\partial \Phi}{\partial x_i}\frac{\partial f}{\partial v_i} = 0. \tag{A.2}$$

A.2 The Jeans's theorems

We now introduce two theorems concerning the DF which are extremely useful in stellar dynamics. Under specific assumptions, they constrain the functional dependence of the DF to integrals of motion.

An integral of motion $I(\mathbf{x}, \mathbf{v})$ is defined as a function of the phase-space coordinates

alone that is constant along an orbit. Therefore we can write

$$\frac{\partial I}{\partial x_i} v_i - \frac{\partial I}{\partial v_i} \frac{\partial \Phi}{\partial x_i} = 0. \tag{A.3}$$

Comparing this equation with the CBE in the stationary case, we notice that the condition for being an integral of motion is identical to that for being a steady state solution of the CBE. We can thus introduce the **Jeans's theorem** which states that *any steady-state solution of the CBE depends on the phase-space coordinates only through integrals of motions and any integral of motion is a steady-state solution of the CBE.*

This means that we can write

$$f(\mathbf{x}, \mathbf{v}) = f(I_1, \ldots, I_N), \tag{A.4}$$

where $I_1, \ldots, I_N$ are N integrals of motion.

Additionally, if the potential of a steady-state galaxy is such that almost all orbits are regular, the **Strong Jeans's theorem** ensures that the DF is a function only of three isolating integrals of motion.

The models that we are interested in studying in this thesis are stationary and axisymmetric systems. Their classical two integrals of motion are the energy E and the component L_z of the angular momentum along the symmetry axis z. As a consequence, for such systems we can have $f = f(E, L_z)$ or $f = f(E, L_z, I_3)$, where the explicit form of I_3 is, in general, unknown.

A.3 Velocity moments of the distribution function

All observable properties of stellar systems can be expressed in terms of the moments of the DF, which are defined as follows.

The zero-order moment of the DF corresponds to the **mass density**:

$$\rho(\mathbf{x}, t) = \int_{\mathbb{R}^3} f d^3\mathbf{v}. \tag{A.5}$$

The first-order moments are the **mean velocity components**:

$$\overline{v_i} = \frac{1}{\rho} \int_{\mathbb{R}^3} f v_i d^3\mathbf{v}, \quad i = 1, 2, 3 \tag{A.6}$$

The second-order moments are defined by considering products of two velocity components. For example, we define, for $i, j = 1, 2, 3$,

$$\overline{v_i v_j} = \frac{1}{\rho} \int_{\mathbb{R}^3} f v_i v_j d^3\mathbf{v}, \tag{A.7}$$

$$\sigma_{ij}^2 = \frac{1}{\rho} \int_{\mathbb{R}^3} f (v_i - \overline{v_i})(v_j - \overline{v_j}) d^3\mathbf{v}. \tag{A.8}$$

The values σ_{ij}^2 are the components of the **velocity dispersion tensor** and, developing

the product in equation (A.8), we can write them as

$$\sigma_{ij}^2 = \overline{v_i v_j} - \overline{v_i}\,\overline{v_j}, \tag{A.9}$$

which clearly shows that the velocity dispersion tensor is symmetric with positive diagonal components.

Higher-order velocity moments are obtained analogously by considering the product of more velocity components.

A.3.1 Second-order velocity moments in axisymmetric stationary systems

We now discuss some properties of the velocity moments defined above in the case of axisymmetric stationary systems.

As explained in Section A.2, for these systems the Jeans's theorem holds and for the majority of them, the strong Jeans's theorem is also valid. Hence we can assume $f(E, L_z)$ or $f(E, L_z, I_3)$.

- Case $f(E, L_z)$:

  In cylindrical coordinates E and L_z are

  $$E = \frac{1}{2}(v_R^2 + v_z^2 + v_\varphi^2) + \Phi, \quad L_z = R v_\varphi, \tag{A.10}$$

  where $R = \sqrt{x^2 + y^2}$ is the cylindrical radius. Therefore, the first-order velocity moments $\overline{v_R}$ and $\overline{v_z}$ are null as they involve an integral of an odd function. For the same reason, $\overline{v_R v_z} = \overline{v_R v_\varphi} = \overline{v_z v_\varphi} = 0$

  From equation (A.7), with $i = j$, we have that $\overline{v_R^2} = \overline{v_z^2} \neq \overline{v_\varphi^2}$.

  With these conditions, the velocity dispersion tensor is diagonal with components $\sigma_R^2 \equiv \sigma_{RR}^2 = \overline{v_R^2}$, $\sigma_z^2 \equiv \sigma_{zz}^2 = \overline{v_z^2}$ and $\sigma_\varphi^2 \equiv \sigma_{\varphi\varphi}^2$, where $\sigma_R^2 = \sigma_z^2$.

- Case $f(E, L_z, I_3)$:

  In this case, we cannot say anything on the velocity moments without knowing the explicit form of I_3. A common assumption in dynamical model is that I_3 is such that all mixed velocity moments vanish, so that the velocity dispersion tensor is diagonal. Furthermore, one may impose a prescribed relation between σ_z^2 and σ_R^2. A common example is the Cappellari (2008) b-anisotropy, where $\sigma_R^2 = b(R, z)\sigma_z^2$.

APPENDIX B

Virial Coefficients

We present here the coefficient w_i entering the second order TVT, introduced in Section 3.1. In the case of axisymmetric systems, they can be expressed in terms of elementary functions (Binney and Tremaine 2008; Ciotti 2021).
They are, in the oblate case ($q < 1$),

$$\begin{cases} w_1 = w_2 = a^3 q \displaystyle\int_0^\infty \frac{d\tau}{(a^2+\tau)^2\sqrt{a^2q^2+\tau}} = \frac{q}{1-q^2}\left(\frac{\arcsin\sqrt{1-q^2}}{\sqrt{1-q^2}} - q\right), \\ \\ w_3 = a^3 q \displaystyle\int_0^\infty \frac{d\tau}{(a^2+\tau)(a^2q^2+\tau)^{3/2}} = \frac{2q}{1-q^2}\left(\frac{1}{q} - \frac{\arcsin\sqrt{1-q^2}}{\sqrt{1-q^2}}\right), \end{cases} \tag{B.1}$$

and, in the prolate case ($q > 1$),

$$\begin{cases} w_1 = w_2 = a^3 q \displaystyle\int_0^\infty \frac{d\tau}{(a^2+\tau)^2\sqrt{a^2q^2+\tau}} = \frac{q}{q^2-1}\left(q - \frac{\operatorname{arctanh}\frac{\sqrt{q^2-1}}{q}}{\sqrt{q^2-1}}\right), \\ \\ w_3 = a^3 q \displaystyle\int_0^\infty \frac{d\tau}{(a^2+\tau)(a^2q^2+\tau)^{3/2}} = \frac{2q}{q^2-1}\left(\frac{\operatorname{arctanh}\frac{\sqrt{q^2-1}}{q}}{\sqrt{q^2-1}} - \frac{1}{q}\right). \end{cases} \tag{B.2}$$

Note that, in the spherical limit, $w_1 = w_2 = w_3 = 2/3$.

APPENDIX C

Useful Proofs

We report here the full proofs of the theorems stated in Chapter 4.

Theorem 1. *Let*

$$m^2 = R^2 + \frac{z^2}{q^2}, \quad q > 0, \tag{4.21}$$

and let the density of an axisymmetric ellipsoidal system be $\rho = \rho(m)$*, with*

$$\frac{d\rho}{dm} \leq 0. \tag{4.22}$$

Let $g_R(R,z)$ *and* $g_z(R,z)$ *be the magnitude of the gravitational field of the ellipsoid along* R *and* z*, respectively, at the point* (R,z)*. Then,* $\forall m$*,*

$$\begin{aligned} &g_R(m,0) < g_z(0,mq) \quad \textit{if} \quad q<1 \ \textit{(oblate)}, \\ &g_R(m,0) > g_z(0,mq) \quad \textit{if} \quad q>1 \ \textit{(prolate)}. \end{aligned} \tag{4.23}$$

Proof. The proof is organised in two steps: we first prove the theorem for constant density ellipsoids, then we exploit this result to prove the theorem for general decreasing density profiles.

For simplicity, let us define $\Delta g \equiv g_z(0,mq) - g_R(m,0)$, so that the theorem is verified if

$$\begin{aligned} &\Delta g > 0 \quad if \quad q<1 \text{ (oblate)}, \\ &\Delta g < 0 \quad if \quad q>1 \text{ (prolate)}. \end{aligned} \tag{C.1}$$

Let us consider a constant-density ellipsoid with density ρ_0. From equation (4.5),

$$\Delta g = 2\pi G \rho_0 m (q w_3 - w_1). \tag{C.2}$$

If $q<1$, substituting the corresponding values of w_3 and w_1, given in Appendix B,

$$\begin{aligned} \Delta g &= \frac{2\pi G\rho_0 mq(1+2q)}{(1-q^2)^{3/2}} \left(\frac{(2+q)\sqrt{1-q^2}}{1+2q} - \arcsin\sqrt{1-q^2} \right) \\ &= \frac{2\pi G\rho_0 mq(1+2q)}{(1-q^2)^{3/2}} \mathcal{F}(q). \end{aligned} \tag{C.3}$$

We have that

$$\frac{d\mathcal{F}}{dq} = -\frac{2(1-q^2)^2(1+q)}{(1+2q)^2\sqrt{1-q^2}}, \tag{C.4}$$

so that $\mathcal{F}$ is monotonically decreasing, and since $\mathcal{F}(1) = 0$, then $\mathcal{F} > 0\ \forall q < 1$. It follows that $\Delta g > 0\ \forall q < 1$.

Analogously, if $q > 1$

$$\begin{aligned}\Delta g &= \frac{2\pi G\rho_0 mq(1+2q)}{(q^2-1)^{3/2}}\left[-\frac{(2+q)\sqrt{q^2-1}}{1+2q} + \operatorname{arctanh}\left(\frac{\sqrt{q^2-1}}{q}\right)\right] \\ &= \frac{2\pi G\rho_0 mq(1+2q)}{(q^2-1)^{3/2}}\mathcal{G}(q).\end{aligned} \tag{C.5}$$

We have that

$$\frac{d\mathcal{G}}{dq} = -\frac{2(q^2-1)^2(1+q)}{(1+2q)^2\sqrt{q^2-1}}, \tag{C.6}$$

$\mathcal{G}$ is monotonically decreasing, and since $\mathcal{G}(1) = 0$, then $\mathcal{G} < 0\ \forall q < 1$. It follows that $\Delta g < 0\ \forall q > 1$. The theorem is thus verified for constant-density ellipsoids.

Let us now consider a generic ellipsoidal system with $\rho(m)$. Then,

$$\Delta g = 2\pi G m(1-q^2)\int_0^\infty \rho\left(\frac{m}{\sqrt{1+\tau}}\right)\mathcal{H}(q,\tau)d\tau, \tag{C.7}$$

where

$$\mathcal{H}(q,\tau) = \frac{(1+q^2)\tau^2+\tau-1}{(1+\tau)^2(1+q^2\tau)(\sqrt{(1+\tau)(q^2+\tau)}+1+q^2\tau)\sqrt{q^2+\tau}}. \tag{C.8}$$

One can easily verify that $\forall q$, $\mathcal{H}$ has a positive root τ_+ and $\mathcal{H}(q,\tau) < 0$ for $\tau < \tau_+$ and $\mathcal{H}(q,\tau) > 0$ for $\tau > \tau_+$. Therefore, equation (C.7) can be rewritten as

$$\Delta g = 2\pi G m(1-q^2)\left(\mathcal{I}_- + \mathcal{I}_+\right), \tag{C.9}$$

where

$$\mathcal{I}_- \equiv \int_0^{\tau_+} \rho\left(\frac{m}{\sqrt{1+\tau}}\right)\mathcal{H}(q,\tau)d\tau < 0, \tag{C.10}$$

$$\mathcal{I}_+ \equiv \int_{\tau_+}^\infty \rho\left(\frac{m}{\sqrt{1+\tau}}\right)\mathcal{H}(q,\tau)d\tau > 0. \tag{C.11}$$

If $(\mathcal{I}_- + \mathcal{I}_+) > 0$ the sign of Δg is determined by the sign of $1-q^2$ and the proof is complete. To establish this inequality for any decreasing density profile, we use the fact that the theorem has already been proven for constant-density ellipsoids. Let us define

$$\rho_0 \equiv \rho\left(\frac{m}{\sqrt{1+\tau_+}}\right). \tag{C.12}$$

Since, by hypothesis, the density is a monotonically decreasing function of m, we have

$$\rho\left(\frac{m}{\sqrt{1+\tau}}\right) \le \rho_0 \quad (\tau < \tau_+), \qquad \rho\left(\frac{m}{\sqrt{1+\tau}}\right) \ge \rho_0 \quad (\tau > \tau_+). \tag{C.13}$$

Therefore

$$\int_0^{\tau_+} \rho\left(\frac{m}{\sqrt{1+\tau}}\right)\mathcal{H}(q,\tau)d\tau \geq \int_0^{\tau_+} \rho_0\mathcal{H}(q,\tau)d\tau, \tag{C.14}$$

$$\int_{\tau_+}^{\infty} \rho\left(\frac{m}{\sqrt{1+\tau}}\right)\mathcal{H}(q,\tau)d\tau \geq \int_{\tau_+}^{\infty} \rho_0\mathcal{H}(q,\tau)d\tau. \tag{C.15}$$

Summing the two yields

$$\mathcal{I}_- + \mathcal{I}_+ \geq \int_0^{\infty} \rho_0\mathcal{H}(q,\tau)d\tau \geq 0, \tag{C.16}$$

where the last inequality follows from the fact that the theorem is verified for constant-density ellipsoids. Finally, the arbitrariness of ρ_0 ensures that the inequality holds for any monotonic density distribution, which completes the proof. □

Theorem 2. *Let*

$$m^2 = R^2 + \frac{z^2}{q^2}, \quad q > 0, \tag{4.24}$$

and let the density of an axisymmetric ellipsoidal system be

$$\rho = \begin{cases} \rho(m) & m \leq m_t, \\ 0 & m > m_t. \end{cases} \tag{4.25}$$

where $m_t > 0$ is a truncation radius. Then, defining

$$R_t(z) = \sqrt{m_t^2 - \frac{z^2}{q^2}}, \quad z_t(R) = q\sqrt{m_t^2 - R^2}, \tag{4.26}$$

the following relation holds $\forall(R,z)$:

$$\begin{aligned} \int_R^{R_t} \rho\frac{\partial\Phi}{\partial R'}dR' - \int_z^{z_t} \rho\frac{\partial\Phi}{\partial z'}dz' = &\int_R^{R_t}\int_z^{z_t} \left(\frac{\partial\rho}{\partial R'}\frac{\partial\Phi}{\partial z'} - \frac{\partial\rho}{\partial z'}\frac{\partial\Phi}{\partial R'}\right)dz'dR' \\ &+ \int_R^{R_t} \rho(R', z_t')\frac{d\Phi(R', z_t')}{dR'}dR'. \end{aligned} \tag{4.27}$$

Proof. Let us compute

$$\begin{aligned} \frac{\partial}{\partial R}\int_z^{z_t} \rho\frac{\partial\Phi}{\partial z'}dz' &= \int_z^{z_t} \left(\frac{\partial\rho}{\partial R}\frac{\partial\Phi}{\partial z'} + \rho\frac{\partial^2\Phi}{\partial R\partial z'}\right)dz' + \rho(R,z_t)\left.\frac{\partial\Phi}{\partial z}\right|_{(R,z_t)}\frac{dz_t}{dR} \\ &= \int_z^{z_t} \left[\frac{\partial\rho}{\partial R}\frac{\partial\Phi}{\partial z'} + \frac{\partial}{\partial z'}\left(\rho\frac{\partial\Phi}{\partial R}\right) - \frac{\partial\rho}{\partial z'}\frac{\partial\Phi}{\partial R}\right]dz' + \rho(R,z_t)\left.\frac{\partial\Phi}{\partial z}\right|_{(R,z_t)}\frac{dz_t}{dR} \\ &= \int_z^{z_t} \left(\frac{\partial\rho}{\partial R}\frac{\partial\Phi}{\partial z'} - \frac{\partial\rho}{\partial z'}\frac{\partial\Phi}{\partial R}\right)dz' - \rho\frac{\partial\Phi}{\partial R} + \rho(R,z_t)\frac{d\Phi(R,z_t)}{dR} \end{aligned} \tag{C.17}$$

Since

$$-\rho\frac{\partial\Phi}{\partial R} = \frac{\partial}{\partial R}\int_R^{R_t} \rho\frac{\partial\Phi}{\partial R'}dR', \tag{C.18}$$

integrating with respect to R yields the desired conclusion. □

APPENDIX D

Jaffe and Gaussian Density Profiles

In Chapter 6, we computed σ^2 and $\overline{v_\varphi^2}$ for Hernquist conjugate models. Here we present the intrinsic velocity fields for two additional profiles: the Jaffe (1983) profile, defined as

$$\rho = \frac{M}{4\pi a^3 q}\frac{1}{m^2(1+m)^2}, \quad m^2 = \frac{R^2}{a^2} + \frac{z^2}{a^2 q^2}, \tag{D.1}$$

and the Gaussian profile, defined in equation (2.15). For both models, the σ^2 and $\overline{v_\varphi^2}$ are computed following the procedure described in Section 6.1.1.

Like the Hernquist profile, the Jaffe profile goes asymptotically as $\rho \propto m^{-4}$ as $m \to \infty$ and is flatter towards the centre of the system. Thus, from the condition (5.12), the limiting axial ratio that ensures $\overline{v_\varphi^2} \geq 0$ everywhere in the prolate system is $q_p = 2/\sqrt{3}$, which corresponds to $q_o = \sqrt{3}/2 \approx 0.866$. The resulting maps of σ^2 and $\overline{v_\varphi^2}$ are shown in Figure D.1. We note that the two quantities have similar values in the oblate and the prolate system and their spatial distribution is such that, when the two models have the same projected orientation, no qualitative differences are observed. Note also that, unlike the Hernquist profile, the Jaffe profile has an inner slope $\rho \propto r^{-2}$, resulting in velocity fields that approach a finite, non-zero central value.

In Figure D.2, we then consider conjugate Jaffe models with axial ratio of the oblate system $q_o = 1/2$ to illustrate the behaviour of σ^2 and $\overline{v_\varphi^2}$ with increasing flattening/elongation. We note that, the maximum values of σ^2 and $\overline{v_\varphi^2}$ increase with respect to the previous case, and the prolate system has, on average, higher velocity dispersion. Moreover, the maps of $\overline{v_\varphi^2}$ show that, as expected, the prolate system is inconsistent outside a conical region, symmetric around the z-axis. This result is in agreement with the analytic prediction of Section 5.2.2.

For the Gaussian profile, we compute σ^2 and $\overline{v_\varphi^2}$ in conjugate pairs with $q_o = \sqrt{3}/2$ and $q_o = 1/2$. The results are shown in Figure D.3 and Figure D.4. As expected, in both cases the prolate model is inconsistent. Moreover, as shown analytically in Section 5.1.1, the region with $\overline{v_\varphi^2} \geq 0$ is confined to a cylinder around the z-axis, which narrows down for increasing elongation of the model.

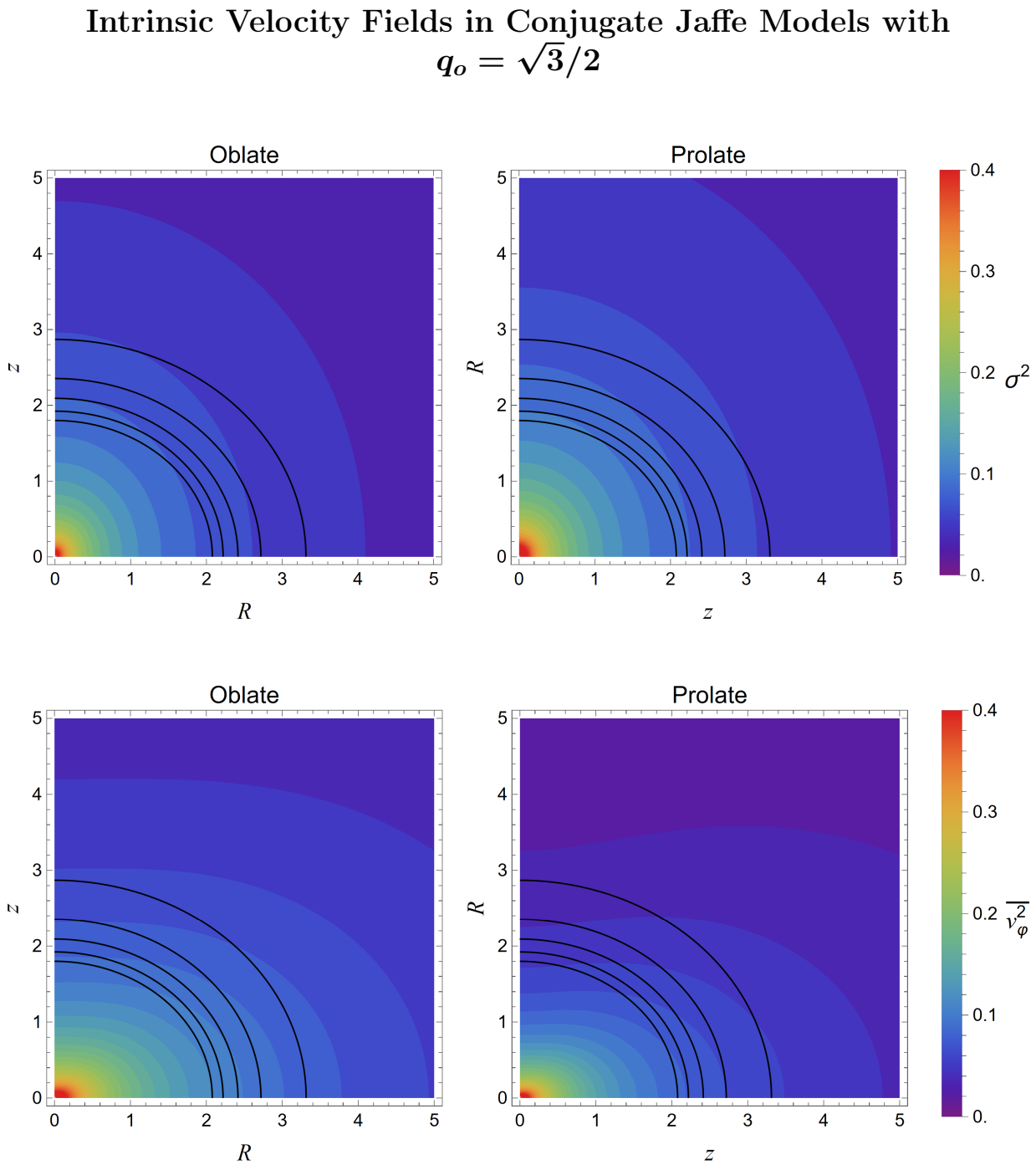

Figure D.1. Maps in the (R,z)-plane of σ^2 (upper panels) and $\overline{v_\varphi^2}$ (lower panels) for oblate (left panels) and prolate (right panels) conjugate Jaffe models with axial ratio of the oblate system $q_o = \sqrt{3}/2$, in common units of GM/a_o. R and z are in units of the oblate scale length a_o, and z denotes the symmetry axis. Black solid lines represent isodensity contours of the stellar distribution. The colour scale is the same for σ^2 and $\overline{v_\varphi^2}$.

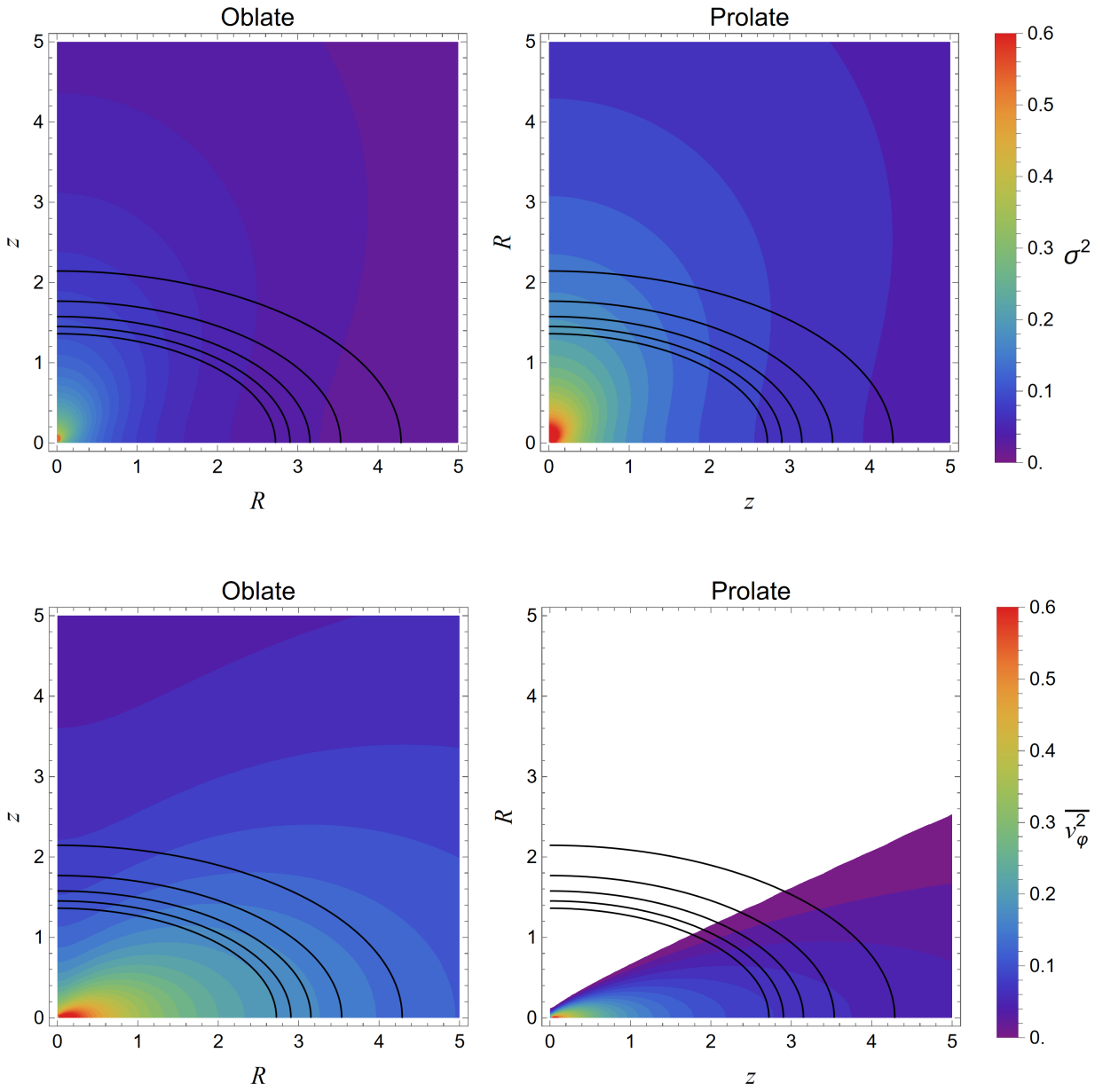

Figure D.2. Maps in the (R,z)-plane of σ^2 (upper panels) and $\overline{v_\varphi^2}$ (lower panels) for oblate (left panels) and prolate (right panels) conjugate Jaffe models with axial ratio of the oblate system $q_o = 1/2$, in common units of GM/a_o. R and z are in units of the oblate scale length a_o, and z denotes the symmetry axis. Black solid lines show isodensity contours of the stellar distribution. The white region in the bottom right panel corresponds to negative values of $\overline{v_\varphi^2}$. The colour scale is the same for σ^2 and $\overline{v_\varphi^2}$.

Intrinsic Velocity Fields in Conjugate Gaussian Models with $q_o = \sqrt{3}/2$

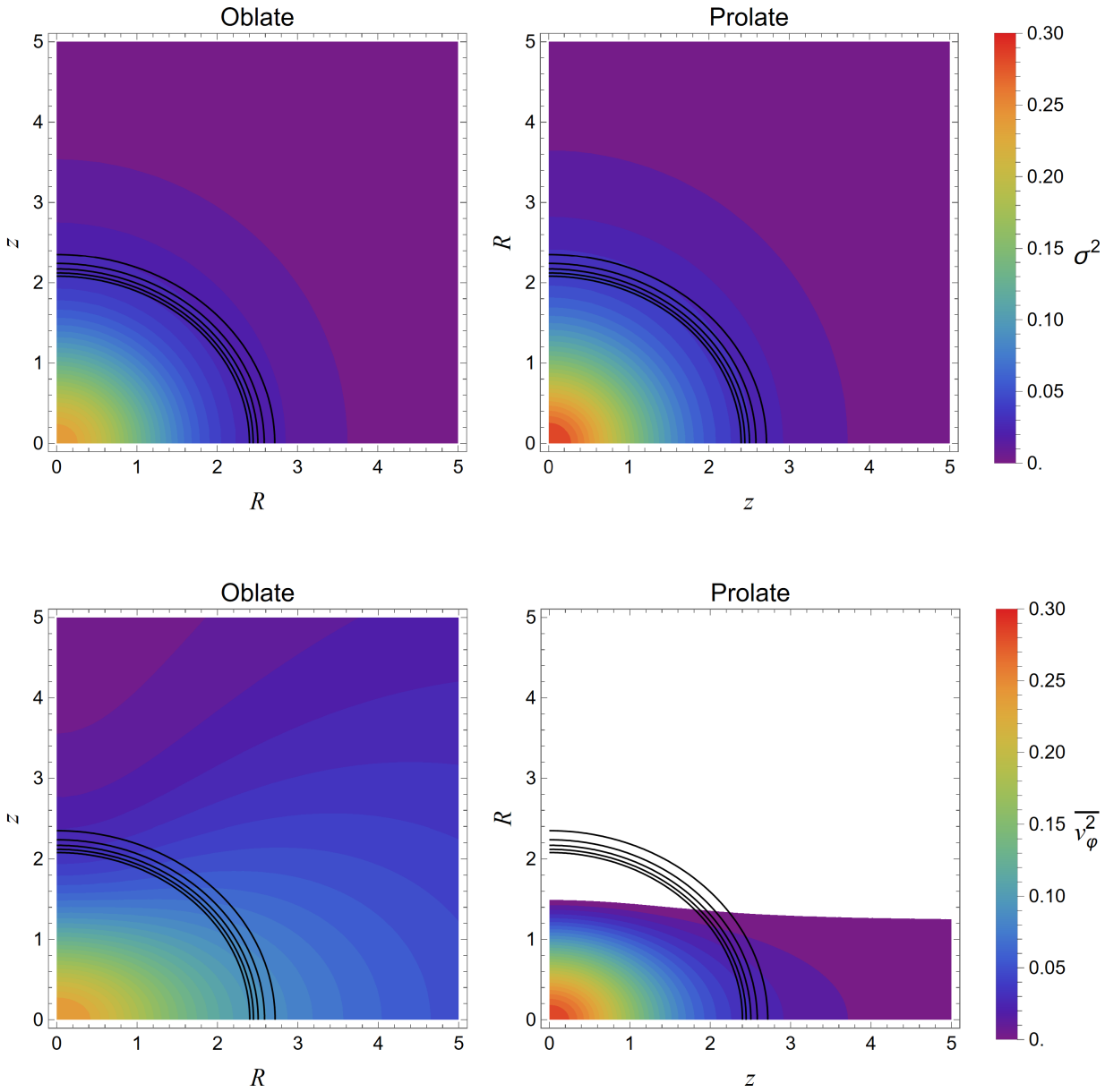

Figure D.3. Maps in the (R,z)-plane of σ^2 (upper panels) and $\overline{v_\varphi^2}$ (lower panels) for oblate (left panels) and prolate (right panels) conjugate Gaussian models with axial ratio of the oblate system $q_o = \sqrt{3}/2$, in common units of GM/a_o. R and z are in units of the oblate scale length a_o, and z denotes the symmetry axis. Black solid lines represent isodensity contours of the stellar distribution. The colour scale is the same for σ^2 and $\overline{v_\varphi^2}$.

Intrinsic Velocity Fields in Conjugate Gaussian Models with $q_o = 1/2$

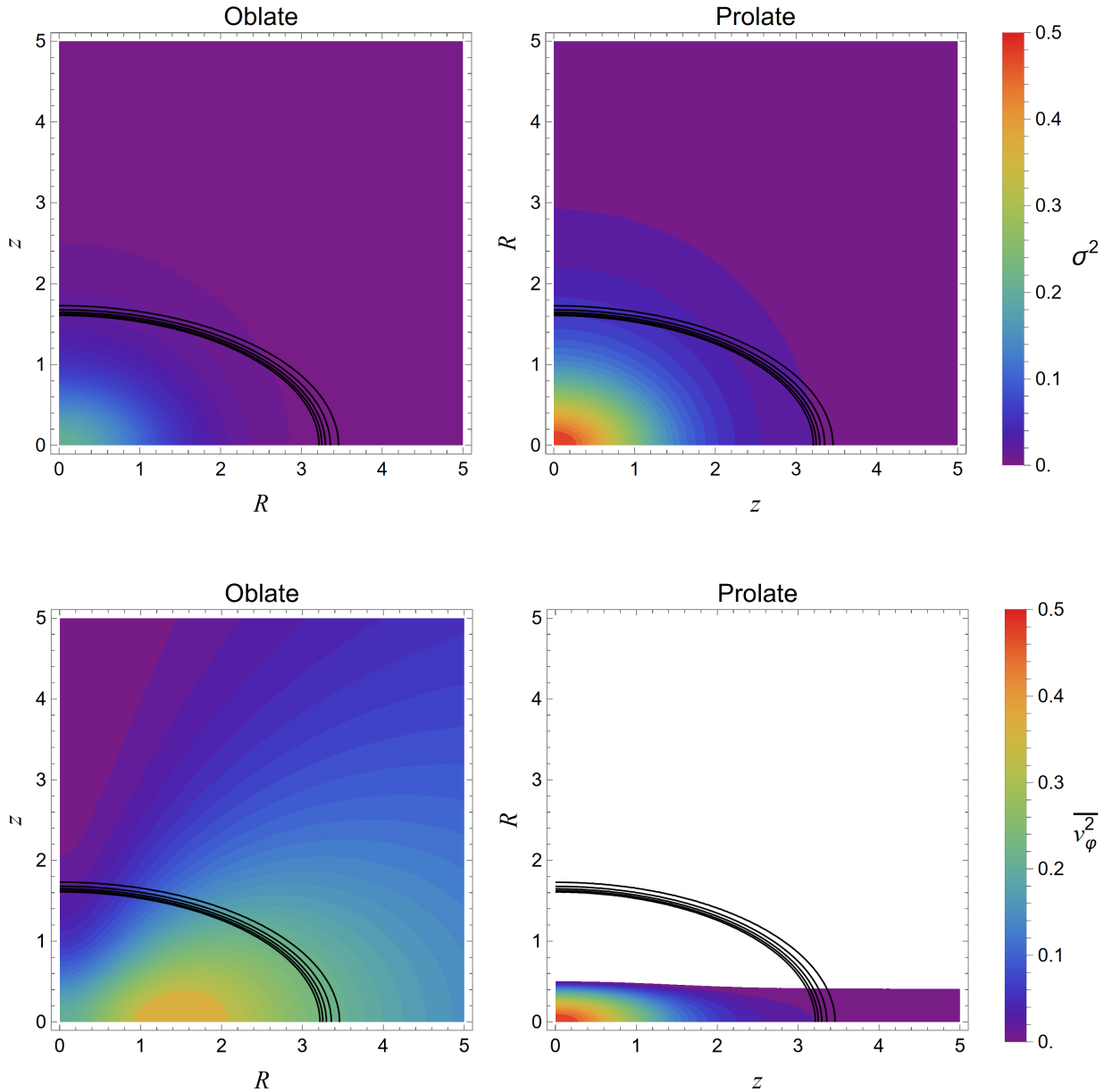

Figure D.4. Maps in the (R,z)-plane of σ^2 (upper panels) and $\overline{v_\varphi^2}$ (lower panels) for oblate (left panels) and prolate (right panels) conjugate Gaussian models with axial ratio of the oblate system $q_o = 1/2$, in common units of GM/a_o. R and z are in units of the oblate scale length a_o, and z denotes the symmetry axis. Black solid lines show isodensity contours of the stellar distribution. The white region in the bottom right panel corresponds to negative values of $\overline{v_\varphi^2}$. The colour scale is the same for σ^2 and $\overline{v_\varphi^2}$.

References

Bertin, G., Ciotti, L., and Del Principe, M. (2002). "Weak homology of elliptical galaxies." In: *A&A* 386, pp. 149–168. DOI: 10.1051/0004-6361:20020248. arXiv: astro-ph/0202208 [astro-ph].

Bertola, F. and Capaccioli, M. (1975). "Dynamics of early type galaxies. I. The rotation curve of the elliptical galaxy NGC 4697." In: *Ap.J.* 200, pp. 439–445. DOI: 10.1086/153808.

Bertola, F. and Galletta, G. (1978). "A new type of galaxy with prolate structure." In: *Ap.J. (Letters)* 226, pp. L115–L118. DOI: 10.1086/182844.

Binney, J. (1978). "Elliptical galaxies: prolate, oblate or triaxial?" In: *Comments on Astrophysics* 8.2, pp. 27–36.

Binney, J., Davies, R. L., and Illingworth, G. D. (1990). "Velocity Mapping and Models of the Elliptical Galaxies NGC 720, NGC 1052, and NGC 4697". In: *Ap.J.* 361, p. 78. DOI: 10.1086/169169.

Binney, J. and Tremaine, S. (2008). *Galactic Dynamics: Second Edition*. Princeton University Press.

Caon, N., Capaccioli, M., and D'Onofrio, M. (1993). "On the shape of the light profiles of early-type galaxies." In: *MNRAS* 265, pp. 1013–1021. DOI: 10.1093/mnras/265.4.1013. arXiv: astro-ph/9309013 [astro-ph].

Cappellari, M. (2008). "Measuring the inclination and mass-to-light ratio of axisymmetric galaxies via anisotropic Jeans models of stellar kinematics". In: *MNRAS* 390.1, pp. 71–86. DOI: 10.1111/j.1365-2966.2008.13754.x. arXiv: 0806.0042 [astro-ph].

— (2016). "Structure and Kinematics of Early-Type Galaxies from Integral Field Spectroscopy". In: *ARAA* 54, pp. 597–665. DOI: 10.1146/annurev-astro-082214-122432.

Chandrasekhar, S. (1969). *Ellipsoidal Figures of Equilibrium*. Dover Publications.

Ciotti, L. (2021). *Introduction to Stellar Dynamics*. Cambridge University Press.

Ciotti, L. and Bertin, G. (1999). "Analytical properties of the $R^{1/m}$ law". In: *A&A* 352, pp. 447–451. DOI: 10.48550/arXiv.astro-ph/9911078. arXiv: astro-ph/9911078 [astro-ph].

Ciotti, L., De Deo, L., and Pellegrini, S. (2025). "An accurate and simple asymptotically matched deprojection of the Sérsic law". In: *A&A* 694, A118.

Ciotti, L. and Pellegrini, S. (1996). "The energetics of flat and rotating early-type galaxies and their X-ray luminosity". In: *MNRAS* 279, p. 240. DOI: 10.1093/mnras/279.1.240. arXiv: astro-ph/9510086 [astro-ph].

de Vaucouleurs, G. (1948). "Recherches sur les Nebuleuses Extragalactiques". In: *Annales d'Astrophysique* 11, p. 247.

Dejonghe, H. (1986). "Stellar dynamics and the description of stellar systems." In: *Phys. Rep.* 133.3, pp. 217–313. DOI: 10.1016/0370-1573(86)90098-0.

Ebrová, I. and Łokas, E. L. (2017). "Galaxies with Prolate Rotation in Illustris". In: *Ap.J.* 850.2, 144, p. 144. DOI: 10.3847/1538-4357/aa96ff. arXiv: 1708.03311 [astro-ph.GA].

Evans, N. W. (1994). "The power-law galaxies." In: *MNRAS* 267, pp. 333–360. DOI: 10.1093/mnras/267.2.333.

Ferrers, N. M. (1877). "On the Potentials, Ellipsoids, Ellipsoidal Shells, Elliptic Laminae, and Elliptics Rings, of Variable Densities". In: *Quart. J. Pure Appl. Math.* 14, pp. 1–22.

Graham, A. W. and Guzmán, R. (2003). "HST Photometry of Dwarf Elliptical Galaxies in Coma, and an Explanation for the Alleged Structural Dichotomy between Dwarf and Bright Elliptical Galaxies". In: *AJ* 125.6, pp. 2936–2950. DOI: 10.1086/374992. arXiv: astro-ph/0303391 [astro-ph].

Hernquist, L. (1990). "An Analytical Model for Spherical Galaxies and Bulges". In: *Ap.J.* 356, p. 359. DOI: 10.1086/168845.

Hubble, E. P. (1926). "Extragalactic nebulae." In: *Ap.J.* 64, pp. 321–369. DOI: 10.1086/143018.

Hunter, C. (1975). "Determination of the distribution function of an elliptical galaxy". In: *AJ* 80, p. 783. DOI: 10.1086/111812.

Hunter, C. and Qian, E. (1993). "Two-integral distribution functions for axisymmetric galaxies." In: *MNRAS* 262, pp. 401–428. DOI: 10.1093/mnras/262.2.401.

Illingworth, G. (1977). "Rotation in 13 elliptical galaxies." In: *Ap.J. Let.* 218, pp. L43–L47. DOI: 10.1086/182572.

Jaffe, W. (1983). "A simple model for the distribution of light in spherical galaxies." In: *MNRAS* 202, pp. 995–999. DOI: 10.1093/mnras/202.4.995.

Jiang, Z. and Moss, D. (2002). "Prolate Jaffe models for galaxies". In: *MNRAS* 331.1, pp. 117–125. DOI: 10.1046/j.1365-8711.2002.05172.x.

Jing, Y. P. and Suto, Y. (2002). "Triaxial Modeling of Halo Density Profiles with High-Resolution N-Body Simulations". In: *Ap.J.* 574.2, pp. 538–553. DOI: 10.1086/341065. arXiv: astro-ph/0202064 [astro-ph].

Kimm, T. and Yi, S. K. (2007). "Intrinsic Axis Ratio Distribution of Early-Type Galaxies from the Sloan Digital Sky Survey". In: *Ap.J.* 670.2, pp. 1048–1055. DOI: 10.1086/522573.

Krajnović, D., Emsellem, E., Cappellari, M., Alatalo, K., Blitz, L., Bois, M., Bournaud, F., Bureau, M., Davies, R. L., Davis, T. A., de Zeeuw, P. T., Khochfar, S., Kuntschner, H., Lablanche, P., McDermid, R. M., Morganti, R., Naab, T., Oosterloo, T., Sarzi, M., Scott, N., Serra, P., Weijmans, A., and Young, L. M. (2011). "The ATLAS^{3D} project - II. Morphologies, kinemetric features and alignment between photometric and kinematic axes of early-type galaxies". In: *MNRAS* 414.4, pp. 2923–2949. DOI: 10.1111/j.1365-2966.2011.18560.x. arXiv: 1102.3801 [astro-ph.CO].

Li, H., Mao, S., Cappellari, M., Graham, M. T., Emsellem, E., and Long, R. J. (2018). "SDSS-IV MaNGA: The Intrinsic Shape of Slow Rotator Early-type Galaxies". In: *Ap.J.*

(Letters) 863.2, L19, p. L19. DOI: 10.3847/2041-8213/aad54b. arXiv: 1807.08872 [astro-ph.GA].

Li, H., Mao, S., Emsellem, E., Xu, D., Springel, V., and Krajnović, D. (2018). "The origin and properties of massive prolate galaxies in the Illustris simulation". In: *MNRAS* 473.2, pp. 1489–1511. DOI: 10.1093/mnras/stx2374. arXiv: 1709.03345 [astro-ph.GA].

Lynden-Bell, D. (1962). "Stellar dynamics: Exact solution of the self-gravitation equation". In: *MNRAS* 123, p. 447. DOI: 10.1093/mnras/123.5.447.

Miller, R. H. (1978). "Free collapse of a rotating sphere of stars." In: *Ap.J.* 223, pp. 122–128. DOI: 10.1086/156242.

Novak, G. S., Cox, T. J., Primack, J. R., Jonsson, P., and Dekel, A. (2006). "Shapes of Stellar Systems and Dark Halos from Simulations of Galaxy Major Mergers". In: *Ap.J. (Letters)* 646.1, pp. L9–L12. DOI: 10.1086/506605. arXiv: astro-ph/0604121 [astro-ph].

Posacki, S., Pellegrini, S., and Ciotti, L. (2013). "The effects of galaxy shape and rotation on the X-ray haloes of early-type galaxies". In: *MNRAS* 433.3, pp. 2259–2274. DOI: 10.1093/mnras/stt898. arXiv: 1304.4085 [astro-ph.GA].

Qian, E., de Zeeuw, P. T., van der Marel, R. P., and Hunter, C. (1995). "Axisymmetric galaxy models with central black holes, with an application to M32". In: *MNRAS* 274.2, pp. 602–622. DOI: 10.1093/mnras/274.2.602. arXiv: astro-ph/9412067 [astro-ph].

Roberts, P. H. (1962). "On the Superpotential and Supermatrix of a Heterogeneous Ellipsoid." In: *Ap.J.* 136, p. 1108. DOI: 10.1086/147461.

Satoh, C. (1980). "Dynamical Models of Axisymmetric Galaxies and Their Applications to the Elliptical Galaxy NGC4697". In: *PASJ* 32, p. 41.

Schechter, P. L. and Gunn, J. E. (1979). "Observations of the internal dynamics of 12 elliptical galaxies." In: *Ap.J.* 229, pp. 472–484. DOI: 10.1086/156978.

Schwarzschild, M. (1979). "A numerical model for a triaxial stellar system in dynamical equilibrium." In: *Ap.J.* 232, pp. 236–247. DOI: 10.1086/157282.

Tsatsi, A., Lyubenova, M., van de Ven, G., Chang, J., Aguerri, J. A. L., Falcón-Barroso, J., and Macciò, A. V. (2017). "CALIFA reveals prolate rotation in massive early-type galaxies: A polar galaxy merger origin?" In: *A&A* 606, A62, A62. DOI: 10.1051/0004-6361/201630218. arXiv: 1707.05130 [astro-ph.GA].

van der Marel, R. P. (1991). "The velocity dispersion anisotropy and mass-to-light ratio of elliptical galaxies." In: *MNRAS* 253, pp. 710–726. DOI: 10.1093/mnras/253.4.710.